Doctoral Dissertation

GOLD NANOPARTICLES-FUNCTIONALIZED GRAPHENE OXIDE NANORIBBONS FOR ENHANCED PERFORMANCE OF ELECTROCHEMICAL BASED-BIOSENSORS

Nur Syakimah Ismail

January 2015

Graduate School of Engineering
Osaka University

GOLD NANOPARTICLES-FUNCTIONALIZED GRAPHENE OXIDE NANORIBBONS FOR ENHANCED PERFORMANCE OF ELECTROCHEMICAL BASED-BIOSENSORS

(金ナノ粒子で機能化した酸化グラフェンナノリボンを用いた高機能な電気化学バイオセンサー)

A dissertation submitted in partial fulfillment of the requirements
for the degree of Doctor of Philosophy

by

Nur Syakimah Ismail

Department of Precision Science & Technology and Applied Physics
Graduate School of Engineering
Osaka University

TABLE OF CONTENTS

LIST OF ABBREVIATIONS

3-AP	3-amino-phthalate
3-AP*	Excited state of 3-amino-phthalate
AA	Ascorbic acid
ABEI	*N*-(aminobutyl)-*N*-(ethylisoluminol)
ABEI-AuNP	Gold Nanoparticle coated ABEI molecules
Ag/AgCl	Silver/Silver Chloride reference electrode
AP	*ρ*-acetamidophenol
ATR-FTIR	Attenuated Total Reflection – Fourier Transform Infrared
AuNP	Gold Nanoparticle
CA	Chronoamperometry
CBS	Carbonate Buffer Solution
CE	Counter Electrode
CL	Chemiluminescence
CNT	Carbon Nanotube
CS	Carbon sheet
CV	Cyclic Voltammetry
ECL	Electrochemiluminescence
EPPG	Edge-Plane Pyrolytic Graphite
GIC	Graphite Intercalation Compound
GNR	Graphene Nanoribbon
GO	Graphene Oxide
GONR	Graphene Oxide Nanoribbon
GOR	Glucose Oxidation Reaction

H_2O_2	Hydrogen Peroxide
H_2SO_4	Sulfuric acid
$HAuCl_4$	Hydrogen Tetrachloroaurate (III) Tetrahydrate
HOPG	Highly Ordered Pyrolytic Graphite
HOO^-	Hydrogen peroxide anion
$HOO^{\bullet-}$	Hydroperoxy radical
$K_3[Fe(CN)_6]$	Potassium Ferricyanide
$KMnO_4$	Potassium Permanganate
LH^-	Luminol monoanion
$LH^{\bullet-}$	Diazasemiquinone radical
LOD	Limit of detection
LSV	Linear Sweep Voltammetry
Luminol	3-amino-phthalhydrazide
MWCNT	Multi-walled Carbon Nanotube
MWCNT_L	Large Diameter of Multi-walled Carbon Nanotube (110-170 nm)
MWCNT_M	Medium Diameter of Multi-walled Carbon Nanotube (40-70 nm)
MWCNT_S	Small Diameter of Multi-walled Carbon Nanotube (3-20 nm)
N_2	Nitrogen
NADH	β-nicotinamide adenine dinucleotide dehydrogenase
NHE	Normal Hydrogen Electrode
O_2	Oxygen
$O_2^{\bullet-}$	Superoxide radical
$OH^{\bullet}$	Hydroxyl radical
OH_{ads}	Hydroxyl adsorption
PBS	Phosphate Buffer Solution

PGO	Pristine Graphite Oxide
PL	Photoluminescence
PPy	Polypyrrole
RE	Reference Electrode
SEM	Scanning Electron Microscopy
SPE	Screen Printed Electrode
UA	Uric acid
UV-Vis	Ultraviolet – Visible Spectrophotoscopy
WE	Working Electrode

NOMENCLATURE

ΔE_p	Peak-to-peak redox potential	[V]
λ_{max}	Absorption peak	[a.u.]
A	Active surface area	[cm^2]
D_0	Diffusion coefficient	[$cm^2\ s^{-1}$]
I_p	Peak current	[A]
I_{peak}	Peak current density	[$mA\ cm^{-2}$]
k^o_{basal}	Electron transfer rate at basal plane	[s^{-1}]
k^o_{edge}	Electron transfer rate at edge plane	[s^{-1}]
v	Scan rate	[$V\ s^{-1}$]
V_{ox}	Oxidation peak	[V]

CHAPTER 1

INTRODUCTION

1.1 Biosensors

Biosensors have been at the forefront of research due to their wide range of applications such as in medical diagnosis, food inspections, environmental monitoring and many more [1]. Biosensors can be defined as simple analytical devices that combine the high sensitivity and specificity of a biological molecule with the versatility of physical transducers to convert biological responses into readable electronic signals [2]. A typical biosensor consists of two parts, which are a biological sensing element and a physical transducer, as depicted in Fig. 1.1. The sensor's recognition element enables the selective response to a particular analyte, thus minimizing interference from other sample components [3]. The purpose of the transducer is to convert a biochemical signal into an electronic signal [4]. There are various types of transducer including piezoelectric, calorimetric, optical, electrochemical and thermal transducer [2,4,5]. The appropriate transducer configuration depends significantly on the nature of the biocatalyst system and the secondary products to be monitored [2]. In this thesis, we focus on electrochemical transducers.

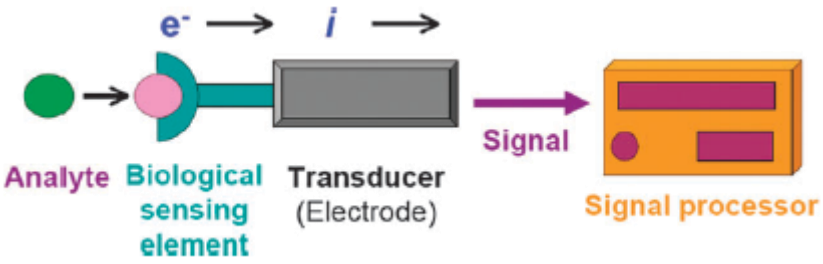

Figure 1.1: Basic building blocks of a biosensor [3].

1.1.1 Electrochemical biosensors

Electrochemical biosensors combine biological recognition element (enzymes, proteins, antibodies, nucleic acids, etc) that selectively reacts with the target analytes and produces an electrical signal whose intensity is proportional to the concentration of the analyte being studied (Fig. 1.2 (A)) [3]. The electrochemical biosensor is part of an electrochemical cell, which consists of three electrodes; working, reference and counter electrodes (Fig. 1.2 (B)). The working electrode (WE) is where the reaction of interest occurs while the counter electrode (CE, also known as auxiliary electrode) is used to close the current circuit in the electrochemical cell, which is usually made of an inert material and does not participate in the electrochemical reaction. The reference electrode (RE) is an electrode that has a stable and well-known electrode potential, and is used as a point of reference in the electrochemical cell for potential control and measurement [6]. The electrochemical reaction being monitored usually generates a measurable current (amperometry), charge accumulation (potentiometry) or resistance and reactance (impedance) [2-3]. The most common technique employed in electrochemical sensing is amperometry, where a potential relative to the RE potential is applied to WE in order to measure resultant current (Fig. 1.2 (C)) In amperometry, the kinetics of the electron transfer reaction is driven by the applied potential, which affects the diffusion-controlled current flowing across the electrode/solution interface. Consequently, the current is obtained through electrolysis by means of an electrochemical reduction or oxidation at WE, which is directly proportional to the bulk concentration of the analyte present in the solution [6]. Therefore, electrochemical biosensors offer ease of fabrication and sensitive detection of analytes, which covers a wide range of biomolecules [7]. The electrochemical method is further improved by combination with the chemiluminescence technique to achieve highly sensitive detection, as will be discussed in the next section.

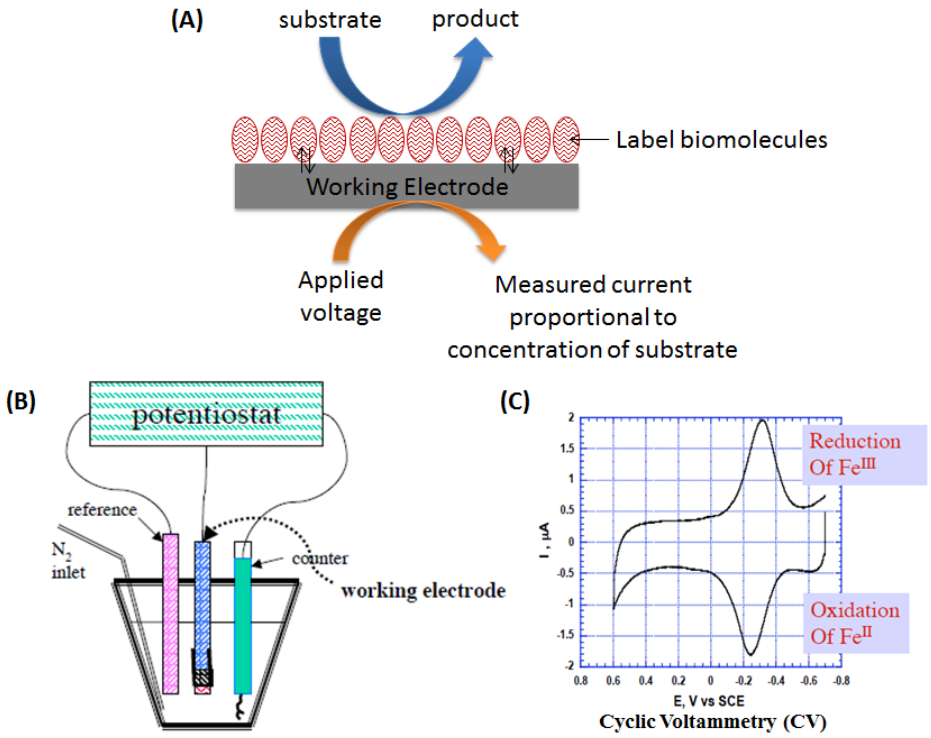

Figure 1.2: (A) Principle of electrochemical biosensors. (B) An electrochemical cell. (C) Output current based on oxidation-reduction (redox) reaction.

1.1.2 Electrochemiluminescence biosensors

Luminescence is the generation of light without heat. This phenomenon can occur through several luminescent processes, namely photoluminescence (PL), chemiluminescence (CL) and electrogenerated chemiluminescence (ECL), as depicted in Fig. 1.3 [8]. PL is a process in which a substance absorbs photons (electromagnetic radiation) and then re-radiates photons, which normally happens in solid materials [9]. CL is initiated by the mixing of necessary reagents and is often controlled by the careful manipulation of fluid flow, while luminescence in ECL is initiated and controlled by changing an electrode potential [8]. The advantages of ECL method in comparison to CL are (i) the electrochemical reaction allows for the time and position control of light-emitting reaction, (ii) it is highly selective due to the redox reaction's dependence on the applied potential, and (iii) it is non-destructive techniques [8].

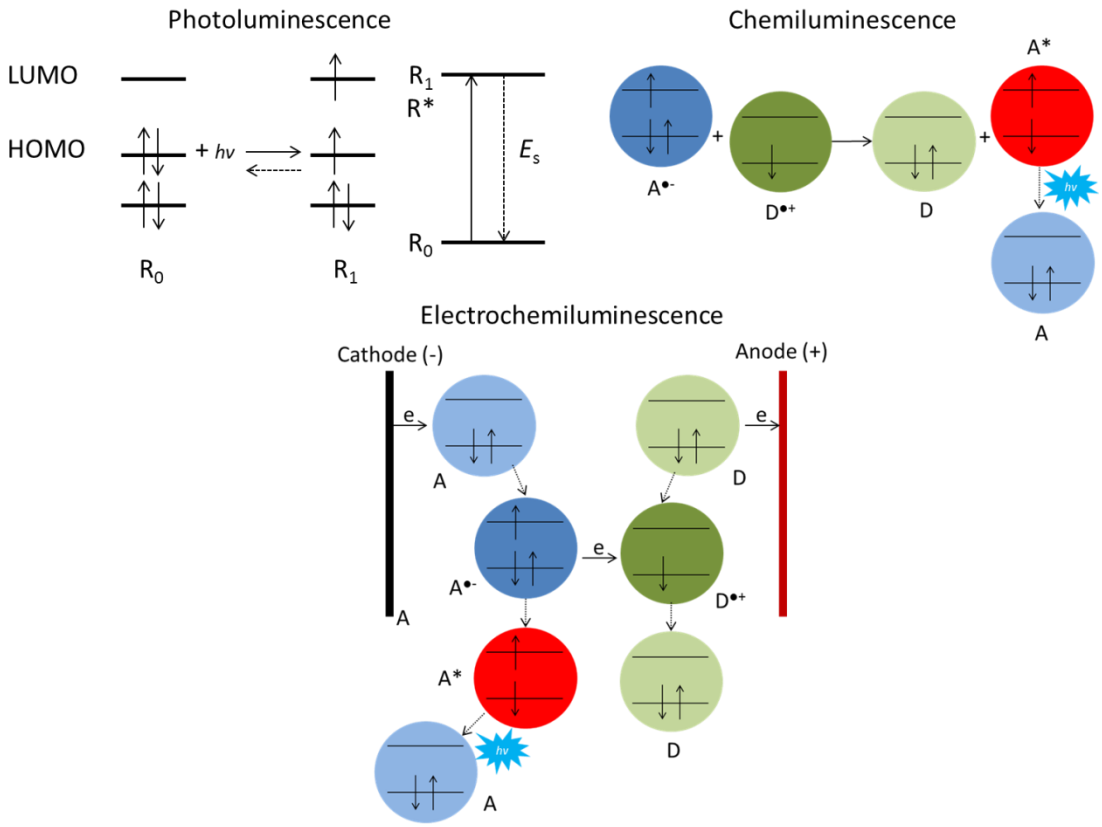

Figure 1.3: Schematic of the general mechanisms of photoluminescence, chemiluminescence and electrogenerated chemiluminescence [8].

Electrogenerated chemiluminescence (ECL) is produced from the excited state of an ECL luminophore using electrochemical techniques, has been applied to the fields of immunoassay, clinical sensing, and environmental monitoring owing to its high sensitivity and extremely wide dynamic range [10]. ECL luminophores are mainly divided into organic (e.g. Luminol) and inorganic (e.g. Ruthenium complex) compounds [11]. ECL is a means of converting electrical energy into radiative energy that involves the production of reactive intermediates from stable precursors at the surface of an electrode. These intermediates then react under a variety of conditions to form excited states that emit light [9,11]. There are two dominant pathways to generate ECL, namely the annihilation and co-reactant pathways [9-11].

In the annihilation pathway, both oxidized and reduced species are produced on the electrode surface by a potential step or sweep. These species then interact to produce a ground state and an electronically excited state the latter of, which then relaxes by emission (Eqs. 1-4) [10-11].

$D - e^- \rightarrow D^{\bullet+}$ (oxidation at electrode) (1)

$A + e^- \rightarrow A^{\bullet-}$ (reduction at electrode) (2)

$A^{\bullet-} + D^{\bullet+} \rightarrow A^{\bullet} + D$ (excited-state formation) (3)

$A^{\bullet} \rightarrow A + h\nu$ (light emission) (4)

where A and D can be from the same species. In the co-reactant pathway, ECL is usually generated by one directional potential scanning on the electrode in the presence of both the luminophore and co-reactant (Eqs. 5-8). Common co-reactants used in ECL are the oxalate ion ($C_2O_4^{2-}$) and tripropylamine (TPrA). A very interesting phenomenon in this system is that the oxidation of the co-reactant leads to the generation of a strong reductant, instead of an oxidant. ECL systems involving the generation of reductants by electrochemical oxidation are referred to as ‘‘oxidative-reductive’’ ECL systems [9-10].

$C_2O_4^{2-} - e^- \rightarrow [C_2O_4^{\bullet-}] \rightarrow CO_2^{\bullet-} + CO_2$ (Co-reactant) (5)

$D - e^- \rightarrow D^{\bullet+}$ (Luminophore)(6)

$CO_2^{\bullet-} + D^{\bullet+} \rightarrow D^{\bullet} + CO_2$ (7)

$D^{\bullet} \rightarrow D + h\nu$ (8)

1.1.3 Nanomaterial-based electrochemical biosensors

The signal transduction and the general performance of electrochemical sensors are often determined by the nanometer-scale surface architectures that connect the sensing element to the biological sample [12]. One of the efforts is utilization of nanomaterials due to their desirable properties. In particular, the ability to tailor the size and structure and hence the properties of nanomaterials offers excellent prospects for designing novel sensing systems and enhancing the performance of bioanalytical assays [13]. Nanomaterials can help address some of the key issues in the development of all biosensors. Such issues include: design of the biosensing interface so that the analyte selectively interacts with the biosensing surface; achievement of efficient transduction of the biorecognition event; increases in the sensitivity and selectivity of the biosensor; and improvement of response times in very sensitive systems [14]. Electrochemical biosensors in combination with nanomaterials have become simple, efficient tools to measure the concentration of analytes at low cost [7,13].

Nanomaterials, particularly carbon nanomaterials, have been at the forefront of nanomaterial research for decades with the discovery of fullerenes, carbon nanotubes (CNTs), and more recently, graphene [14]. Carbon nanomaterials have shown attractive properties for electrochemical biosensing due to their high conductivity, large active surface area and ease of functionalization [14-15].

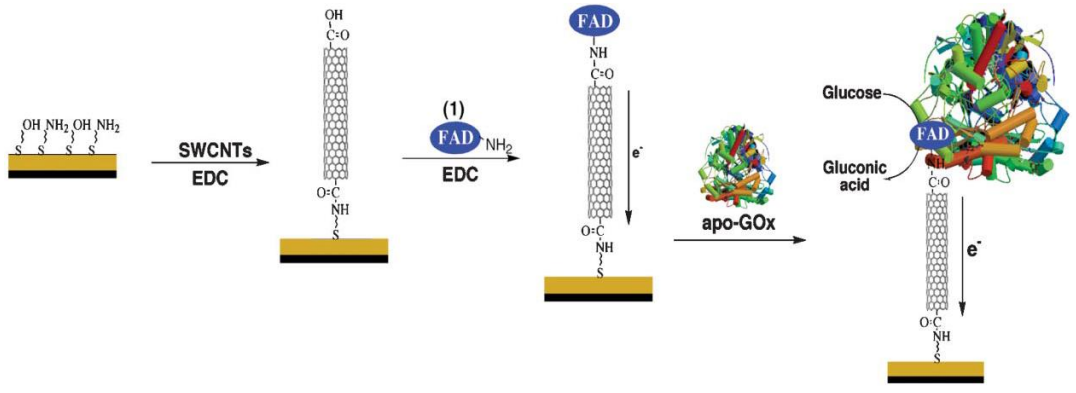

Figure 1.4: Assembly of functionalized-single-walled CNT (SWCNT) electrically contacted glucose oxidase electrode [16].

In addition, many kinds of nanoparticles, such as metal, oxide and semiconductor nanoparticles have been used for constructing electrochemical sensors and biosensors. These nanoparticles play different roles in different sensing systems. Among important functions provided by nanoparticles include the immobilization of biomolecules, the catalysis of electrochemical reactions, the enhancement of electron transfer between electrode surfaces and proteins, labeling of biomolecules and even acting as reactants [17]. Catalysis is the most important chemical application of metal nanoparticles, and has been studied extensively. Transition metals, especially precious metals, have catalytic activity for many organic reactions. In addition, metal nanoparticles can be used as heterogeneous and homogeneous catalysts. The catalysis takes place on the active sites of the surface of metal nuclei (i.e. the mechanism is similar to conventional heterogeneous catalysis).

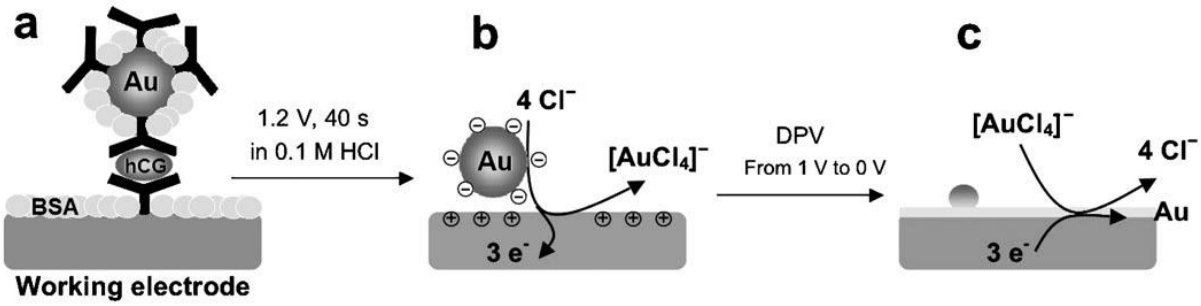

Figure 1.5: Gold nanoparticle used as label in immunosensor [18].

1.2 Gold nanoparticle in electrochemical biosensor

Nanosized particles of noble metals, especially gold nanoparticles (AuNPs), have received great interest due to their attractive electronic, optical, and thermal properties as well as catalytic properties and potential applications in various fields [19]. Bulk gold (Au) is chemically inert and is generally regarded as a poor catalyst. Interestingly, when Au is in the form of very small particles with diameters below 10 nm and is deposited on metal oxides or activated carbon, it becomes catalytically active, especially at low temperatures [20]. The

catalytic performance of Au is defined by three major factors; contact structure, support selection and particle size [20-21]. The unique properties of AuNPs to provide a suitable microenvironment for biomolecule immobilization while retaining their biological activity, and to facilitate electron transfer between immobilized proteins and electrode surfaces, have led to an intensive use of this nanomaterial for the construction of electrochemical biosensors with enhanced analytical performance with respect to other biosensor designs [22].

Typically, AuNPs are prepared by chemical reduction of the corresponding transition metal salts, hydrogen tetrachloroaurate (III) tetrahydrate ($HAuCl_4.4H_2O$), in the presence of a stabilizer that binds to their surface to impart high stability and rich linking chemistry and to provide the desired charge and solubility properties. After the breakthrough synthesis of AuNPs reported by Schmid [23-24] and Brust et al. [25-26], a variety of methods has been developed to prepare AuNPs. In our study, two types of syntheses were used to prepare AuNPs; burst nucleation and seed growth methods for electrochemical- and electrochemiluminescence-based biosensors, respectively. The burst nucleation method used tert-butylamine-borane complex (TBAB) as a reducing agent as shown in Fig. 1.6. This method required the utilization of hexane as a surfactant to avoid aggregation of AuNPs [27].

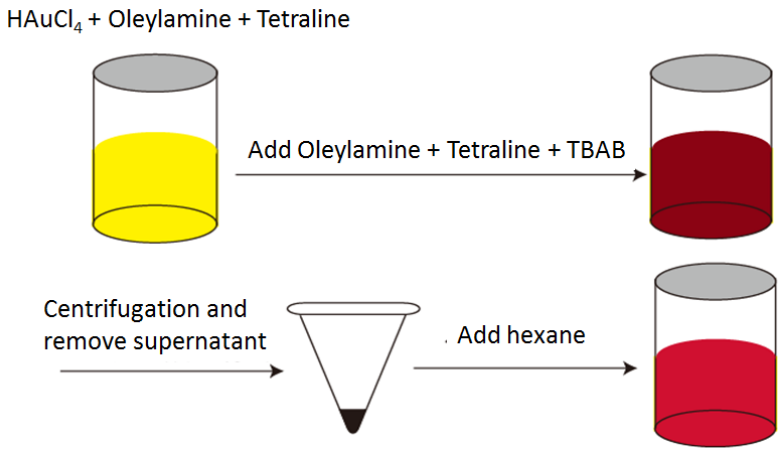

Figure 1.6: Burst nucleation method [27].

On the other hand, the seed growth method involved direct reduction of $HAuCl_4$ in *N*-(aminobutyl)-*N*-(ethylisoluminol) (ABEI) solution [28]. Through this method, AuNPs were form with ABEI molecules existed on its surface through the covalent interaction between gold and nitrogen atoms in their amino groups. Moreover, the carboxylic group in a molecule of the oxidation product of ABEI results on electrostatic repulsion for the stabilization of AuNPs (Fig. 1.7).

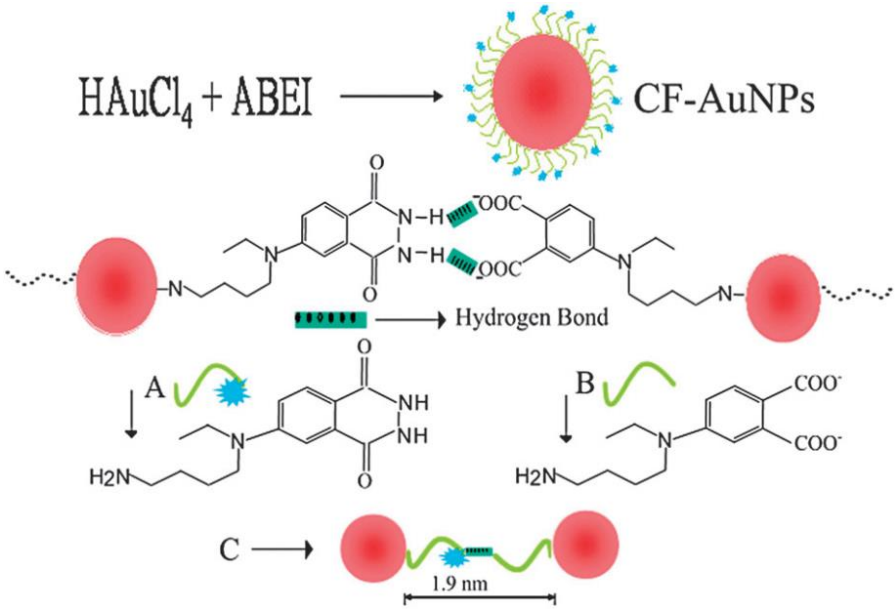

Figure 1.7: Seed growth method [28].

In chapter 3, the role of AuNPs in catalyzing non-enzymatic glucose oxidation reaction was studied in neutral conditions. In alkaline conditions (Fig. 1.8), strong adsorption of hydroxide anions on AuNPs enhanced the rate of deprotonation/dehydrogenation that initiates the glucose oxidation reaction [29]. Regarding this, at neutral or low pH, the rate of deprotonation/dehydrogenation is lower than at higher pH. However, it would be preferable and allow for wider applications if commercialized products were designed to work at neutral pH. To solve this problem, we focused on the development of functionalized carbon nanomaterial which can act as an active functional supporting matrix that could promote the dehydrogenation process and enhance the glucose oxidation reaction kinetics under neutral

conditions.

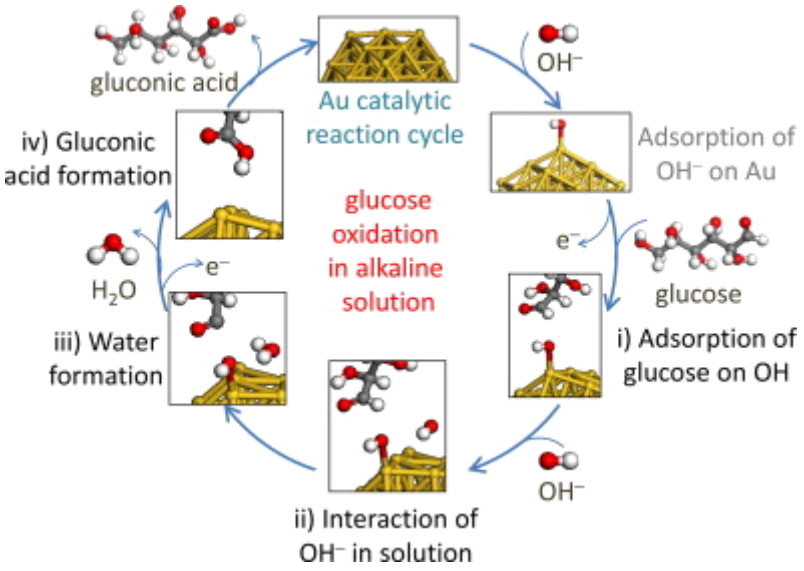

Figure 1.8: Schematic illustration of Au catalytic cycle for glucose oxidation reaction in alkaline solution [29].

Luminol-H_2O_2 CL reaction has been widely applied for the detection of various substances. It has been found that AuNPs could enhance the CL from the luminol-H_2O_2 system depending on their sizes [30]. The CL enhancement by AuNPs of the luminol-H_2O_2 system is proposed to originate from the particles' catalytic activity, which facilitates the radical generation and electron-transfer processes taking place on their surface [30]. Most studies investigate ECL of luminol in solution on the surface of Au electrodes, leaving space to explore ECL of luminol at the solid-liquid interface. In chapter 4, the seed growth method produced isoluminol molecules coated on the surface of AuNPs, which were subsequently drop cast on the working electrode surface. These isoluminol coated AuNP on modified electrodes were subjected to cyclic voltammetry (CV) under various test conditions in order to elucidate the ECL mechanism.

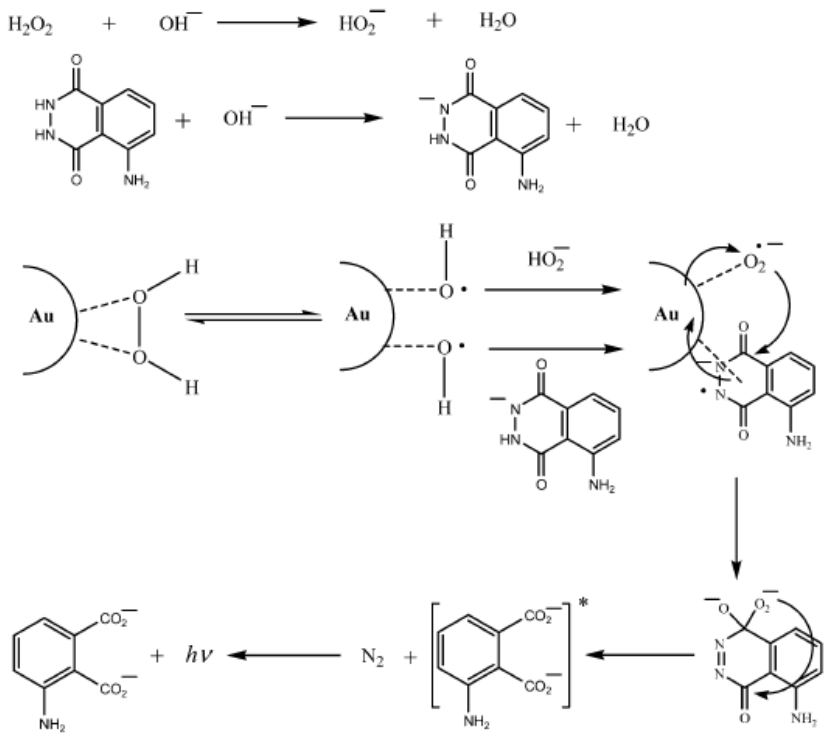

Figure 1.9: Mechanism for luminol-H_2O_2-gold colloid CL system [30].

Conjugation of AuNPs with other nanomaterials and biomolecules is an attractive research area within nano-biotechnology [31]. In this context, carbon nanomaterials, especially carbon nanotubes (CNTs), have attracted much interest in fundamental and applied research due to their unique properties. Hybrid nanoparticle/nanotube materials have been shown to possess interesting properties, which can be beneficial for the development of electrochemical biosensors. Moreover, the incorporation of enzymes into the new composite matrix enables the preparation of a mediator-less biosensor with a remarkably higher sensitivity [32]. Hybrid composites can be prepared by selective attachment of AuNPs to carbon nanotubes' surfaces. This requires the prior of functionalization CNTs in order to immobilize AuNPs. Based on the multiple functions of carbon nanomaterials in electrochemical biosensors, we chose a recently discovered carbon material, graphene, as the functional supporting matrix to improve the catalytic activity of AuNPs.

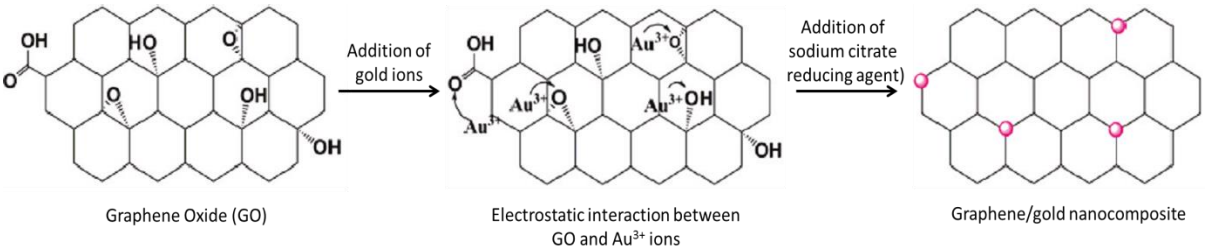

Figure 1.10: Schematic representation of the mechanism of nucleation of gold nanoparticles at functionalized graphene surface [33].

1.3 Graphene for electrochemical applications

1.3.1 Graphene

Graphene is a single atomic layer of carbon atoms in an sp^2 hexagonal bonding configuration. It is the basic building block for other carbon materials, as illustrated in Fig. 1.11 [34]. Even though graphene has been theoretically studied for decades, this material had never been produced until 2003 by Andre Geim and Kostya Novoselov from University of Manchester using the exfoliation method on graphite by scotch tape. Their groundbreaking experiments regarding the 2D material graphene has won them the 2010 Nobel Prize in Physics.

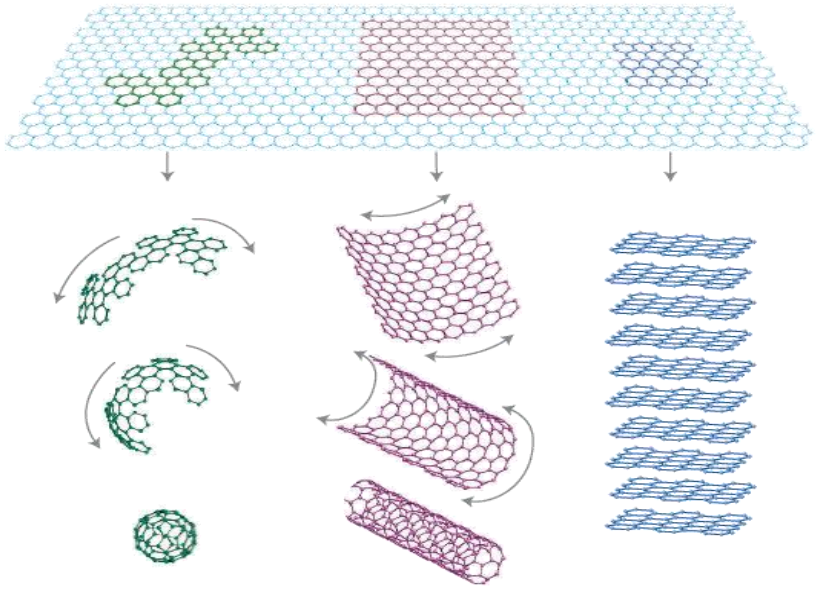

Figure 1.11: Graphene is 2D building material for 0D fullerene, 1D nanotube and 3D graphite [22]

Considerable research has been conducted on graphene since its first introduction by Geim and Novoselov, in order to develop scalable synthesis methods [35-36] and improve material properties [37-38] and functionalities [39-40]. Graphene can be synthesized mainly by mechanical and chemical approaches as depicted in Fig. 1.12. Micromechanical exfoliation has yielded small samples of graphene that are useful for fundamental study. Although large-area films (up to ~1 cm^2) made of single- to few-layer graphene have been generated by chemical vapor deposition (CVD) growth on metal substrates, the uniform growth of single-layer graphene is still a challenge [35]. Meanwhile, chemical synthesis focuses on chemical exfoliation of graphite or cutting of carbon nanotubes to form graphene. Exfoliation of graphite to graphite oxide through Hummer's method has gained much interest due to its simplicity; involves oxidation of graphite in the presence of strong acids and oxidants. Subsequently, the oxygen-based functional groups on graphite oxide can be removed by a reduction process.

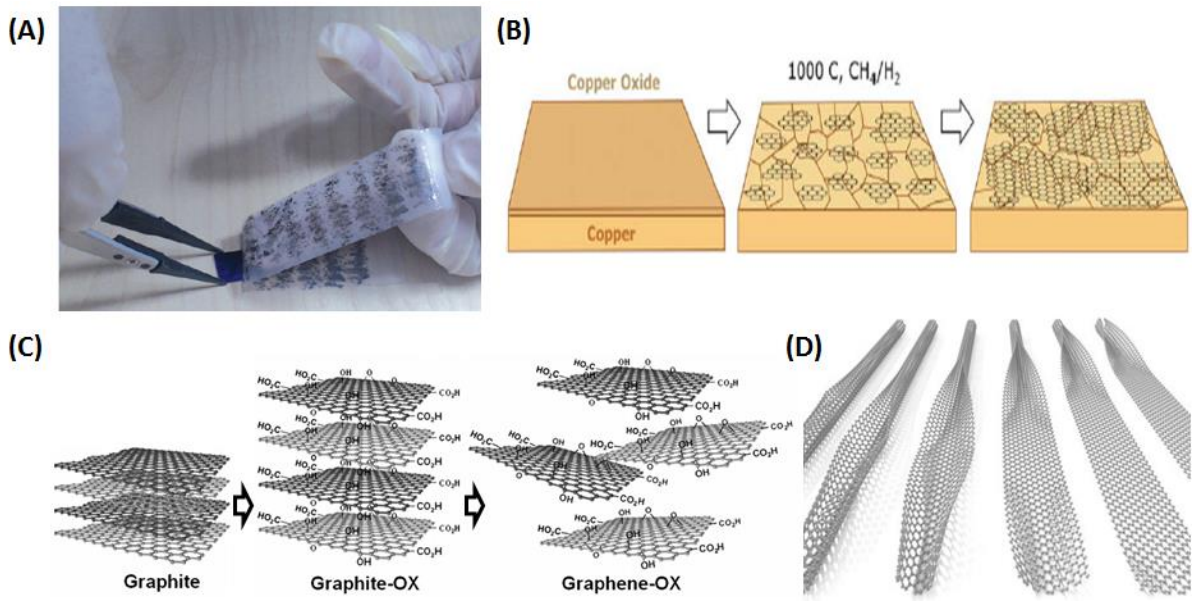

Figure 1.12: Mechanical synthesis through (A) micromechanical exfoliation and (B) CVD epitaxial growth. Chemical synthesis through (C) graphite oxidation and (D) MWCNT unzipping.

1.3.2 Electrochemical performance of graphene

The properties and possible applications of graphene-based materials depend greatly on their synthesis procedure (mechanically or chemically generated) [37]. An electrochemical performance analysis of mechanically and chemically derived graphene demonstrates that pristine graphene has a lower catalytic activity than graphene oxide or bulk graphite [41-42]. Recently, electron transfer in graphene has been demonstrated contributed by its peripheral edge as opposed to its side [43]. This is because the former acts electrochemically akin to that of edge plane- and the latter to that of basal plane-like sites/defects of highly ordered pyrolytic graphite (HOPG). In HOPG, the electron transfer kinetics of the edge is overwhelmingly dominant over that of the basal. Fig. 1.13 illustrates a schematic representation of graphene (A) and graphite (B) indicating their edge and basal sites, where the heterogeneous electron transfer rate of the former (k^{o}_{edge}) is anomalously faster over that of the latter (k^{o}_{basal}). The CVs in Fig. 1.9 depict that increasing the mass deposition of graphene onto underlying edge-plane pyrolytic graphite (EPPG) electrode surface leads to a decrease in the voltammetric peak height (I_p) as well as a significant decrease in the electrochemical reversibility of the redox probe, as evident from the increasing peak-to-peak redox potential (ΔE_p). These results indicate that the addition of graphene onto the EPPG electrode results in the reduction of the observed electron transfer kinetics. It is well documented that the voltammetric response of graphitic electrodes depends on the proportion of edge plane sites, where a low and high proportion result in slow and fast electron transfer, respectively [41-42]. Consequently, the observed deterioration in the electrochemical responses are likely due to the reduced proportion of available edge plane sites and an increased basal plane contribution from the addition of graphene.

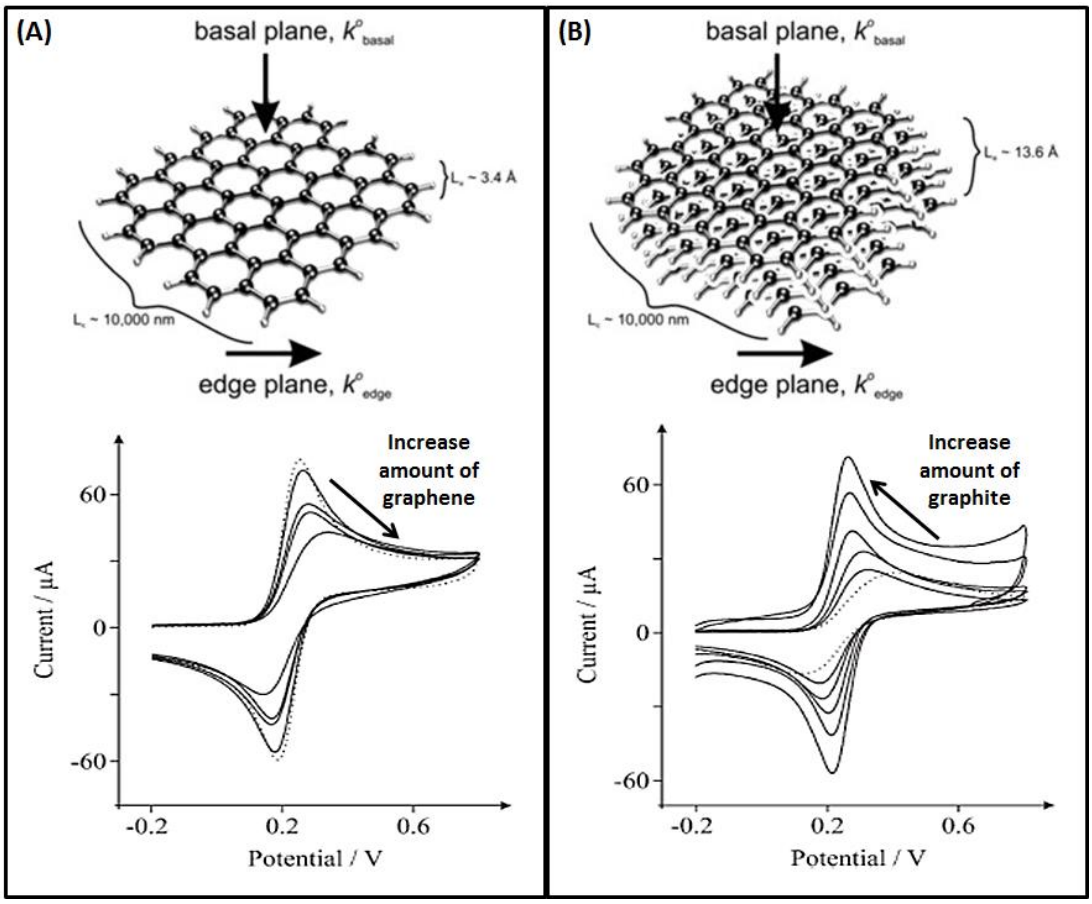

Figure 1.13: Effects of edge and basal planes on the electrochemical performance of (A) pristine graphene and (B) graphite. Cyclic voltammetric profiles recorded utilizing 1 mM potassium ferrocyanide (II) in 1 M KCl.

The majority of graphene used in electrochemistry is produced through the reduction of graphene oxide (GO), which results in partially functionalized graphene sheets or chemically reduced GO, since pristine graphene is inert and difficult to immobilize on electrode surfaces [7]. Therefore, it is expected that reactive edges and structural defects or impurities are beneficial for electrochemical activity [41-42]. Hence, we have chosen to focus on graphene oxide nanoribbons (GONRs), which contain various oxygen-based functional groups on both the basal plane and straight edges of the graphene strip, for use in electrochemical sensors.

1.3.3 Graphene oxide nanoribbons

Graphene nanoribbons (GNRs) are strips of graphene with a high length-to-width ratio and straight edges [44]. Experimentally, microscopic quantities of few-layer GNRs were made available through several processes including microfabrication on graphite surfaces followed by exfoliation, exfoliation of bulk graphite in the presence of surfactants or plasma etching of multi-walled CNTs (MWCNTs) partially imbedded in a layer of protective polymer. Carbon nanotubes are often described as rolled up graphene sheets; therefore, it would seem natural to unroll them to obtain graphene [45]. Fig. 1.14 illustrates several methods utilizing MWCNTs to yield GNRs.

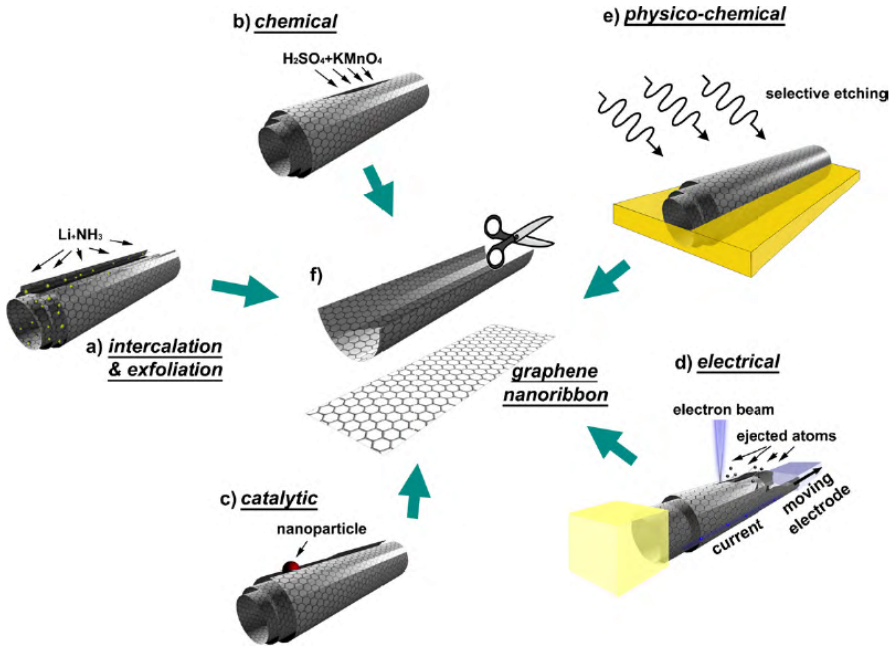

Figure 1.14: Graphene nanoribbon synthesis method [45].

Among the aforementioned methods, the longitudinal unzipping of MWCNTs through an oxidizing process, proposed by Kosynkin et al. [46], is extremely simple, efficient, and potentially scalable for producing exfoliated graphene sheets. This unzipping method involves suspending the MWCNTs in concentrated sulfuric acid (H_2SO_4) for 1–12 h followed

by a potassium permanganate ($KMnO_4$) treatment. They determined that their method gained a high degree of consecutive tube openings when high amounts of $KMnO_4$ were used. Since the unzipping process is oxidative, the resultant nanoribbons possess various types of oxygen-based functional groups at their edges and on their graphitic surfaces, similar to GO. Therefore, these nanoribbons are termed graphene oxide nanoribbons (GONRs). The advantages of this method include the ability to control the number of graphene layers based on the selected MWCNT diameter and the uniformity of the resultant nanoribbon structure.

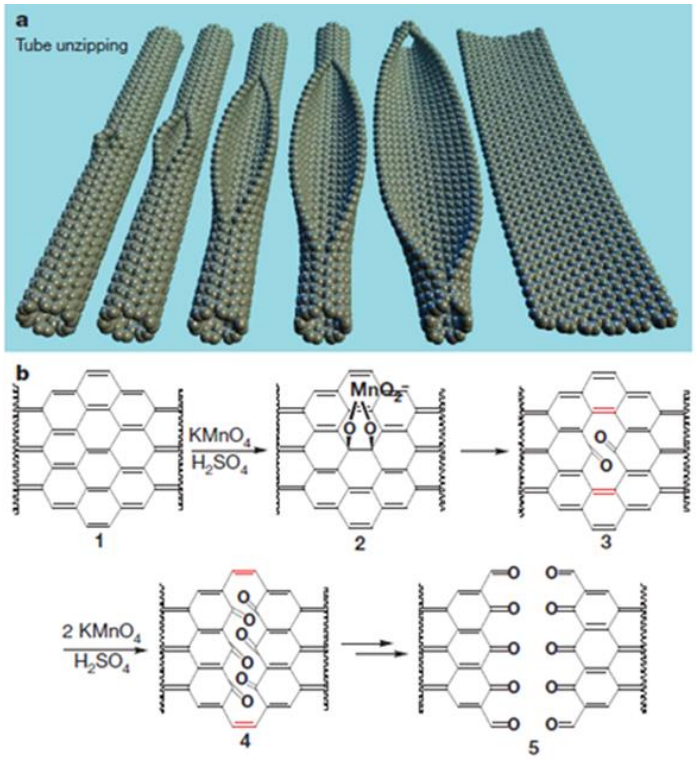

Figure 1.15: Longitudinal unzipping of MWCNT [34].

Recent reports on the mechanism of GO formation from bulk graphite using a modified Hummer's method (Fig. 1.16) revealed that the first step was the conversion of graphite to a sulfuric acid–graphite intercalation compound (H_2SO_4-GIC) followed by the conversion of the GIC to the oxidized form of graphite (pristine graphite oxide, PGO) by

permanganate, and finally the formation of GO by the reaction of PGO with water [47]. The formation of the H_2SO_4-GIC was described as beginning immediately upon exposure of the graphite to the acid medium, while the conversion of GIC to PGO was slower depending on the graphite source.

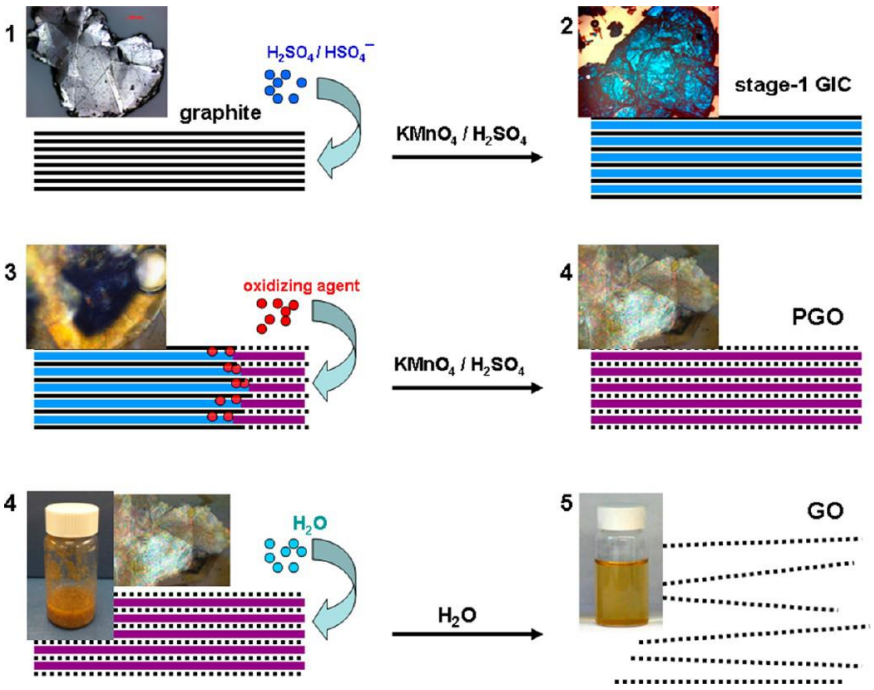

Figure 1.16: Schematic of conversion of bulk graphite to GO [47].

In comparison to graphite, MWCNTs as the starting material have a unique 2D structure, with diameters ranging from 2 to 500 nm and lengths from 50 nm to a few mm. The MWCNTs contain several concentric coaxial graphene cylinders with an interlayer spacing of 0.34 nm, similar to graphite [48]. However, studies have shown that this interlayer spacing increases with a decreasing nanotube diameter as depicted in Fig. 1.17 [49]. Smaller nanotube diameters have a higher interlayer spacing due to the large repulsive forces between adjacent tubes, which result from their high curvature. In the case of intermediate and large-diameter MWCNTs, the interlayer spacing varies based on the innermost tube's diameter with an asymptotic limit of 0.344 nm [49]. Moreover, the turbostratic stacking of the constituent

shells in the MWCNT facilitate slipping of adjacent graphene shells, reducing the shear modulus due to the weak van der Waals interactions [50]. Therefore, the degree of oxidation and unzipping rates for nanotubes with different diameters are expected to vary.

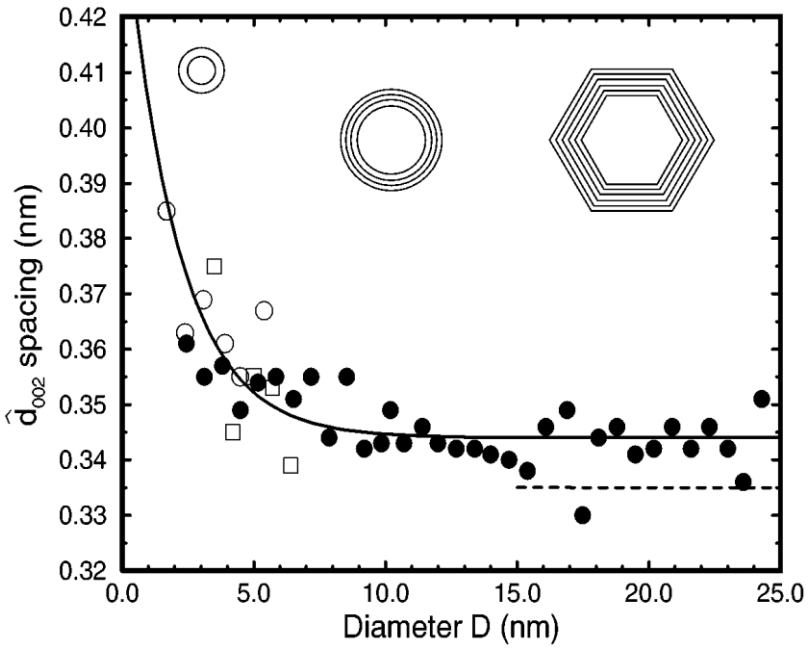

Figure 1.17: Effect of MWCNT diameter in interlayer spacing and tubes properties [49].

Herein, in chapter 2 we investigate the effect of the suspension period in H_2SO_4 on various diameters of MWCNTs using the longitudinal unzipping method to produce GONRs for potential sensor applications. The resultant GONR products were characterized by observing their surface morphology, analyzing their degree of oxidation, and disorder density in comparison to their respective MWCNT precursors. Finally, the applicability of the obtained GONRs as electrode materials was evaluated by the electrochemical detection of hydrogen peroxide (H_2O_2) and β-nicotinamide adenine dinucleotide dehydrogenase (NADH), which are commonly used in evaluating biosensor systems.

1.4 Organization of thesis

This thesis starts with a brief introduction to biosensors and the materials used in this research including gold nanoparticles (AuNPs) and graphene oxide nanoribbons (GONRs). In chapter 2, the factors that affect the rate of unzipping and oxidation degree are discussed thoroughly, specifically on multi-walled carbon nanotube (MWCNT) diameter and pre-oxidation time. Subsequently, a report on the performance of the produced GONRs as electrode materials in electrochemical biosensors is presented. In chapter 3, the tuning of AuNP catalytic activity by GONR as a supporting matrix in a non-enzymatic glucose sensor at neutral conditions is reported. Then, a thorough study on ECL of isoluminol-functionalized AuNP on GONR and a proposed ECL mechanism are described in chapter 4. The potential applications of isoluminol-functionalized AuNP with GONR on modified screen printed electrodes in enzymatic biosensor are demonstrated. Finally, a summary on the findings and future remarks are given in chapter 5.

1.5 References

[1] A.P.F. Turner, Biosensor: sense and sensibility, *Chem. Soc. Rev.* **42** (2013) 3184.

[2] C.R. Lowe, An introduction to the concepts and technology of biosensors, *Biosensors* **1** (1985) 3.

[3] N.J. Ronkainen, H.B. Halsall, W.R. Heineman, Electrochemical biosensor, *Chem. Soc. Rev.* **39** (2010) 1747.

[4] J.E. Frew, H.A.O. Hill, Electrochemical biosensors, *Anal. Chem.* **59** (1987) 933.

[5] F.W. Scheller, R. Hintsche, D. Pfeiffer, F. Schubert, K. Riedel, R. Kindervater, Biosensors: Fundamental, Applications and Trends, *Sensors and Actuators B* **4** (1991) 197.

[6] A.J. Bard, L.R. Faulkner, *Electrochemical Methods Fundamentals and Applications*, John Wiley & Sons, Inc., 2nd edn. (2001).

[7] K. Kerman, M. Saito, S. Yamamura, Y. Takamura, E. Tamiya, Nanomaterial-based electrochemical biosensor for medical applications, *Trends in Analytical Chemistry* **27** (2008) 585.

[8] W. Miao, Electrogenerated chemiluminescence and its biorelated applications, *Chem. Rev.* **108** (2008) 2506.

[9] A.J. Bard, *Electrogenerated Chemiluminescence*, Marcel Dekker, Inc., 10th edn. (2004).

[10] L. Hu, G. Xu, Applications and trends in electroclemiluminescence, *Chem. Soc. Rev.* **39** (2010) 3275.

[11] M.M. Richter, Electrochemiluminescence (ECL), *Chem. Rev.* **104** (2004) 3003.

[12] D. Grieshaber, R. MacKenzie, J. Vörös, E. Reimhult, Electrochemical Biosensors - Sensor Principles and Architectures, *Sensors* **8** (2008) 1400.

[13] J. Wang, nanomaterial-based electrochemical biosensors, *Analyst* **130** (2005) 421.

[14] W. Yang, K.R. Ratinac, S.P. Ringer, F. Braet, Carbon nanomaterials in biosensors, *Angew. Chem. Int. Ed.* **49** (2010) 2114.

[15] X. Yang, B. Feng X. He, F. Li, Y. Ding, J. Fei, Carbon nanomaterial based electrochemical sensors for biogenic amines, *Microchim Acta* **180** (2013) 935.

[16] F. Patolsky, Y. Weizmann, I. Willner, Long-Range Electrical Contacting of Redox Enzymes by SWCNT Connectors, *Angew. Chem. Int. Ed.* **43** (2004) 2113.

[17] X. Luo, A. Morrin, A.J. Killard, M.R. Smyth, Application of nanoparticles in electrochemical sensors and biosensors, *Electroanalysis* **18** (2006) 319.

[18] K. Idegami, M. Chikae, K. Kerman, N. Nagatani, T. Yuhi, T. Endo, E. Tamiya, Gold Nanoparticle-Based Redox Signal Enhancement for Sensitive Detection of Human Chorionic Gonadotropin Hormone, *Electroanalysis* **20** (2008) 14.

[19] S. Guo, E. Wang, Synthesis and electrochemical applications of gold nanoparticles, *Anal. Chim. Acta* **598** (2007) 191.

[20] M. Haruta, When gold is not noble: catalysis by nanoparticles, *The Chemical Record* **3** (2003) 75.

[21] A. Corma, H. Garcia, Supported gold nanoparticles as catalyst for organic reactions, *Chem. Soc. Rev.* **37** (2008) 2096.

[22] J.M. Pingarrón, P. Yáñez-Sedeño, A. González-Cortés, Gold nanoparticle-based electrochemical biosensors, *Electrochimica Acta* **53** (2008) 5848.

[23] G. Schmid, Large clusters and colloids, *Chem. Rev.* **92** (1992) 1709.

[24] G. Schmid, L.F. Chi, Metal clusters and colloids, *Adv. Mater.* **10** (1998) 515.

[25] M. Brust, M. Walker, D. Bethell, D.J. Schiffrin, R.J. Whyman, Synthesis of thiol-derivatised gold nanoparticles in a two-phase Liquid–Liquid system, *J. Chem. Soc. Chem. Commun.* **7** (1994) 801.

[26] M. Brust, J. Fink, D. Bethell, D.J. Schiffrin, C.J. Kiely, Synthesis and reactions of functionalised gold nanoparticles, *J. Chem. Soc. Chem. Commun.* **16** (1995) 1655.

[27] J. Naruse, L.Q. Hoa, Y. Sugano, T. Ikeuchi, H. Yoshikawa, M. Saito, E. Tamiya, Development of biofuel cells based on gold nanoparticle decorated multi-walled carbon nanotubes, *Biosensors & Bioelectronics* **30** (2011) 204.

[28] D. Tian, H. Zhang, Y. Chai, H. Cui, Synthesis of *N*-(aminobutyl)-*N*-(ethylisoluminol) functionalized gold nanomaterials for chemiluminescent bio-probe, *Chem. Commun.* **47** (2011) 4959.

[29] T. Ishimoto, Y. Hamatake, H. Kazuno, T. Kishida, M. Koyama, Theoretical study of support effect of Au catalyst for glucose oxidation of alkaline fuel cell anode, *Applied Surface Science* **324** (2015) 76.

[30] Z.F. Zhang, H. Cui, C.Z. Lai and L.J. Liu, Gold nanoparticle-catalyzed luminol chemiluminescence and its analytical application, *Anal. Chem.* **77** (2005) 3324.

[31] E. Katz, I. Willner, Integrated Nanoparticle–Biomolecule Hybrid Systems: Synthesis,

Properties, and Applications, *Angew. Chem. Int. Ed.* **43** (2004) 6042.

[32] J. Manso, M.L. Mena, P. Yáñez-Sedeño, J.M. Pingarrón, Electrochemical biosensors based on colloidal gold–carbon nanotubes composite electrodes, *J. Electroanal. Chem.* **603** (2007) 1.

[33] G. Goncalves, P.A.A.P. Marques, C.M. Granadeiro, H.I.S. Nogueira, M.K. Singh, J. Grácio, Surface modification of graphene nanosheet with gold nanoparticles: the role of oxygen moieties at graphene surface on gold nucleation and growth, *Chem. Mater.* **21** (2009) 4796.

[34] A.K. Geim, K.S. Novoselov, The rise of graphene. *Nat Mater* **6** (2007) 183.

[35] S. Park, R.S. Ruoff, Chemical methods for the production of graphenes. *Nat Nanotechnol* **4** (2009) 217.

[36] M.J. Allen, V.C. Tung, R.B. Kaner, Honeycomb Carbon: A review of graphene. *Chem. Rev.* **110** (2010) 132.

[37] K.S. Novoselov, A.K. Geim, S.V. Morozov, D. Jiang, Y. Zhang, S.V. Dubonos, I.V. Grigorieva, A.A. Firsov, Electric field effect in atomically thin carbon films. *Science* **306** (2004) 666.

[38] C.N.R. Rao, A.K. Sood, R. Voggu, K.S. Subrahmanyam, Some novel attributes of graphene. *J. Phys. Chem. Lett.* **1** (2010) 572.

[39] T. Kuila, S. Bose, A.K. Mishra, P. Khanra, N.H. Kim, J.H. Lee, Chemical functionalization of graphene and its applications. *Prog. Mater. Sci.* **57** (2012) 1061.

[40] D. Chen, H. Feng, J. Li, Graphene oxide: preparation, functionalization and electrochemical applications. *Chem. Rev.* **112** (2012) 6027.

[41] D.A.C. Brownson, C.E. Banks. Graphene electrochemistry: fabricating amperometric biosensor. *Analyst* **136** (2011) 2084.

[42] D.A.C Brownson, A.C. Lacombe, M. Gómez-Mingot, C.E. Banks. Graphene oxide gives

rise to unique and intriguing voltammetry. *RCS Advances* **2** (2012) 665.

[43] P.M. Hallam, C.E. Banks, Quantifying the electron transfer sites of graphene, *Electrochemistry Communication* **13** (2011) 8.

[44] A.L. Higginbotham, D.V. Kosynkin, A. Sinitskii, Z. Sun, J.M. Tour, Lower-defect graphene oxide nanoribbons from multiwalled carbon nanotubes. *ACS Nano* **4** (2010) 2059.

[45] M. Terrones, Nanotubes unzipped, *Nature* **458** (2009) 845.

[46] D.V. Kosynkin, A.L. Higginbotham, A. Sinitskii, J.R. Lomeda, A. Dimiev, B.K. Price, J.M. Tour, Longitudinal unzipping of carbon nanotubes to form graphene nanoribbons. *Nature* **458** (2009) 872.

[47] A.M. Dimiev, J.M. Tour, Mechanism of graphene oxide formation. *ACS Nano* **8** (2014) 3060.

[48] S. Iijima, Helical microtubules of graphitic carbon. *Nature* **354** (1991) 56.

[49] C.H. Kiang, M. Endo, P.M. Ajayan, G. Dresselhaus, M.S. Dresselhaus, Size effect in carbon nanotubes. *Phys. Rev. Lett.* **81** (1998) 1869.

[50] X. Sun, C.H. Kiang, M. Endo, K. Takeuchi, T. Furuta, M.S. Dresselhaus, Stacking characteristics of graphene shells in carbon nanotubes. *Phys. Rev. B* **54** (1996) 629.

CHAPTER 2

EFFECT OF MWCNT DIAMETER AND CHEMICAL OXIDATION TIME ON FORMATION AND PERFORMANCE OF GRAPHENE OXIDE NANORIBBONS FOR ELECTROCHEMICAL BIOSENSOR APPLICATIONS

2.1 Introduction

Graphene is a single atomic layer of carbon atoms in an sp^2 hexagonal bonding configuration that is the basic building block for other carbon materials [1]. Considerable research has been conducted on graphene since its first introduction by Geim and Novoselov, in order to develop scalable synthesis methods [2-3] and improve material properties [4-5] and functionalities [6-7]. The properties and possible applications of graphene based materials depend greatly on their synthesis procedure (mechanically or chemically generated) [6]. Both the mechanical exfoliation and the high-temperature growth techniques can produce high quality graphene with low throughput, but at a high cost [2]. In contrast, the chemically derived approach yields high throughput graphene with graphitic defects at a low cost [2]. An electrochemical performance analysis of mechanically and chemically derived graphene demonstrates that pristine graphene has a lower catalytic activity than graphene oxide or bulk graphite [8-9]. Furthermore, it is expected that the reactive edges and structural defects or impurities are beneficial for electrochemical activity [8-9]. Hence, we have chosen to focus on graphene oxide nanoribbons (GONRs), which contain various oxygen-based functional groups on both the basal plane and straight edges of the graphene strip, for use in electrochemical sensors.

Recently, graphene nanoribbons (GNRs) have been produced by a chemical unzipping of multiwalled carbon nanotubes (MWCNTs) [10]. The advantages of this method include the

ability to control the graphene layer number based on the selected MWCNT diameter and the uniformity of the resultant nanoribbon structure. Several well-known techniques for producing GNRs include treating MWCNT with oxidizing agents under acidic conditions followed by a reduction process [11], etching by an argon plasma [12], exfoliation based on the intercalation of alkali-metal atoms [13], and cleaving with catalytic metal nanoparticles [14]. Among the aforementioned methods, the longitudinal unzipping of MWCNTs through the oxidizing process, proposed by Kosynkin et al. [11], is extremely simple, efficient, and potentially scalable for producing exfoliated graphene sheets. This unzipping method involves suspending the MWCNTs in concentrated sulfuric acid (H_2SO_4) for 1–12 h followed by a potassium permanganate ($KMnO_4$) treatment. They determined that their method gained a high degree of consecutive tube openings when high amounts of $KMnO_4$ were used. Since the unzipping process is oxidative, the resultant nanoribbons possess various types of oxygen-based functional groups at their edges and on their graphitic surfaces, similar to graphene oxide (GO). Therefore, these nanoribbons are termed graphene oxide nanoribbons (GONRs). Furthermore, the GONRs are highly soluble in water without the assistance of dispersing agents, and form stable colloids due to the electrostatic repulsion from the carboxylic and hydroxyl groups present on the GONR surface [15]. With these interesting properties, GONRs hold significant potential through a facile surface modification to chemically functionalize them for use in electrochemical sensor applications.

In order to achieve fully unzipped MWCNTs on a large scale, several optimization studies have been performed, starting with optimization of the quantity of oxidizing agent, $KMnO_4$ [11]. Further optimization of this method focused on varying the acid medium, reaction temperature, and $KMnO_4$ reaction time in order to form GONRs with fewer defects [16]. Through their experiments, they confirmed that a sufficient amount of H_2SO_4 (about 90 vol%) was crucial for the complete formation and exfoliation of nanoribbons, while the

addition of a second acid (about 10 vol%) could enhance the GONR quality. The suspension of the MWCNTs in concentrated H_2SO_4 prior to $KMnO_4$ treatment is believed to allow penetration and intercalation of the H_2SO_4, enhancing the oxidation process of the oxidizing agents. Recent reports on the mechanism of graphene oxide formation from bulk graphite using a modified Hummer's method revealed that the first step was the conversion of graphite to a sulfuric acid–graphite intercalation compound (H_2SO_4-GIC) followed by the conversion of the GIC to the oxidized form of graphite (pristine graphite oxide, PGO) by permanganate, and finally the formation of GO by the reaction of PGO with water [17]. The formation of the H_2SO_4-GIC was described as beginning immediately upon exposure of the graphite to the acid medium, while the conversion of GIC to PGO was slower depending on the graphite source. In comparison to graphite, MWCNTs as the starting material have a unique 2D structure, with diameters ranging from 2 to 500 nm and lengths from 50 nm to a few mm. The MWCNTs contain several concentric coaxial graphene cylinders with an interlayer spacing of 0.34 nm, similar to graphite [18]. However, studies have shown that this interlayer spacing increases with a decreasing nanotube diameter [19]. Smaller nanotube diameters have a higher interlayer spacing due to the large repulsive forces between the adjacent tubes resulting from their high curvature. In the case of intermediate and large-diameter MWCNTs, the interlayer spacing varies based on the innermost tube's diameter with an asymptotic limit of 0.344 nm [19]. Moreover, the turbostratic stacking of the constituent shells in the MWCNT facilitate slipping of adjacent graphene shells, reducing the shear modulus due to the weak van der Waals interactions [20]. Therefore, the degree of oxidation and unzipping rates for nanotubes with different diameters are expected to vary.

Herein, we investigate the effect of the suspension period in H_2SO_4 on various diameters of MWCNTs using the longitudinal unzipping method to produce GONRs for potential sensor applications. To the best of our knowledge, this is the first study on the

unzipping rate of various MWCNTs diameters. The unzipping technique was applied to three diameters of MWCNTs, representing small (3–20 nm), medium (40–70 nm) and large (110–170 nm) diameter. These selected MWCNTs were then suspended in concentrated H_2SO_4 for 3, 6, or 12 h prior to the $KMnO_4$ treatment. The resultant GONR products were characterized by observing their surface morphology, analyzing the degree of oxidation, and disorder density compared with their respective MWCNT starting materials. Finally, the applicability of the obtained GONRs was evaluated by the electrochemical detection of hydrogen peroxide (H_2O_2) and β-nicotinamide adenine dinucleotide dehydrogenase (NADH), which are commonly evaluated in biosensor systems.

2.2 Experimental Procedure

2.2.1 Materials and reagents

MWCNTs with a diameter of 3–20 nm (S) and 40–70 nm (M), the concentrated H_2SO_4, $KMnO_4$, 30% hydrogen peroxide (H_2O_2), ethanol, ether, and potassium ferricyanide ($K_3[Fe(CN)_6]$) were obtained from Wako Pure Chemical Industries, Ltd., Japan. MWCNTs with a diameter of 110–170 nm (L), potassium chloride (KCl), and carbon sheets (CS) were purchased from Sigma-Aldrich, USA. The β-nicotinamide adenine dinucleotide (NADH) was obtained from Oriental Yeast Co. Ltd., Japan. The phosphate buffer solution (PBS, 0.1 mol·L^{-1}, pH 7.0) was prepared from KH_2PO_4 and K_2HPO_4 from Sigma-Aldrich, USA. Ultrapure water was obtained from a Barnstead Nanopure water purification system (18 MΩ, Thermo Scientific, USA) and was used in all experiments.

2.2.2 GONR synthesis and characterization

To synthesize the GONRs, the different types of MWCNTs were exposed separately for longitudinal unzipping by suspending them in concentrated H_2SO_4 and then treating them

with $KMnO_4$ [11]. Three sizes of commercial MWCNTs were used in this experiment; the small size MWCNTs (MWCNT_S) have diameters between 3–20 nm, the medium size (MWCNT_M) have diameters of 40–70 nm, and the large size (MWCNT_L) have diameters of 110–170 nm. The MWCNTs were suspended in concentrated H_2SO_4 for 3, 6, or 12 h, followed by treatment with 500 wt% $KMnO_4$. The mixture was stirred at room temperature for 1 h and then heated between 55 to 70 °C for an additional 1 h. After all of the $KMnO_4$ was consumed, the mixture was quenched by pouring it onto ice containing a small amount of H_2O_2. The solution was then filtered through a polytetrafluoroethylene (PTFE) membrane. The remaining solid was washed with HCl and ethanol/ether alternately between filtrations. The final product was dried *in vacuo*.

All of the GONR products were imaged by scanning electron microscopy (SEM) using a Strata DB 235 microscope (FEI Co.) The GONR products' degrees of oxidation were examined by an attenuated total reflection Fourier Transform reflection infrared (ATR-FTIR) spectroscopy (FT-720, Horiba, Japan). Meanwhile, Raman Spectroscopy (Raman-11, Nanophoton Corp., Japan) was used to check the structure and topology of the MWCNTs and GONRs. The degree of remaining π-conjugation in the GONR after the oxidation process was determined by a UV-Vis spectrophotometer (UV-2550, Shimadzu, Japan).

2.2.3 GONRs in biosensor applications

The electrochemical performances of GONR-based electrodes were evaluated with an Autolab potentiostat/galvanostat PGSTAT12 (Metrohm/Eco Chemie, Netherlands). The working electrode was fabricated by decorating carbon sheet (CS) substrates with the GONR materials (GONR/CS) by the drop cast method. First, 0.5 mg of the GONRs were sonicated and dispersed in 1 mL of ethanol. Then, the mixture was drop cast on the surface of a 1 cm^2 cleaned carbon sheet and dried at 60 °C for 1 h. To clean the surface of the GONR/CS, the

electrode was subjected to a thermal treatment at 400 °C for 2 h. A three-electrode cell was used for all electrochemical measurements, with a platinum coil as the counter electrode, Ag/AgCl as the reference electrode (BAS Inc., Japan), and the prepared GONR/CS as the working electrode.

2.3 Results and Discussion

2.3.1 Morphology inspection

0.5 mg/mL samples of each GONR products and MWCNT starting material were sonicated thoroughly in ethanol before deposition on carbon sheets. Then, the fabricated samples were heated at 400 °C for 2 h before the SEM imaging. The resultant GONR surface morphologies are summarized in Table 2.1. The lengthwise cutting and unraveling of the nanotube sidewalls was observed on the as-prepared GONRs and compared to the MWCNT starting materials. As shown in the figures of Table 1, the rate of unzipping to yield straight edge nanoribbons was clearly affected by the MWCNT diameter and their suspension time in concentrated H_2SO_4 prior to the permanganate introduction. Initially, GONRs obtained from the MWCNT_S show only a minor degree of opening, concentrated either in the center or in tears at the end of the nanotubes, regardless of the H_2SO_4 suspension time. Meanwhile, the GONRs derived from the MWCNT_M gradually produced fully opened nanoribbons as the H_2SO_4 suspension time was increased. On the other hand, GONRs derived from the MWCNT_L formed huge exfoliated sheets, where the size was independent of H_2SO_4 exposure time. These results suggest that the MWCNT_S suffer from unzipping difficulty compared to the MWCNT_M and MWCNT_L, and this may be due to high van der Waals interactions from the adjacent coaxial graphene basal planes, especially for nanotubes with radii below 7 nm [21]. Moreover, incomplete unzipping of the MWCNT_S was observed even after increasing the reaction time in the concentrated H_2SO_4, indicating a low formation

of the GIC-H_2SO_4 intermediate, which then resulted in a low oxidation efficacy to break apart the graphitic plane. Furthermore, the SEM images demonstrate that most of the unzipping process takes place at the ends of the nanotubes rather than at the planar walls, suggesting there is a greater reactivity in the existing defects at the MWCNT_S end caps [22].

Table 2.1. SEM images of GONR products.

Parameters		**Diameter of MWCNT**		
		S	**M**	**L**
Acid Treatment Time (hours)	**0**	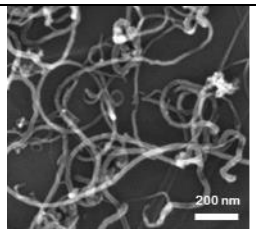 MWCNT_S 3–20 nm	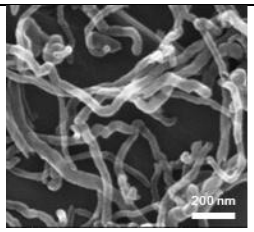 MWCNT_M 40–70 nm	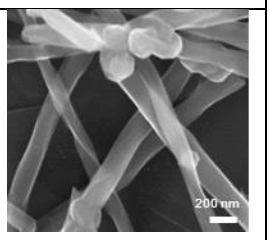 MWCNT_L 110–170 nm
	3	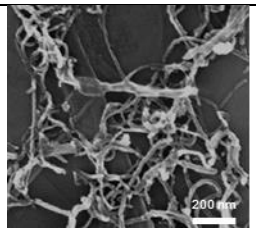 Stacked tubes Minor unzipped	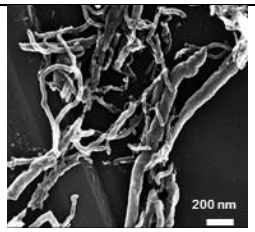 Stacked ribbons & tubes Partially opened	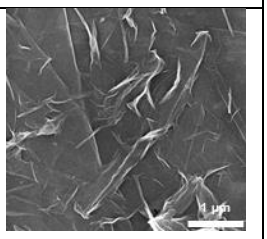 Exfoliated ribbons Fully opened
	6	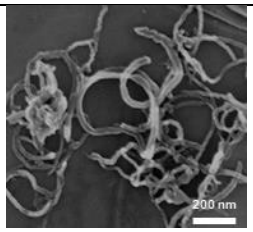 Stacked tubes Minor unzipped	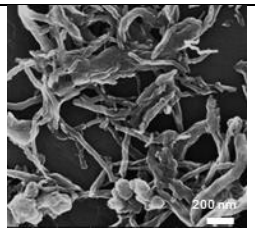 Stacked ribbons & tubes Partially opened	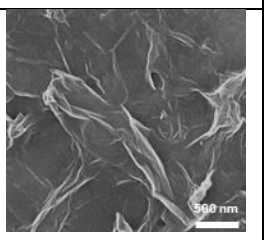 Exfoliated ribbons Fully opened
	12	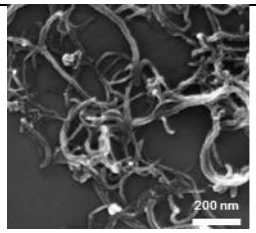 Stacked tubes Minor unzipped	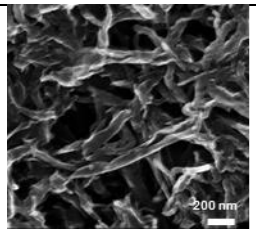 Stacked ribbons Fully opened	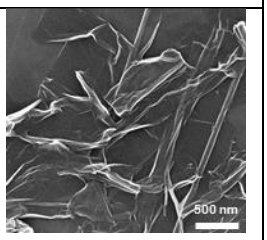 Exfoliated ribbons Fully opened

In contrast to the MWCNT_S, the GONRs produced from the MWCNT_M that underwent less than 12 h of acid treatment had remaining unzipped inner tubes intertwined with thick nanoribbon stacks. Meanwhile, the MWCNT_M that underwent more than 12 h of acid treatment (GONR12M) were able to completely unzip all of the MWCNT layers, but these still consisted of multi-stack graphene layers. The unzipped MWCNT_M have a slightly curved morphology to their layers instead of flat nanoribbons. These results confirmed that the unzipping process initiated from the outermost layer of the MWCNT, with the long acid treatment time facilitating the complete opening of all MWCNT layers [11]. The irregular GONR surface morphology produced by the MWCNT_M may result from the graphene pieces flaking off from wall defects during sonication [22]. Nevertheless, a low degree of GONR exfoliation was observed even after a 12 h suspension time in H_2SO_4. This result demonstrates a slow diffusion rate of the permanganate into the MWCNT_M, leading to a slow disruption of the graphene lattice to increase the interlayer spacing [17]. Consequently, strong van der Waals forces prevent the GONR layers from undergoing a chemical-mechanical breaking during sonication. In the case of the MWCNT_L, the resultant GONRs are huge straight edged nanoribbons, even with the minimum exposure time in concentrated H_2SO_4. These results clearly demonstrate a high rate of MWCNT_L unzipping due to a greater number of defects at the end caps, coupled with the large curved surface area that together serve as reactive sites for oxidation [22]. Moreover, the complete unzipping of all MWCNT_L nanotube layers confirmed the easy penetration of H_2SO_4 to form the GIC-H_2SO_4 intermediate, resulting in a faster diffusion rate of the oxidizing agent to oxidize the nested graphene cylinders [17]. The SEM images also reveal that the GONRs produced from MWCNT_L at a longer suspension period in the H_2SO_4 (GONR12L) tended to form a fractured graphene sheet seam between the separated lattice fragments through oxygen atom bridging [23]. These oxygen-zipped ridges produce a crumpling of the GONR sheet.

Furthermore, a long oxidation treatment with the strong acid also caused the GONR12L to fracture into shorter segments.

In summary, our analysis revealed that the unzipping rate was dependent on the diameter of the MWCNTs, as MWCNT_L > MWCNT_M > MWCNT_S. The effect of increasing the MWCNT suspension time in concentrated H_2SO_4 was not apparent for the MWCNT_S and MWCNT_L, but it significantly improved the unzipping rate of the MWCNT_M. Other factors that might also affect the unzipping rate are number of nanotube layers and innermost nanotube diameter. The different MWCNT diameters affect the permanganate diffusion rate into the nanotube layers, which subsequently contributed to the varied degree of oxidation degree. To detail the degree of oxidation as well as the structural changes, FTIR measurements were taken of all samples with the results discussed in the following section.

2.3.2 FTIR characterization

The oxidative unzipping of the MWCNTs is caused by oxygen atoms randomly attaching to the honeycomb lattice, primarily at the defect or edge sites, forming an epoxy bridge that joins two adjacent carbon atoms [24]. This three-membered epoxide is severely strained due to the configuration changes that occur as the planar sp^2-hybridized orientation switches to a distorted sp^3-hybridized geometry. Therefore, the cooperative alignment of the epoxy groups induces sufficient tension in the underlying lattice to break the native carbon bonds [24]. The opening sites of the nanotubes are expected to be decorated with ketones that can then be converted to carboxylic groups [11]. On the other hand, MWCNTs with different diameters, having different numbers of layers, were predicted to show a diverse degree of oxidation, as the oxidation reaction rate of the MWCNT's innermost layers is considerably slower than that of the outermost layers [25]. Furthermore, the variation in the oxidation rate between the

layers may affect the GONR sheet exfoliation due to low intercalation of oxygen functional groups, leading to a small spacing displacement that is insufficient to overcome the van der Waals forces.

In order to examine the degree of oxidation for the GONR derived from MWCNTs with different diameters and varied acid treatment time, we prepared a thin layer of each material by dropping a 0.5 mg/mL GONR or MWCNT precursor solution in ethanol on the ATR's diamond surface and allowing it to dry. Before the catalyst deposition, the control sample was analyzed first in "background mode" then "sample mode". The background was subtracted from the sample mode signal allowing us to distinguish the surrounding air peaks (Fig. 2.1 (A)) at ~2300 cm^{-1} that attributed to the asymmetric vibration stretch of CO_2, while the noisy signals in the regions 3400–4000 cm^{-1} and 1300–1900 cm^{-1} were derived from water vapor [26-27]. In addition, all GONR spectra (Fig. 2.1 (B-D)) showed the common hydroxyl band at ~3420 cm^{-1} (i) for the COO-H/O-H stretching [25-28] in addition to three strong carbonyl bands at ~1700 cm^{-1} (ii) for C=O stretching [25-28], ~1564 cm^{-1} (iii) for –COO- asymmetric stretching [26], and ~1209 cm^{-1} (iv) for C-O stretching [25,28]. In comparison, all MWCNT spectra (Fig. 2.1 (A)) displayed no common hydroxyl (i) or carbonyl (ii-iv) peaks, indicating that all GONR products had undergone the oxidation process. The GONR obtained from the MWCNT_S had the lowest hydroxyl band (i) intensity with a relatively high carbonyl band (ii-iv) intensity, whereas the GONR derived from the MWCNT_M showed an incremental increase in both the carbonyl (ii-iv) and hydroxyl (i) peak intensities compared to the GONR from the MWCNT_S. Meanwhile, the GONR produced from the MWCNT_L had a nearly equivalent carbonyl peak intensity (ii-iv) to that of the other GONRS, but with the highest hydroxyl peak intensity (i). These results suggest that the MWCNT_S suffered from a low degree of oxidation, leading to partial or minimally unzipped MWCNTs, and therefore the hydroxyl groups were expected to appear at the

nanotube ends' torn edges, as imaged by the SEM in Table 2.1. A higher degree of oxidation was observed in the case of the MWCNT_M, indicated by the appearance of ketone groups, which produce fully unzipped nanotubes, but with a low intercalation of hydroxyl groups on the graphitic surface, and therefore a low exfoliation rate between the MWCNT layers. The GONR produced by the MWCNT_L had the highest degree of oxidation, a completed oxidation process that resulted in a high amount of carboxylic groups due to ketone protonation, as observed by the strong hydroxyl band intensity [11].

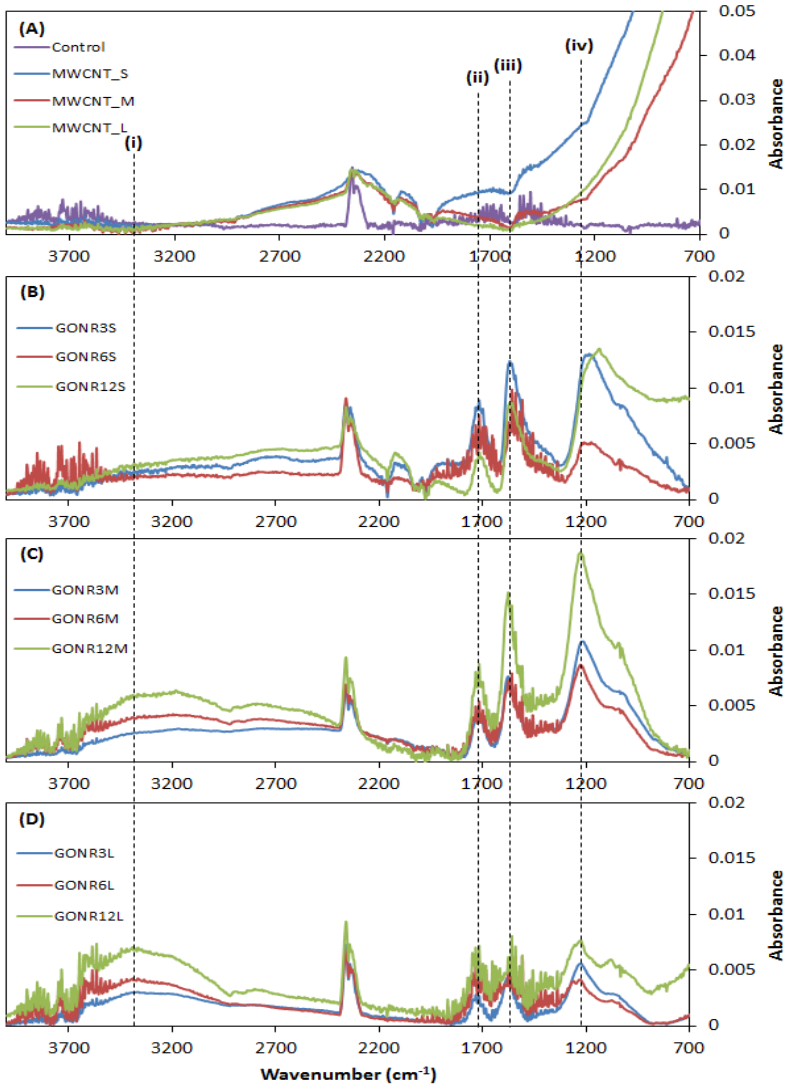

Figure 2.1: ATR-FTIR spectra of (A) MWCNTs with different diameters, and GONR derived from (B) MWCNT_S, (C) MWCNT_M, and (D) MWCNT_L at varied suspension times in concentrated H_2SO_4.

With regard to the effect of the acid treatment time, the degree of oxidation for the produced GONRs increased with increasing suspension time in concentrated H_2SO_4 for all types of MWCNTs. The FTIR spectra of the GONRs synthesized from the MWCNT_S (Fig. 1B) showed a slight increase in the hydroxyl band (i) as the suspension time in H_2SO_4 was increased from 3 to 12 h. However, a strong carbonyl band (ii–iii) was observed for a short suspension period in H_2SO_4, and the C-O moiety band (iv) had the strongest absorbance intensity at the 3 and 12 h of acid treatment times. These results imply that different acid treatments periods contribute to different amounts of the H_2SO_4-GIC intercalate that react strongly with the large phenolic groups produced under strong $KMnO_4$ oxidation in H_2SO_4. As the oxidation process proceeds, the majority of these phenolic groups likely condense to form C-O-C ether linkages or epoxy bridges (iv) in order to rupture the graphitic lattice. A small portion of the phenolic groups at the edges or at defect sites were oxidized to ketone or quinone groups (ii–iii), and subsequently, only a few ketone groups are converted to carboxylic groups, as referred to in (i–iii). Since there is a low intensity of the O-H band (i), we can conclude that band (iv) mainly contributed to epoxy bridges that failed to crack the graphitic lattice, and carbonyl groups (ii–iii) primarily decorated the edges of the nanotubes' end caps. On the other hand, the GONR produced from the MWCNT_M (Fig. 1C) shows a strong absorbance intensity of bands (i–iv) as the suspension period in concentrated H_2SO_4 was increased, especially the GONR12M sample. The significant increase in bands (i) and (iv) indicates the presence of hydrated surface oxides from O-H deformation and C-O stretching that may be attributed to phenols, hydroquinones, and aromatic carboxylic groups. Carbonyl bands (ii–iii) of the GONR synthesized after 3 and 6 h of exposure in H_2SO_4 (GONR3M and GONR6M) have nearly identical intensities while band (iv) shows a high variation in intensity between acid treatment times. The GONR3M and GONR6M possess low band (i) and high band (iv), indicating that C-O-C bridges were formed by an incomplete

unzipping process. In addition, the oxidative unzipping of MWCNT_L (Fig. 1D) produced GONR with nearly equivalent absorbance intensities for all bands (i–iv) depending on the acid treatment time. The intensities of the hydroxyl, carbonyl, and ether bands increased proportionally with longer acid treatment time, suggesting that the MWCNT_L has the highest rate of oxidation and unzipping to form the GONR.

In conclusion, the pristine MWCNT properties such as diameter can have a significant effect on the degree of oxidation, and therefore the unzipping rate. Moreover, long acid treatment times increase the degree of oxidation and hydrophilicity of the GONR product. A high hydrophilicity is vital for promoting exfoliation, particularly for creating fully unzipped MWCNT. These results reveal that the order of increased degree of oxidation is MWCNT_L > MWCNT_M > MWCNT_S and 12 h > 6 h > 3 h. The oxidative unzipping process introduces of defects and disorder on the graphitic lattice, as investigated in the following sections.

2.3.3 Raman analysis

Raman spectroscopy has been widely used to characterize carbonaceous materials and evaluate the degree of disorder in their structure [30]. The relative degree of structural defects and disorder in graphene is usually evaluated by analyzing the intensity ratio between the disorder-induced D band and the sp^2-reduced G band (I_D/I_G) [31]. To investigate the defects and disorder of the prepared GONRs compared to their pristine MWCNT precursors, a few drops of 0.5 mg/mL individual solutions of either the GONRs or MWCNTs in ethanol were cast onto quartz micro-glasses. After drying, the sample was observed using the 514 nm wavelength at room temperature. Fig. 2.2 (A) displays the Raman spectrum of pristine MWCNT_L, showing the obvious G band (1565 cm^{-1}) resulting from the MWCNTs' highly crystalline structure and a minimal D band (1331 cm^{-1}) of amorphous or disordered carbon

[30-31]. In contrast, the GONR materials formed from the MWCNT_L show a broadened G band after the oxidation process along with the appearance of the D band. This identifies a reduction of the in-plane sp^2 domain size and an increasing level of disorder in the GONR due to the oxidation process [11]. Furthermore, this result correlates with the FTIR data in Fig. 2.1 (D), where the oxidative unzipping of MWCNT_Ls by various acid treatment times produced oxygen-based functional groups along the edges and basal planes, reducing the honeycomb lattice structure.

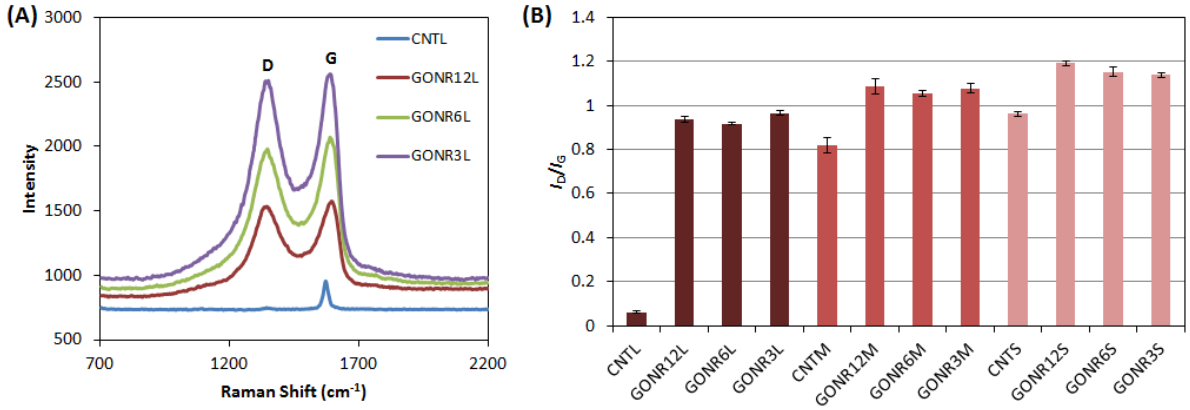

Figure 2.2: (A) Raman spectra of the GONRs and their MWCNT_L precursor with various suspension times in H_2SO_4. (B) The D to G band peak intensity ratio (I_D/I_G) with error bars indicating the standard deviation of six I_D/I_G ratios across each sample.

The chemically modified MWCNTs have higher I_D/I_G ratios than pristine MWCNTs as depicted in Fig. 2.2 (B) due to the high degree of induced defects and disorder. Among the pristine MWCNTs, the MWCNT_L had the lowest I_D/I_G ratio compared to MWCNT_M and MWCNT_S because of graphitization, which results in a polygonal cross section with low structural defects [19]. Interestingly, the average I_D/I_G ratios of the GONR derived from the different MWCNT diameters, following an order of MWCNT_S > MWCNT_M > MWCNT_L, inferring an identical trend for the degree of defects and disorder in these products. The degree of defects in the GONRs produced from the MWCNT_L was about

176% higher than their starting material, with the I_D/I_G ratio of the GONR3L being higher than that of GONR6L and GONR12L. These results indicate that the MWCNT_L is easily oxidized even after a very short exposure time to acid, and it has few original defects that act as reactive sites in the oxidation process. Since the MWCNT_L has a much larger diameter, the resultant GONRs also have larger remaining sp^2 domains than the disorder domains, which consequently contributes to their low I_D/I_G ratios compared to GONRs derived from the MWCNT_M and MWCNT_S. In contrast, the MWCNT_S precursor produced 19% of structural defects on the GONR, and increased the disorder level along with increased acid treatment time. These results confirm that the smaller diameter nanotubes are less reactive and result in a low oxidation rate [25]; hence, the longer suspension time in H_2SO_4 provides more intercalant species and defects to promote the oxidation-based unzipping process. In the case of the GONRs synthesized from the MWCNT_M, the degree of defects was about 27%, with small variations in the I_D/I_G ratio across the varied concentrated H_2SO_4 suspension times. This result is in agreement with the FTIR data in Fig. 1B, where the GONR12M and GONR3M demonstrated a high degree of oxidation by the presence of hydroxyl and epoxy bridges, respectively, which also led to high disorder levels. As the GONR conductivity is directly affected by structural defects and disorder, the remaining amount of π-conjugation in the GONRs was investigated and discussed in the following section.

2.3.4 Investigation on the degree of conjugation

The characterization of the GONR by FTIR revealed that the MWCNTs underwent the oxidation process while the Raman spectra showed that the GONRs had increased disorder and oxygen-based functional group defects. Thus, the level of π-conjugation remaining in the GONR can be determined by the λ_{max} of its absorption when dispersed in DI water using a UV-Vis spectrophotometer. The absorption peak, λ_{max} of the GONRs produced from the

MWCNT_L with various acid treatment times (Fig. 3A) and of GONRs synthesized from various MWCNT diameters at 6 h of suspension in concentrated H_2SO_4 (Fig. 3B) appeared around 240–260 nm. A shoulder around ~300 nm can be observed and attributed to the *n*-π* transition of the carbonyl groups. It is known that highly conjugated graphene-like materials have an λ_{max} at ~275 nm while, materials with a disrupted π-network and greater number of sp^3 carbons have a blue shifted λ_{max} (~235 nm) [16, 24]. Based on Fig. 3A, the λ_{max} value shifts in the order of GONR3L > GONR12L > GONR6L, suggesting a high degree of conjugation in the GONR6L. Both the UV-Vis and Raman results imply that the oxidative unzipping process disrupts the crystalline MWCNT_L conjugation; however, the majority of π-conjugation can be maintained due to the vast size of the exfoliated GONR. In comparison, the λ_{max} of GONR synthesized from different MWCNT diameters shows a shift of GONR6L > GONR6M > GONR6S (Fig. 3B). This result is in agreement with the degree of oxidation revealed by FTIR and further elucidated the degree of disorder in the Raman spectra, indicating that the GONR produced from the MWCNT_M and MWCNT_S were unopened and stacked with low hydrophilicity. At this point, we have identified that the unzipping process for various diameter MWCNT for different suspension times in concentrated H_2SO_4 produced GONRs with different degrees of oxidation, disorder, and π-conjugation network. Moreover, GONRs with a disrupted π-conjugation network and oxygenated functional groups have a poor conductivity [11]. Nevertheless, the defects and functionalization of the graphene-based electrode has proven beneficial in electrochemical sensor applications [8]. The performance of GONR-based electrochemical sensors is demonstrated in the following sections.

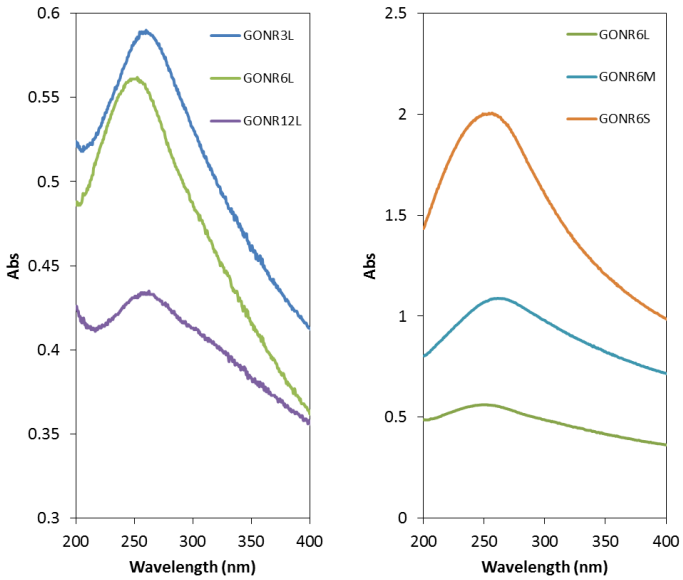

Figure 2.3: (A) UV-Vis absorption spectra of GONRs produced from MWCNT_L with varied suspension times in H_2SO_4. (B) UV-Vis of GONRs synthesized from varied diameters of MWCNTs with 6 h of H_2SO_4 treatment time.

2.3.5 Electrochemical performance and sensor applications

Several researchers have studied the relationship between surface structure and electrochemical phenomena, especially for carbon electrodes. In general, the electrode reactivity is influenced by the carbon material's microstructure [8], surface functional groups [32], and surface defects [33]. Herein, the produced GONRs were explored as the electrode materials in electrochemical sensors. First, a GONR-based electrode was tested in a ferro/ferricyanide redox probe to provide information on the electron transfer kinetics, based on the peak-to-peak redox potential (ΔE_p) between the reversible redox peaks, peak current density (I_p), and calculated active surface area (A). Then, the performance of the GONR-based electrodes towards the electro-oxidation of H_2O_2 and NADH were investigated using cyclic voltammetry (CV). H_2O_2 and NADH are essential mediators in enzymatic reactions, and therefore, the sensitive detection of these components is important for developing oxidase- and dehydrogenase-based electrochemical biosensors [34].

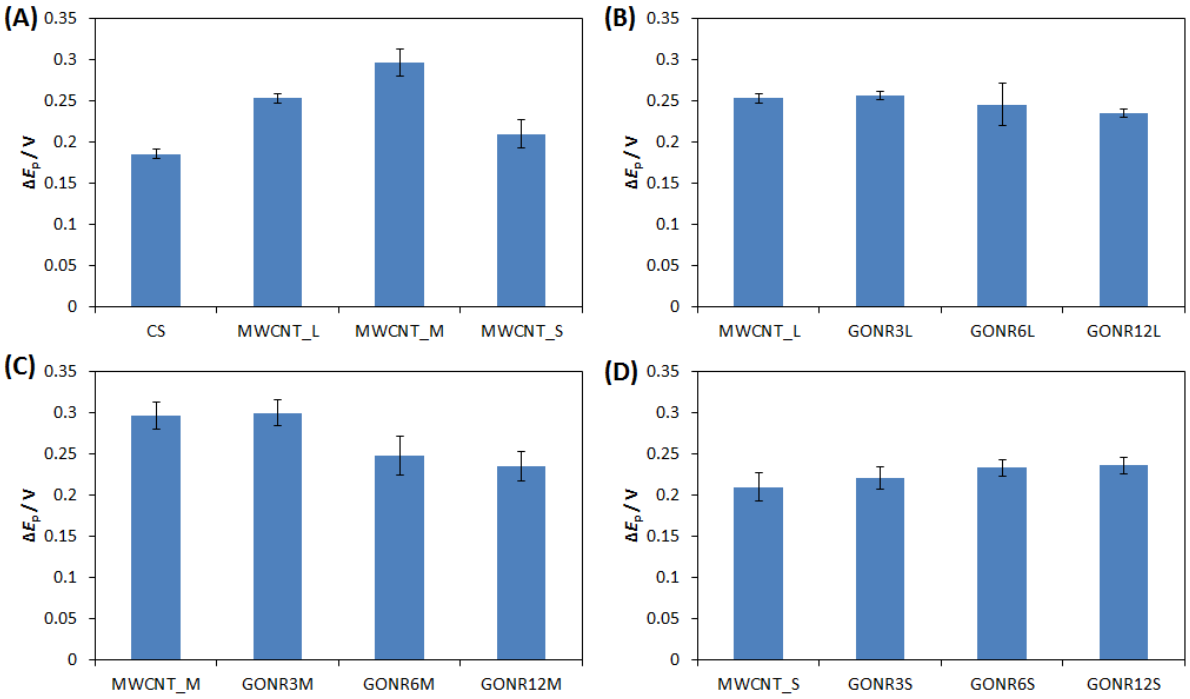

Figure 2.4: Extracted peak-to-peak redox separation (ΔE_p) of GONR- or MWCNT-modified CS. The electrolyte was 10 mM $K_3[Fe(CN)_6]$ in 1 M KCl and the scan rate was 100 mV/s.

Fig. 2.4 (A) shows that CS modified with pristine MWCNTs have increased ΔE_p values, indicating slow electron transfer kinetics. This is due to the hydrophobic characteristics of the MWCNTs, which hinder electrolyte diffusion. Furthermore, the ΔE_p values of the different MWCNT diameters varied as follows, MWCNT_M > MWCNT_L > MWCNT_S. The MWCNT_L had faster electron transfer kinetics than the MWCNT_M, likely due to the larger nanotubes providing a large surface area and easy electrolyte penetration for chemical reactions. Moreover, the MWCNT_L is less hydrophobic than MWCNT_M and MWCNT_S, as it produces a homogeneous layer on the CS electrode (Fig. 2.5). In contrast, the MWCNT_S has very fine tubes that reduce the CS electrode's surface roughness, making it easier for the electrolyte to make contact compared to the MWCNT_M.

Figure 2.5: Electrode surface of bare carbon sheet (CS) and various MWCNT diameter precursors modified CS.

Fig. 2.4 (B) displays decreasing of ΔE_p values proportional to increasing in acid treatment time for the GONRs yielded from the MWCNT_L, indicative of a fast electron transfer at a higher degree of oxidation. Therefore, the I_p and A values also increase, as depicted in Fig. 2.6 (B) and 2.7 (B), respectively. Since the $Fe(CN)_6^{3-/4-}$ is insensitive to surface oxide coverage [9, 32], the enhanced in conductivity and catalytic performance mainly resulted from the huge active surface area and surface defects on the exfoliated GONR, which are attractive as electrochemical reaction sites [31, 33-34]. The ΔE_p, I_p, and A values of the GONRs synthesized from the MWCNT_M were identical to those of the GONRs formed from the MWCNT_L. Their electron transfer kinetics increased significantly with longer acid treatment times, which may be due to the increased GONR hydrophilicity enhancing the electrolyte contact with the electrode's surface. However, GONRs produced from the MWCNT_S show increased ΔE_p values for longer suspension times in H_2SO_4 (Fig. 2.4 (D)). Nonetheless, no changes were observed on their I_p and A values, as presented in Fig. 2.6 (D) and 2.7 (D), respectively, which indicates slow electron transfer kinetics and poor electro-catalytic activity due to a low active surface area. This result agrees with the SEM images in Table 2.1 and the FTIR spectra in Fig. 2.1 (D) that reveal minimal unzipping and a low degree of oxidation for the MWCNT_S regardless of acid treatment times.

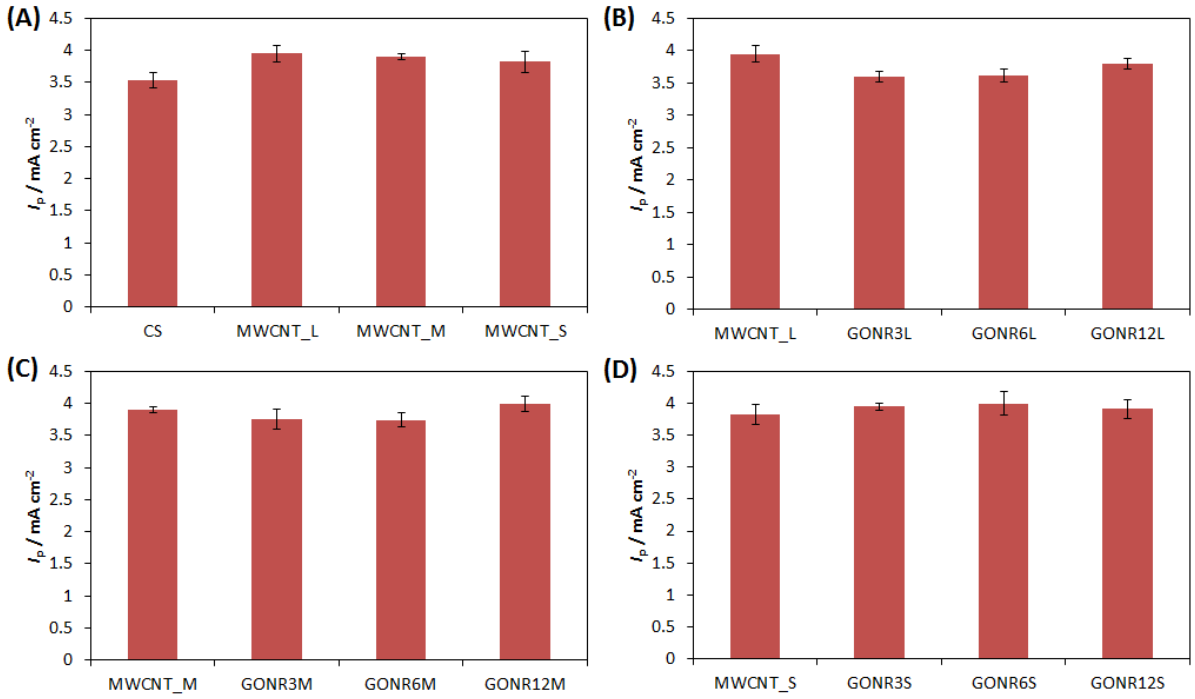

Figure 2.6: Extracted peak current density (I_p) of GONR- or MWCNT-modified CS. The electrolyte was 10 mM $K_3[Fe(CN)_6]$ in 1 M KCl and the scan rate was 100 mV/s.

The active surface area was calculated using Randle-Sevcik equation:

$$A = I_p/268600 \times n^{3/2} {D_0}^{1/2} C_0 v^{1/2}$$

where I_p, n, D_0, C_0 and v represent redox peak current (A), number of electrons transferred in the redox event, diffusion coefficient (cm^2 s^{-1}), concentration of redox species (mol cm^{-3}) and scan rate (V s^{-1}) [19]. The D_0 of 10 mM $K_3[Fe(CN)_6]$ in 1 M KCl for carbon sheet (CS) electrode is 7.33×10^{-5} cm^2 s^{-1}.

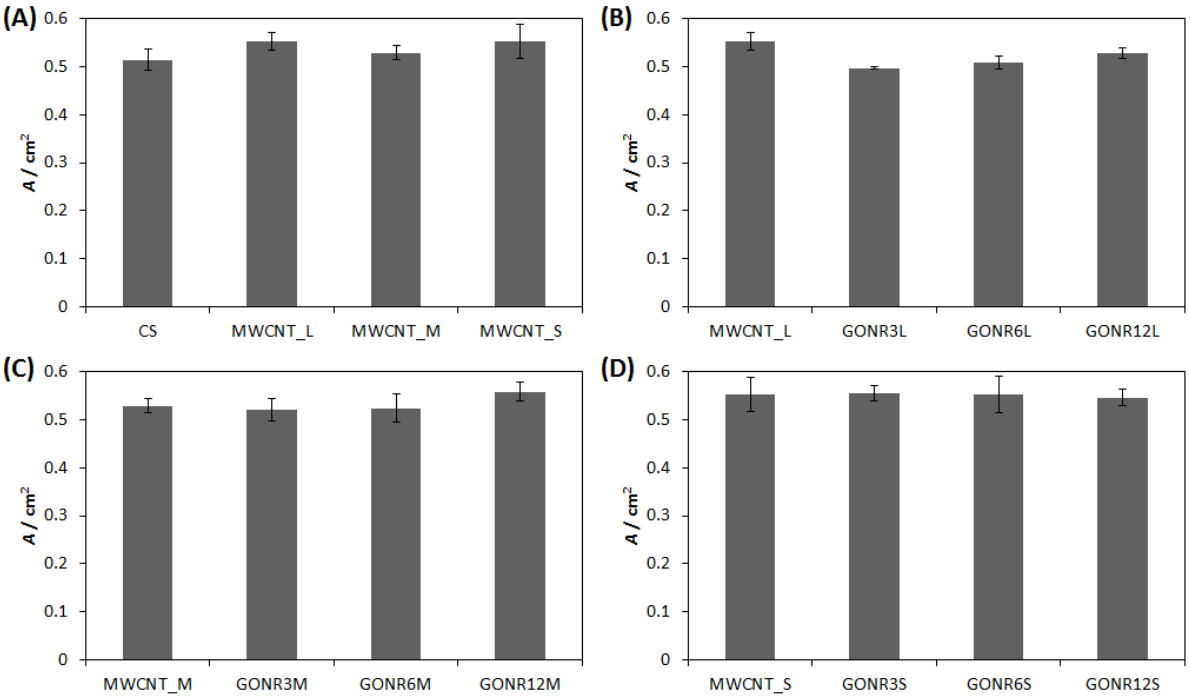

Figure 2.7: Calculated active surface area (*A*) of GONR- or MWCNT-modified CS. The electrolyte was 10 mM $K_3[Fe(CN)_6]$ in 1 M KCl and the scan rate was 100 mV/s.

Fig. 2.8 compares the background-subtracted CVs of the GONR-based electrodes in the presence of H_2O_2. The onset potentials for oxidation/reduction currents for the CS, GONR12S, GONR12M, and GONR12L began at 0.63/-0.18 V, 0.56/-0.11 V, 0.52/0.09 V, and 0.50/0.12 V, respectively (Fig. 2.8 (A)). This result shows that the bare CS had a poor catalytic activity, and modifying it with the GONR materials improved the electro-catalytic performance towards the H_2O_2 redox reactions. Moreover, the high degree of oxidation and edge-plane defects in the GONR12L may have contributed to its superior catalytic activity compared to the GONR12M and GONR12S. Fig. 2.8 (B) displays the onset potentials for oxidation/reduction currents for the MWCNT_L, GONR3L, GONR6L, and GONR12L, which began at 0.65/-0.15 V, 0.56/0.07 V, 0.53/0.10 V, and 0.50/0.12 V, respectively. The pristine MWCNT_L-modified CS electrode exhibited a low electro-catalytic activity compared to the GONR-based electrode, indicating that the oxygen-based functional groups

and edge-plane defect sites are required to catalyze the H_2O_2 redox reaction [8, 34]. In addition, this result also confirmed that the GONRs produced from longer acid treatment times demonstrated a higher degree of oxidation, producing a more active catalytic material for H_2O_2 detection.

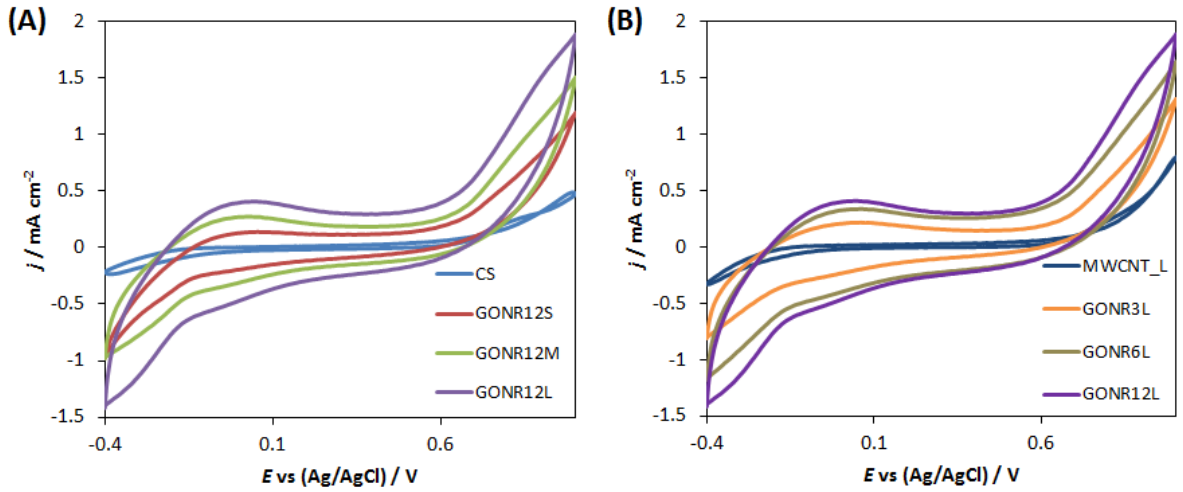

Figure 2.8: (A) CVs of GONR-based electrodes from various MWCNT diameters precursors after 12 h of H_2SO_4 treatment time. (B) CVs of GONR-based electrodes produced from the MWCNT_L precursor after various suspension periods in H_2SO_4. The electrolyte is 1 mM H_2O_2 in 0.1 M PBS (pH 7.0) with a scan rate of 50 mV/s.

Fig. 2.9 (A) shows that the oxidation of NADH occurs at 0.38 V for a CS. Modifying the CS with a GONR material maintained this oxidation peak potential, but resulted in an increased peak current density. The CVs show that the GONR12L has the highest peak current density, indicating enhanced catalytic activity due to the exfoliated GONRs providing a high surface reactivity and edge-plane defect density [34]. This phenomenon may also be due to an increased effective surface area, manifested by an increase in the background charging current [35] and verified by the calculation in Fig. 2.7. Furthermore, Fig. 2.9 (B) suggests that the pristine MWCNTs have a lower electro-catalytic activity than the GONR materials, indicating that the oxygen functional groups catalyzed the NADH oxidation

reaction [35]. Consequently, the GONR synthesized at longer suspension times in H_2SO_4 gave a higher electro-catalytic performance due to a high degree of oxidation and larger active surface area.

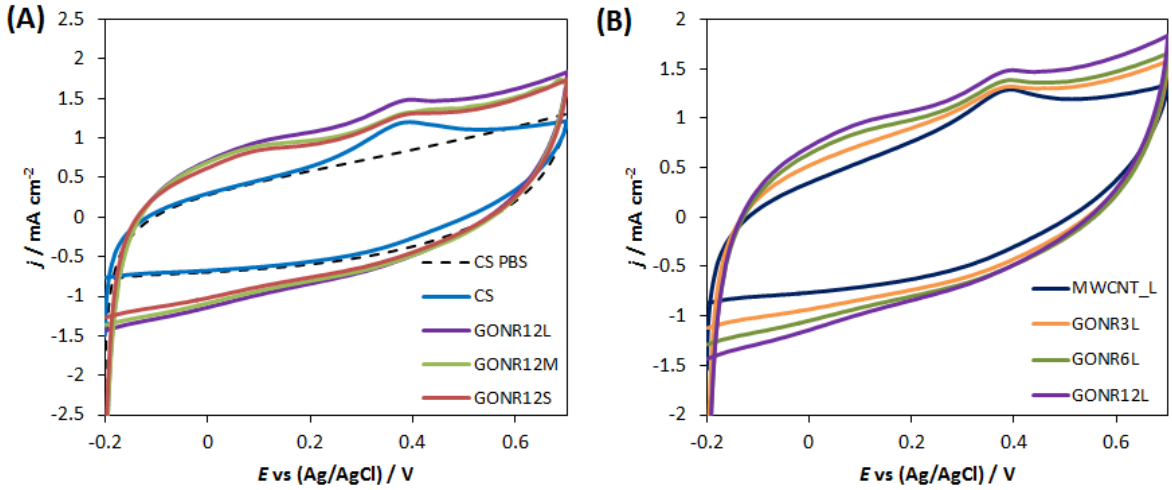

Figure 2.9: (A) CVs of GONR-based electrodes from various MWCNT diameters precursors after 12 h of H_2SO_4 treatment time. (B) CVs of GONR-based electrodes produced from the MWCNT_L precursor after various suspension periods in H_2SO_4. The electrolyte is 1 mM NADH in 0.1 M PBS (pH 7.0) with a scan rate of 50 mV/s.

In conclusion, the electrochemical performance of the GONR-based electrode is significantly affected by its surface morphology and degree of oxidation, which vary through the oxidative unzipping process of various MWCNT diameters in different acid treatment times. A large proportion of oxygenated species present on the GONR can be beneficially when used in electrochemical sensors where oxygenated electro-catalytic reactions are employed. Based on these results, a higher performance of the electrodes is observed with the modification of the GONRs, following the precursors of MWCNT_L > MWCNT_M > MWCNT_S at 12 > 6 > 3 h of acid treatment times.

2.4 Conclusions

In summary, we have studied for the first time, the effects of MWCNT diameter and H_2SO_4 pre-treatment time towards GONR production by the oxidative unzipping method. SEM images reveal that large-diameter MWCNTs have a faster rate of unzipping than smaller MWCNT diameters. Moreover, only the medium-diameter MWCNTs depend on the acid treatment period to produce fully unzipped nanoribbons. FTIR spectra disclose the degree of oxidation, which have increasing peak intensities correlated to increase acid treatment times and MWCNT diameters. This indicates that the large-diameter MWCNTs have highly reactive surfaces that easily interact with oxygen atoms, subsequently cracking the graphitic lattice. Thus, the degree of oxidation is correlated with the I_D/I_G ratio in Raman spectra, showing 176%, 27%, and 19% increments in their degree of disorder for the GONR products compared to MWCNT_L, MWCNT_M, and MWCNT_S, respectively, while a low I_D/I_G ratio variation was observed for the different acid treatment times. Interestingly, the maximum absorbance peak, λ_{max}, shows that the highly oxidized GONR synthesized from the MWCNT_L maintained a large amount of its π-conjugated structure. Applying the GONRs as electrode materials in electrochemical sensors demonstrated that they exhibited superior electro-catalytic activity compared to their MWCNT precursors owing to the highly active surface areas with oxygen-based functional groups that facilitate catalyzing redox reactions. These enhance sensor performance, which in turn has been shown as being dependent on the size of the original MWCNTs and treatment time in concentrated H_2SO_4. Further work on improving the GONR's electro-catalytic activity by functionalization has commenced in our laboratory, paving the way for future development of GONR-based electrochemical biosensors.

2.5 References

[1] A.K. Geim, K.S. Novoselov, The rise of graphene. *Nat Mater* **6** (2007) 183.

[2] S. Park, R.S. Ruoff, Chemical methods for the production of graphenes. *Nat Nanotechnol* **4** (2009) 217.

[3] M.J. Allen, V.C. Tung, R.B. Kaner, Honeycomb Carbon: A review of graphene. *Chem. Rev.* **110** (2010) 132.

[4] K.S. Novoselov, A.K. Geim, S.V. Morozov, D. Jiang, Y. Zhang, S.V. Dubonos, I.V. Grigorieva, A.A. Firsov, Electric field effect in atomically thin carbon films. *Science* **306** (2004) 666.

[5] C.N.R. Rao, A.K. Sood, R. Voggu, K.S. Subrahmanyam, Some novel attributes of graphene. *J. Phys. Chem. Lett.* **1** (2010) 572.

[6] T. Kuila, S. Bose, A.K. Mishra, P. Khanra, N.H. Kim, J.H. Lee, Chemical functionalization of graphene and its applications. *Prog. Mater. Sci.* **57** (2012) 1061.

[7] D. Chen, H. Feng, J. Li, Graphene oxide: preparation, functionalization and electrochemical applications. *Chem. Rev.* **112** (2012) 6027.

[8] D.A.C. Brownson, C.E. Banks. Graphene electrochemistry: fabricating amperometric biosensor. *Analyst* **136** (2011) 2084.

[9] D.A.C Brownson, A.C. Lacombe, M. Gómez-Mingot, C.E. Banks. Graphene oxide gives rise to unique and intriguing voltammetry. *RCS Advances* **2** (2012) 665.

[10] M. Terrones, Nanotubes unzipped. *Nature* **458** (2009) 845.

[11] D.V. Kosynkin, A.L. Higginbotham, A. Sinitskii, J.R. Lomeda, A. Dimiev, B.K. Price, J.M. Tour, Longitudinal unzipping of carbon nanotubes to form graphene nanoribbons. *Nature* **458** (2009) 872.

[12] L. Jiao, X. Wang, G. Diankov, H. Wang, H. Dai, Facile synthesis of high-quality graphene nanoribbons. *Nat Nanotechnol* **5** (2010) 321.

[13] A.G. Cano-Márquez, F.J. Rodríguez-Macías, J. Campos-Delgado, C.G. Espinosa-González, F. Tristán-López, D. Ramírez-González, D.A. Cullen, D.J. Smith, M. Terrones, Y.I. Vega-Cantù, Ex-MWNTs: Graphene sheets and ribbons produced by lithium intercalation and exfoliation of carbon nanotubes. *Nano Lett* **9** (2009) 1527.

[14] Ci L, Zu X, Wang L, Gao W, Ding F, Kelly KF, et al. Controlled nanocutting of graphene. *Nano Res* **1** (2008) 116.

[15] A.M. Dimiev, L.B. Alemany, J.M. Tour, Graphene oxide. Origin of acidity, its instability in water and new dynamic structural model. *ACS Nano* **7** (2013) 576.

[16] A.L. Higginbotham, D.V. Kosynkin, A. Sinitskii, Z. Sun, J.M. Tour, Lower-defect graphene oxide nanoribbons from multiwalled carbon nanotubes. *ACS Nano* **4** (2010) 2059.

[17] A.M. Dimiev, J.M. Tour, Mechanism of graphene oxide formation. *ACS Nano* **8** (2014) 3060.

[18] S. Iijima, Helical microtubules of graphitic carbon. *Nature* **354** (1991) 56.

[19] C.H. Kiang, M. Endo, P.M. Ajayan, G. Dresselhaus, M.S. Dresselhaus, Size effect in carbon nanotubes. *Phys. Rev. Lett.* **81** (1998) 1869.

[20] X. Sun, C.H. Kiang, M. Endo, K. Takeuchi, T. Furuta, M.S. Dresselhaus, Stacking characteristics of graphene shells in carbon nanotubes. *Phys. Rev. B* **54** (1996) 629.

[21] X.Q. He, S. Kitipornchai, C.M. Wang, K.M. Liew, Modeling of van der Waals force for infinitesimal deformation of multi-walled carbon nanotubes treated as cylindrical shells. *Int. J. Solid Struct.* **42** (2005) 6032.

[22] S.R. Dhakate, N. Chauhan, S. Sharma, R.B. Mathur, The production of multi-layer graphene nanoribbons from thermally reduced unzipped multi-walled carbon nanotubes. *Carbon* **49** (2011) 4170.

[23] P.M. Ajayan, B.I. Yakobson, Oxygen breaks into carbon world. *Nature* **441** (2006) 818.

[24] J.L. Li, K.N. Kudin, M.J. McAllister, R.K. Prud'homme, I.A. Aksay, R. Car, Oxygen-

driven unzipping of graphitic materials. *Phys. Rev. Lett.* **96** (2006) 176101-1.

[25] K.C. Park, T. Hayashi, H. Tomiyasu, M. Endo, M.S. Dresselhaus, Progressive and invasive functionalization of carbon nanotube sidewalls by diluted nitric acid under supercritical conditions. *J. Mater. Chem.* **15** (2005) 407.

[26] L.Q. Hoa, M.C. Vestergaard, H. Yoshikawa, M. Saito, E. Tamiya, Enhancing catalytic performance of Pt-based electrode with a noncovalent interaction-induced functionalized carbon nanotube-grafted matrix. *J. Mater. Chem.* **22** (2012) 14705.

[27] C. Hontoria-Lucas, A.J. López-Peinado, J.D. López-González, M.L. Rojas-Cervantes, R.M. Martín-Aranda, Study of oxygen-containing groups in a series of graphite oxides: physical and chemical characterization. *Carbon* **33** (1995) 1585.

[28] G. Shao, Y. Lu, F. Wu, C. Yang, F. Zeng, Q. Wu, Graphene oxide: the mechanism of oxidation and exfoliation. *J. Mater. Sci.* **47** (2012) 4400.

[29] W.S. Hummers, R.E. Offeman, Preparation of graphitic oxide. *J. Am. Chem. Soc.* **80** (1958) 1339.

[30] S. Cho, K. Kikuchi, A. Kawasaki, Radial followed by longitudinal unzipping of multiwalled carbon nanotubes. *Carbon* **49** (2011) 3865.

[31] A. Ambrosi, A. Bonanni, Z. Sofer, J.S. Cross, M. Pumera, Electrochemistry at chemically modified graphenes. *Chem. Eur. J.* **17** (2011) 10763.

[32] P. Chen, M.A. Fryling, R.L. McCreery, Control of electron transfer kinetics at glassy carbon electrodes by specific surface modification. *Anal. Chem.* **68** (1998) 3958.

[33] M.T. McDermott, K. Kneten, R.L. McCreery, Anthraquinonedisulfonate adsorption, electron-transfer kinetics, and capacitance on ordered graphite electrodes: the important role of surface defects. *J. Phys. Chem.* **96** (1992) 3124.

[34] M. Zhou, Y. Zhai, S. Dong, Electrochemical sensing and biosensing platform based on chemically reduced graphene oxide. *Anal. Chem.* **81** (2009) 5603.

[35] D.C.S. Tse, T. Kuwana, Electrocatalysis of dihydronicotinamide adenosine diphosphate with quinones and modified quinone electrodes. *Anal. Chem.* **50** (1978) 1315.

CHAPTER 3

DEVELOPMENT OF NON-ENZYMATIC ELECTROCHEMICAL GLUCOSE SENSOR BASED ON GRAPHENE OXIDE NANORIBBONS - GOLD NANOPARTICLE HYBRID

3.1 Introduction

The number of people living and dying with diabetes mellitus across the world is alarming, and is continuing to rise [1]. Currently, much effort is dedicated to the development of an artificial pancreas that monitors the glucose concentration continuously in diabetic patients [2]. At present, conventional glucose sensors on the market are based on the enzymatically catalyzed oxidation of glucose. However, these types of glucose sensor suffer from several drawbacks such as degradation of enzymatic activity (owing to factors such as temperature, pH, humidity, etc.), their oxygen dependence and a lack of electrode simplicity and reproducibility [3-4]. Therefore, advances in the direct electrochemical oxidation of glucose with high sensitivity and selectivity are greatly desired.

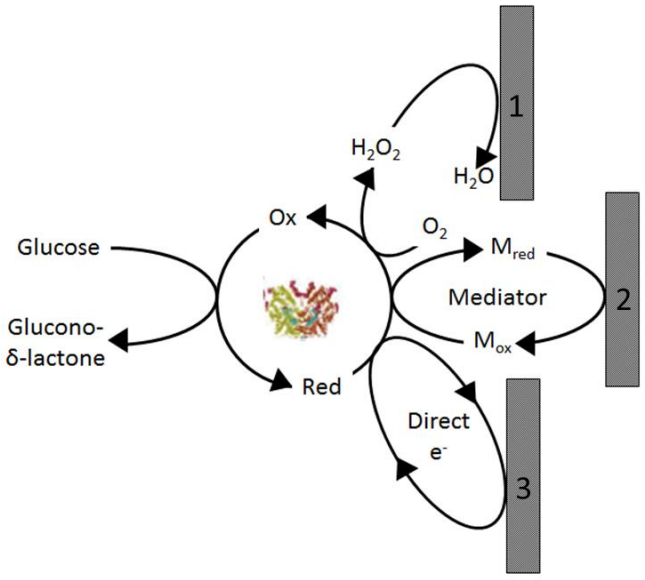

Figure 3.1: Generation of enzymatic glucose sensor.

For improvements in the sensitivity of the sensor, electrode surface modification is an effective method for enhancing the catalytic activity of noble metals or transition metals, which act as electrochemical catalysts for the glucose oxidation reaction. Among such metals, gold (Au) and platinum (Pt) are the most common and effective [4]. Vassilyev et al. [5] reported that the glucose electro-oxidation reaction rate on gold exceeds that on platinum and other metals in group VIII in neutral and alkaline conditions, which makes it a better candidate for glucose sensor applications. Studies of the glucose oxidation mechanism on gold electrodes showed that the gold surface can induce a hydroxyl adsorption (OH_{ads}) layer, leading to the dehydrogenation step in the glucose oxidation reaction mechanism [5-8]. In agreement with theoretical studies, experimental data also proved that the rate of the dehydrogenation step is lower at neutral and low pH than at high pH. Unfortunately, in the case of implantable glucose sensors, a neutral pH with a minimum of added specific solvents is preferable for practical applications. To solve this problem, we focused on the development of an active functional supporting matrix that could promote the dehydrogenation process and enhance the glucose oxidation reaction kinetics under neutral conditions. Recently, Hoa et al. [9] demonstrated concrete research on functionalized multi-walled carbon nanotubes (MWCNTs) as a functional supporting matrix, which enhanced the catalytic activity of Pt nanoparticles by inducing OH_{ads} to promote a similar dehydrogenation step in the ethanol oxidation reaction. Taking into account the successful application of functionalized MWCNTs as a functional supporting matrix, herein, we utilize functionalized carbon nanomaterial to enhance the performance of a low-loaded noble-metal-based catalyst.

Carbon nanomaterials have been at the forefront of nanomaterial research for decades with the discovery of fullerenes, carbon nanotubes (CNTs), and more recently, graphene. Graphene is a single-atomic-layer honeycomb lattice of carbon atoms in an sp^2 hexagonal bonding configuration which is the basic building block for other carbon materials [10]. The

properties of graphene, however, are influenced by the mechanical or chemical synthesis procedure [11]. Compared with mechanical synthesis, the chemically derived approach is scalable, allows high-volume production, and is versatile in terms of chemical functionalization, but gives low control of the graphene structures and defects [12]. One of the improved techniques in chemically derived graphene is the longitudinal unzipping of CNTs to form graphene oxide nanoribbons (GONRs) by using oxidizing agents in strong acidic conditions, followed by a reduction process to finally achieved graphene nanoribbons [13]. Graphene nanoribbons are strips of graphene with a high length-to-width ratio and straight edges. The advantage of this method is the better controllability of the graphene layer number according to the selected MWCNT size and the uniform structure of the nanoribbons. Owing to the strong oxidative reaction during unzipping process, the resulting GONRs are highly soluble in water and polar solvents, with an attractive surface and edges containing oxygen functional groups [14].

Herein, for the first time, we investigate the performance of gold nanoparticles decorated on graphene oxide nanoribbons on a carbon sheet substrate (AuNP/GONR/CS) towards the direct glucose oxidation reaction in neutral conditions. Previously, researchers have synthesized graphene or graphene oxide decorated with AuNPs by electrodeposition [15] and *in-situ* chemical synthesis [16]. The disadvantages of those methods are the uncontrollable amount and size of AuNPs on the graphene–modified electrode, leading to poor reproducibility. In contrast to these conventional approaches, we develop a chemical and thermal deposition method that offers high controllability, reproducibility, and consequently, reactivity of the AuNP/GONR catalyst towards the glucose oxidation reaction. Furthermore, the performance of the electrode under the influence of electroactive interference is studied. These interesting results obtained may provide insights for further improvements of non-

enzymatic glucose sensors through the utilization of GONRs as a functional supporting matrix.

3.2 Experimental

3.2.1 Materials and reagents

Carbon sheet (CS), gold sheet (1.153 g, 25 × 25 mm), potassium chloride (KCl), 1,2,3,4–tetrahydronaphthalene (tetraline, 95–98%), *tert*-butylamine-borane complex (TBAB) and polypyrrole (PPy, 5 wt % solution in water) were purchased from Sigma Aldrich, USA. Multi-walled carbon nanotubes (MWCNTs), hydrogen tetrachloroaurate (III) tetrahydrate ($HAuCl_4 \cdot 4H_2O$), oleylamine, hexane, concentrated sulphuric acid (H_2SO_4), potassium permanganate ($KMnO_4$), 30% hydrogen peroxide (H_2O_2), ethanol, ether, D-glucose, and 5% Nafion® were obtained from Wako Co., Japan. Phosphate buffer solution (PBS, 0.1 mol L^{-1}, pH 7.0) was prepared from KH_2PO_4 and K_2HPO_4. Ultrapure water was obtained from a Barnstead Nanopure water purification system (18 MΩ, Thermo Scientific, USA) and was used in all experiments.

3.2.2 Synthesis of GONRs

GONRs were synthesized through the method of longitudinal unzipping of MWCNTs [13]. In brief, MWCNTs were suspended in concentrated H_2SO_4 for 12 h, and then treated with $KMnO_4$. The mixture was stirred at room temperature for 1 h, and heated at 55 to 70 °C for a further 1 h. After all the $KMnO_4$ had been consumed, the reaction was quenched by pouring the mixture onto ice containing 1.25% H_2O_2. The solution was filtered through a polytetrafluoroethylene (PTFE) membrane. The remaining solid was washed with HCl and ethanol/ether alternately between filtrations. The final product was dried *in vacuo*.

3.2.3 Synthesis of AuNPs

AuNPs were synthesized through a burst nucleation method using the TBAB complex as the reducing agent [17]. First, $HAuCl_4 \cdot 4H_2O$ (10 mg), oleylamine (1 mL), and tetraline (1 mL) were mixed to obtain the precursor solution. Then, the solution was stirred at room temperature for 10 min. The reducing solution was prepared by mixing oleylamine (100 µL), tetraline (100 µL), and TBAB (0.1 mmol), and was added slowly to the precursor solution. The reaction mixture was stirred at room temperature for 1 h.

Ethanol (10 mL) was added to the reacted solution so that the AuNPs precipitated, and cleaned AuNPs were thus obtained. The AuNPs were collected by centrifugation at 8000 rpm for 8 min. The supernatant was removed, and hexane (2 mL) followed by ethanol (10 mL) was added to disperse the AuNPs for further centrifugation. Dispersion and centrifugation were carried out until the supernatant turned colorless. Finally, AuNP solution was prepared by adding hexane to prevent aggregation. The final concentration was 15 mg $HAuCl_4$ in 1 mL hexane.

3.2.4 Fabrication of AuNPs/GONRs/CS electrode

First, GONRs (0.5 mg) were sonicated and dispersed in 1 mL ethanol. Then, the mixture was cast on the surface of a cleaned carbon sheet (2 cm^2) and dried at 60 °C for 1 h. A 25% AuNP solution (100 µL) was then dropped slowly onto the surface of the GONR-modified carbon sheet to obtain the AuNP/GONR/CS working electrode. To remove the stabilizing agent on the AuNP surface and bind the AuNPs to the GONRs, the AuNP/GONR/CS was subjected to thermal treatment at 400 °C for 2 h.

3.2.5 Characterization of GONR materials and AuNPs/GONRs/CS electrodes

The functional groups on the MWCNTs and GONRs were confirmed by attenuated total reflectance–Fourier transform infrared (ATR-FTIR) spectroscopy (Horiba FT-720, Japan). Raman-11 spectroscopy (Nanophoton Corp., Japan) was used to examine the defect intensities of the MWCNTs and GONRs. The morphologies of the catalytic materials were acquired by scanning electron microscopy (SEM) using a DB 235 microscope (FEI Co.). All electrochemical measurements were performed with an Autolab potentiostat/galvanostat PGSTAT12 (EcoChemie, Netherlands). A three-electrode cell was used for the electrochemical measurements, with a platinum coil serving as the counter electrode, Ag/AgCl as the reference electrode (BASi, 3.0 mol dm^{-3} NaCl, +0.209 V vs. NHE at 298.2 K), and the prepared AuNP/GONR/CS as the working electrode.

3.3 Results and Discussion

3.3.1 Preparation and morphological characterization of AuNP/GONR/CS

Figs. 3.2 (A) and (B) illustrate the preparation process and surface morphologies of the catalytic materials corresponding to each fabrication step. The successful opening of MWCNTs was based on the oxidation of alkenes by permanganate under strong acid conditions [13]; appeared to occur along a line, thus affording straight-edged nanoribbons, as shown in Fig. 3.2 (B)(ii). Then, AuNPs (≈6 nm) were hybridized homogenously on the surface of the GONR-modified carbon sheet (Fig. 3.2 (B)(iii)). As depicted in Fig. 1B (iv), under thermal treatment at 400 °C for 2 h, small AuNPs aggregated to form larger nanoparticles [17]. Aggregations of AuNPs were profound at the edges of the GONRs owing to the large number of oxygen-containing functional groups that attract AuNPs.

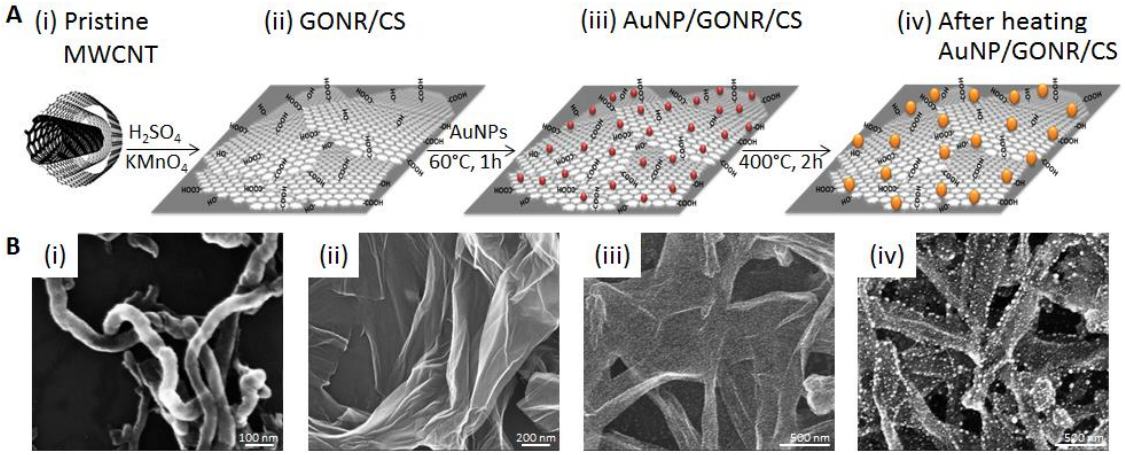

Figure 3.2: (A) Illustration of AuNP/GONR/CS electrode preparation process, and (B) SEM images of the corresponding catalytic materials at each fabrication step.

The thermal treatment step was necessary not only to activate the AuNP catalytic surface by removing the stabilizing agents, but also to bind AuNPs on the GONRs for stability enhancement [18]. On the basis of cyclic voltammetry (CV) data of the AuNP/GONR/CS electrode with and without thermal treatment in 10 mM ferricyanide solution (Fig. 3.3), it was proved that the AuNP/GONR/CS electrode subjected to the thermal treatment had an active surface area 28.76% larger [19], and showed a corresponding increase in the glucose electro-oxidation peak current density (Fig. 3.4). The active surface area (A) was calculated based on Randle-Sevcik equation:

$$A = I_p/268600 \times n^{3/2} {D_0}^{1/2} C_0 v^{1/2}$$

where I_p, n, D_0, C_0 and v represent redox peak current (A), number of electrons transferred in the redox event, diffusion coefficient ($cm^2\ s^{-1}$), concentration of redox species ($mol\ cm^{-3}$) and scan rate ($V\ s^{-1}$) [19]. The D_0 of 10 mM $K_3[Fe(CN)_6]$ in 0.1 M PBS for modified carbon sheet (CS) electrode is $3.52 \times 10^{-5}\ cm^2\ s^{-1}$.

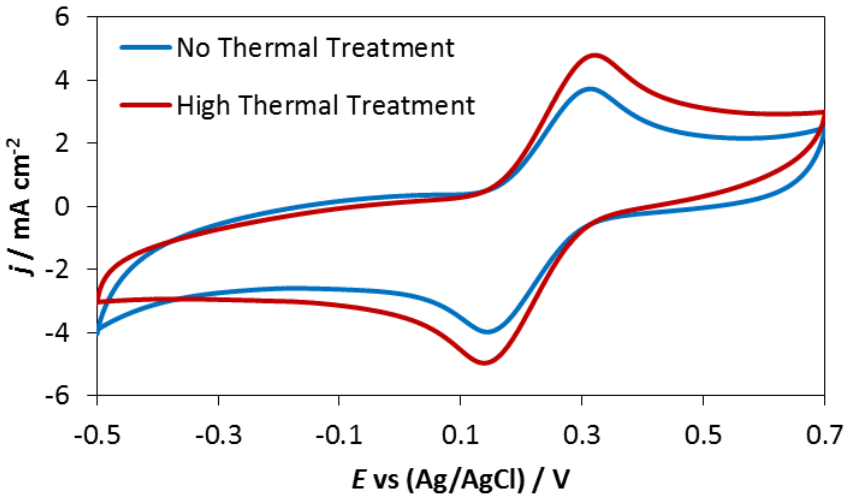

Figure 3.3: Effect of thermal treatment on the AuNP/GONR/CS electrode in enhancing active surface area. The electrolyte was 10 mM $K_3[Fe(CN)_6]$ in 0.1 M PBS (pH 7.0), and the scan rate was 50 mV/s.

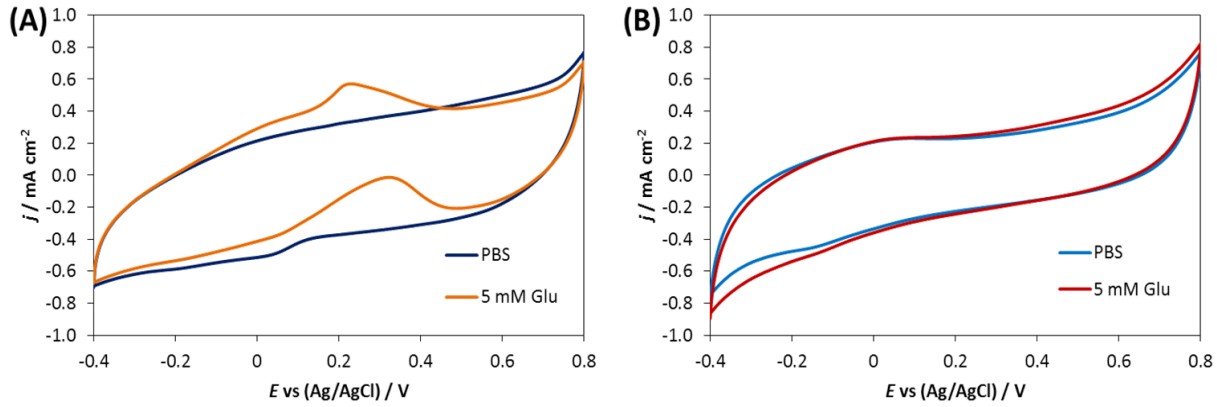

Figure 3.4: Electrocatalytic comparison of the AuNP/GONR/CS electrode with (A) and without (B) the thermal treatment. The electrolyte was 0.1 M PBS (pH 7.0) with and without the presence of 5 mM glucose and the scan rate was 10 mV/s.

3.3.2 Characterization of GONRs

To examine the nature of the functional groups on GONRs resulting from the unzipping of MWCNTs, we prepared a thin layer of catalyst on an ATR diamond surface with a few drops of 0.5 mg/mL GONR or native MWCNT solution in ethanol. The FTIR spectra in Fig. 3.5

(A) show common peaks at around 2300 cm^{-1}, which are attributed to the asymmetric stretching vibration of CO_2, while the noise signal in the regions 3400–4000 cm^{-1} and 1300–1900 cm^{-1} are derived from water vapor [9]. Apart from those signals, the GONR spectrum showed a strong hydroxyl band at approximately 3200 cm^{-1} (i) of COO–H/O–H stretching, in addition to three carbonyl bands at around 1700 cm^{-1} (ii) of C=O stretching, around 1564 cm^{-1} (iii) of –COO– asymmetric stretching, and about 1209 cm^{-1} (iv) of C–O stretching [9, 13]. In comparison, the MWCNT spectrum displayed no hydroxyl (i) or carbonyl (ii–iv) bands, indicating that the MWCNTs had undergone oxidation unzipping to form functional GONR materials.

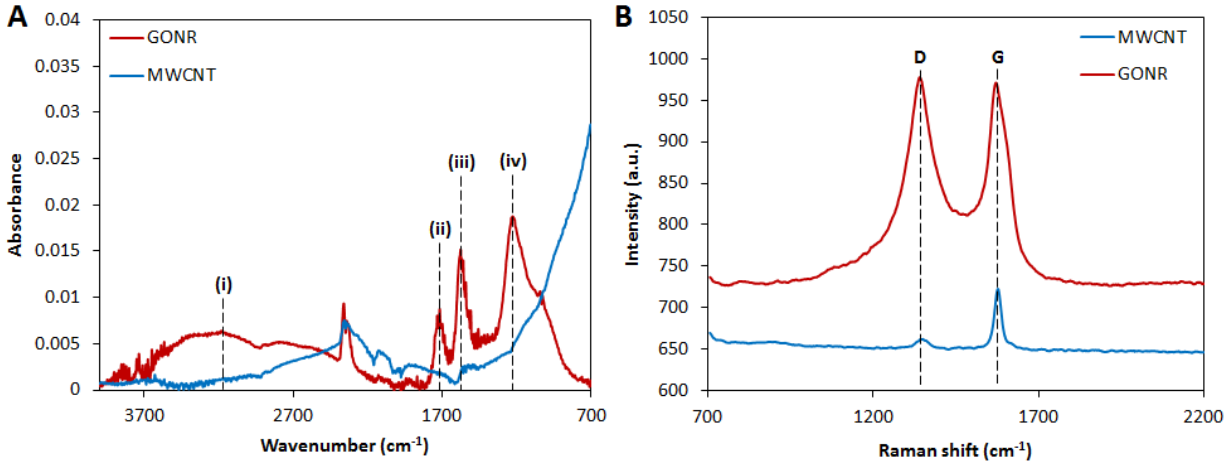

Figure 3.5: (A) ATR-FTIR and (B) Raman spectra of GONRs compared with those of pristine MWCNTs as the starting material.

Raman spectroscopy provides useful information on the defects (D band) and in-plane vibrations of sp^2 carbon atoms (G band) of graphene [20]. The GONR and MWCNT solutions in ethanol were casted on quartz microglass and dried at room temperature. The samples were measured using an excitation wavelength of 514 nm. Fig. 3.5 (B) displays a broadened G band (1565 cm^{-1}) after the oxidation process, along with the appearance of the D band at 1331 cm^{-1} of GONRs [20-21]. This result reveals the size reduction of in-plane sp^2

domains to sp^3, indicating an increase in the structural disorder level of the GONRs owing to the oxidative synthesis process. The disorder degree can be calculated from the ratio of intensities of the D and G peaks (I_D/I_G) [13, 20]. The I_D/I_G ratios of pristine MWCNTs and GONRs were 0.054 and 1.026, respectively, which further confirmed that the GONRs resulted from a strong oxidative unzipping process, and therefore, contained many oxygen functional groups on the basal plane. It is expected that these functional groups on the GONR matrix play an important role in the enhancement of the glucose oxidation kinetics on AuNPs. Further electrocatalytic characterizations of each catalytic material towards the direct glucose oxidation reaction under neutral conditions are presented in the following sections.

3.3.3 Glucose oxidation reaction in neutral conditions

The glucose oxidation reaction kinetics is dependent on the chemical and physical nature of the catalytic materials [5, 7] on the electrode surface. Gold has proven to be a superior catalyst in the glucose oxidation reaction in either alkaline or neutral conditions [5]. However, studies have proved that the smooth surface of gold at temperatures below 473 K is catalytically inactive for the hydrogenation and oxidation reactions [22]. Interestingly, the catalytic properties of gold were improved in nanosized particles on a supporting metal oxide even at temperatures as low as 200 K owing to the moderate strength of the metal–oxygen bonding [23-24]. Taking this into account, it is expected that the oxygen functional groups present near the AuNP active surface can induce OH_{ads} via non-covalent interactions, and consequently, can stimulate a faster dehydrogenation rate as the first and slow step in the glucose oxidation mechanism, and therefore, speed up the kinetics of the whole reaction [9]. Hence, we prepared a series of catalytic materials made of AuNPs decorated on our promising GONR functional supporting matrix on a CS substrate to study their catalytic

performance on the glucose oxidation reaction in neutral conditions in comparison to that of a bulk gold electrode.

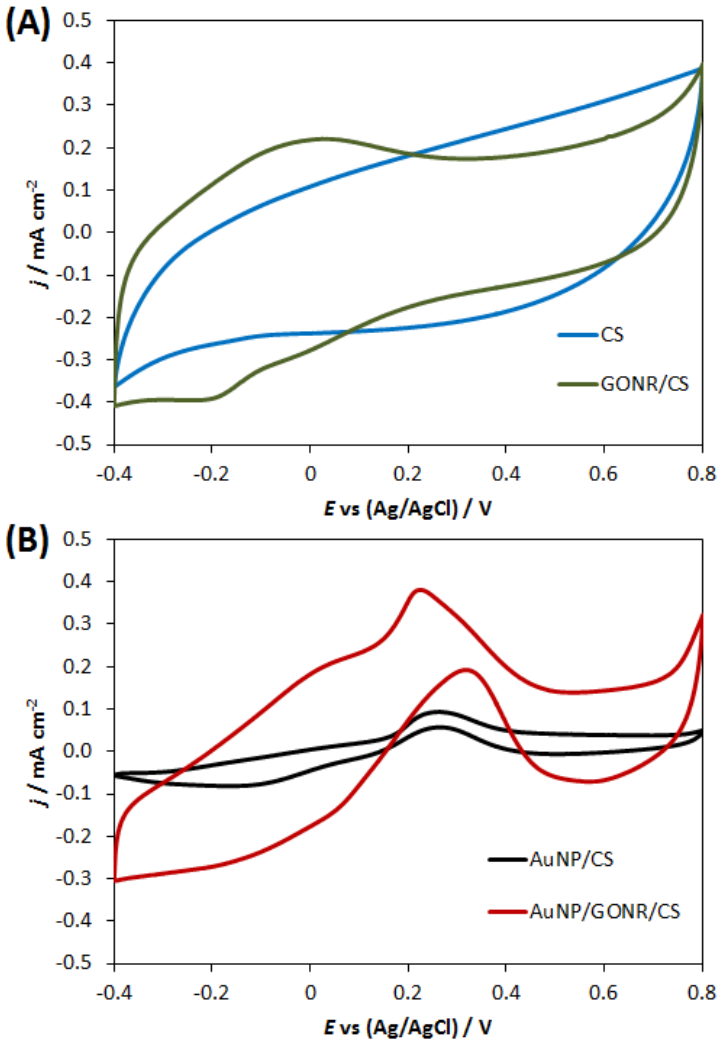

Figure 3.6: Electrochemical characterization of glucose oxidation reaction (GOR) on (A) CS and GONR/CS, and (B) AuNP/CS and AuNP/GONR/CS electrodes. The electrolyte was 5 mM glucose in 0.1 M PBS (pH 7.0), and the scan rate was 10 mV/s.

As depicted by the CVs in Fig. 3.6 (A), bare CS was inert to glucose oxidation. The GONR/CS electrode was also inert to glucose oxidation, but exhibited a high double layer capacitance in both phosphate buffer solutions (PBS) with and without the presence of glucose. The broad peak around 0 V might be due to the oxidation of oxygen functional groups on the GONR surface. For the investigation of the role of the GONRs in enhancing

the catalytic activity of AuNPs, CVs of the AuNP/CS and AuNP/GONR/CS electrodes with equal geometric areas and AuNP loadings were compared (Fig. 3.6 (B)). The glucose oxidation potential of the AuNP/CS electrode can be observed at 0.257 V, while a negative shift of 30 mV was observed in the case of the AuNP/GONR/CS electrode, clearly indicating the supporting effects of the GONR functional matrix on the enhancement of the reaction kinetics. In addition, AuNPs with support from GONRs induced a much earlier onset potential at –0.185 V than that of the AuNP/CS electrode. This enhancement indicates the increase in adsorption kinetics of glucose on the active surface of the AuNPs decorated on the functional GONR matrix [23]. Consequently, not only was the oxidation peak potential of the AuNP/GONR/CS electrode shifted negatively, but its current density was also 121.22% higher than that of the AuNP/CS electrode. Furthermore, the earlier onset potential suggests that the oxygen-containing functional groups on the GONR matrix might help facilitate the formation of the OH adsorption (OH_{ads}) layer on the Au surface, which is necessary for the dehydrogenation step that initiates the glucose oxidation mechanism [5-8]. In addition, the SEM image of the AuNPs taken after thermal treatment without the GONR matrix demonstrates the strong aggregation of AuNPs to form a Au island (Fig. 3.7). This result again proves that GONRs were essential in acting as a backbone to prevent the aggregation of AuNPs, and thus to enhance the total active surface area of AuNPs.

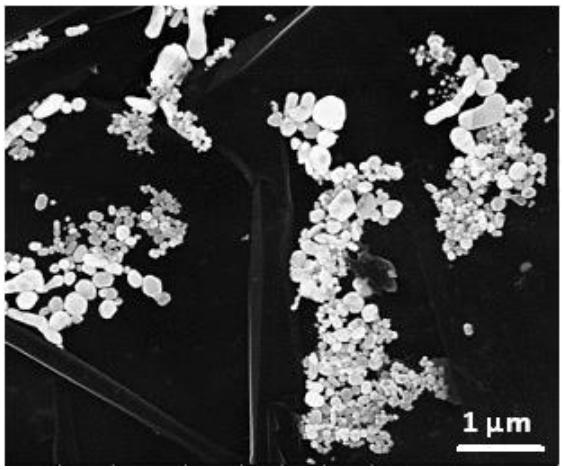

Figure 3.7: SEM image of the AuNP on carbon sheet electrode after thermal treatment.

For further investigation of the catalytic properties of AuNPs supported by the GONR functional matrix, the CV of the AuNP/GONR/CS electrode was compared with that of the conventional Au sheet electrode in the direct glucose oxidation reaction. As depicted in Fig. 3.8, although the Au sheet has a more negative glucose oxidation potential at 0.14 V, indicating faster mass transfer processes, it produces a current density 80 000 times lower than that of the AuNP/GONR/CS electrode.

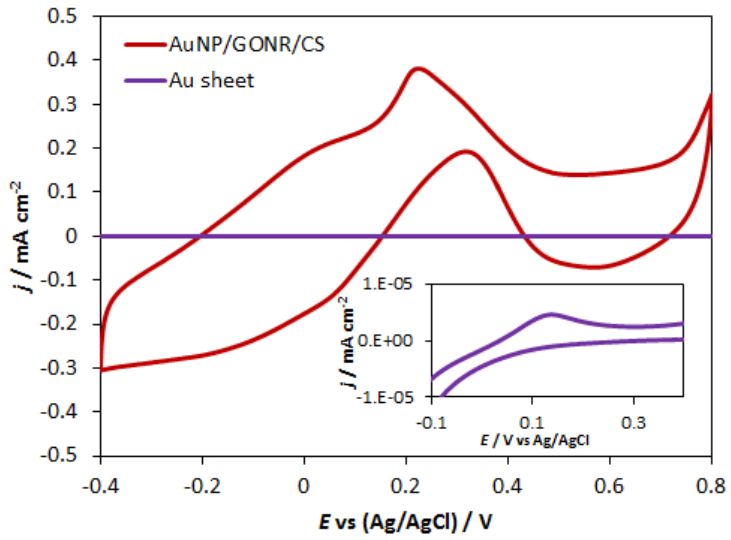

Figure 3.8: Electrocatalytic comparison of AuNP/GONR/CS with Au sheet electrode. The loading of the Au sheet and AuNP/GONR/CS electrodes were 195.8 and 0.1125 mg cm^{-2}, respectively. The electrolyte was 5 mM glucose in 0.1 M PBS and the scan rate was 10 mV/s.

It is worth mentioning that the Au loading of the Au sheet is 200% higher than that of the AuNP/GONR/CS electrode, proving that the high catalytic performance of the hybrid electrode can be attributed to the three–dimensional specific non-covalent interactions between the GONR functional groups and AuNPs active sites with the reactant and intermediates [9]. Low mass transfer on the AuNP/GONR/CS electrode might be due to the complicated intercalation of AuNPs on GONR layers, which delays the diffusion of glucose

toward the AuNPs compared with that on the flat surface of the Au sheet. Furthermore, the higher peak current density of the AuNP/GONR/CS electrode is attributed to the increased AuNP surface area [18] along with the greater number of active sites [24]. To prove this suggestion, we examined the surface area of the Au sheet and AuNP/GONR/CS electrode by running CVs in 10 mM ferricyanide. As expected, the calculation from the CV data in Fig. 3.9 confirmed that the active surface area of the AuNP/GONR/CS electrode is 34.84% higher than that of the Au sheet for a geometric area of 1 cm^2 [19]. This result proved the superior catalytic activity of AuNPs on the GONR supporting matrix by the fact that a 34.84% increase in surface area can induce up to a 200% increase in peak current density.

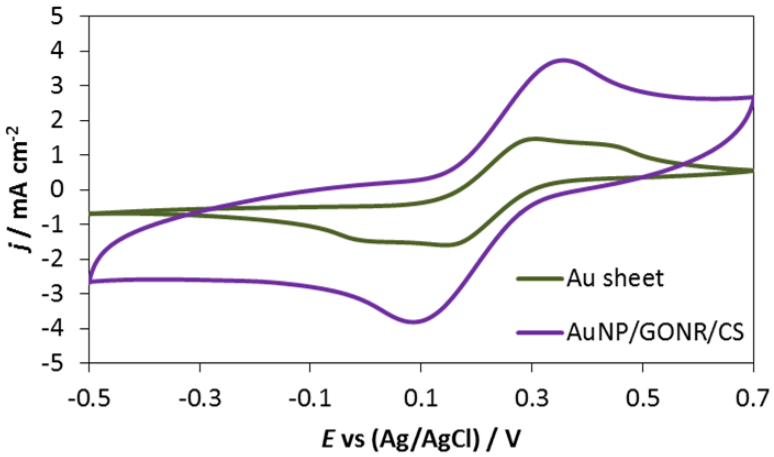

Figure 3.9: Comparison of the active surface area between Au sheet and AuNP/GONR/CS electrodes. The electrolyte was 10 mM $K_3[Fe(CN)_6]$ in 0.1 M PBS.

Leading up to this point, we have so far proven that GONRs play a very important role as a functional supporting matrix in enhancing the catalytic activity of AuNPs in the glucose oxidation reaction, and also act as a backbone to prevent the aggregation of AuNPs. To achieve a better performance of the AuNP/GONR/CS electrode, we carried out further optimization studies on GONR and AuNP loading; the results are described in the following section.

3.3.4 Optimization of GONR and AuNP loadings

The glucose oxidation reaction is remarkably structurally sensitive to the supported Au catalyst [7, 25]. Moreover, the reactivity of Au depends on the supporting matrix (e.g. metal oxide) [23-24] and the particle size [25-26]. Therefore, we optimized the GONR and AuNP loadings to achieve an optimum binding between AuNPs and the GONR supporting matrix while controlling the size of the AuNPs in the AuNP/GONR/CS electrode. The optimized AuNP/GONR/CS electrode was determined from the measured current density of the glucose oxidation peak in 5 mM glucose and the calculated active surface area of AuNPs in 10 mM ferricyanide with PBS (pH 7.0) as supporting electrolyte. Fig. 3.10 (A) shows that increasing the loading of GONR shifts the glucose oxidation peak (V_{ox}) on AuNP/GONR/CS electrode negatively in the forwards scans, and increases the peak current density (I_{peak}) significantly.

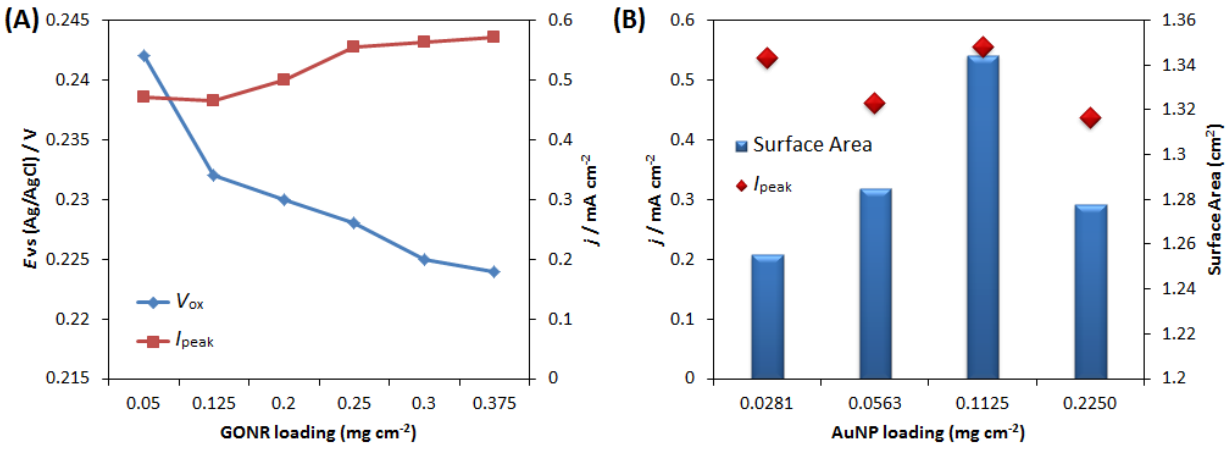

Figure 3.10: (A) Extracted peak current density and glucose oxidation peak of electrodes with various loadings of GONR on CS with a constant AuNP loading of 0.1125 mg cm^{-2}. (B) Comparison of peak current density and active surface area of electrodes with various loadings of AuNPs on GONR/CS. The supporting electrolytes were 5 mM glucose and 10 mM $K_3[Fe(CN)_6]$ in 0.1 M PBS (pH 7.0) for measurements of peak current density and active surface area, respectively.

This phenomenon might be due to the low efficiency of the GONR material, which required a high loading for oxidative reactions, as suggested by Brownson et al. [27], who reported that increasing the edge plane content by increasing the graphene layer leads to an enhancement in heterogeneous electron transfer. On the other hand, the current density of the broad peak at 0 V also increases, which might be because of greater availability of oxygenated functional groups near the AuNPs to form $AuOH_{ads}$, thus promoting glucose oxidation reaction. Furthermore, a sufficient GONR loading prevents the accumulation of AuNPs, resulting in a larger total surface area, as mentioned above. However, more than 0.25 mg cm^{-2} of GONR loading resulted in inhomogeneous and crumbling surface of the electrode (Fig. 3.11). Therefore, we have chosen 0.25 mg cm^{-2} as the optimum GONR loading.

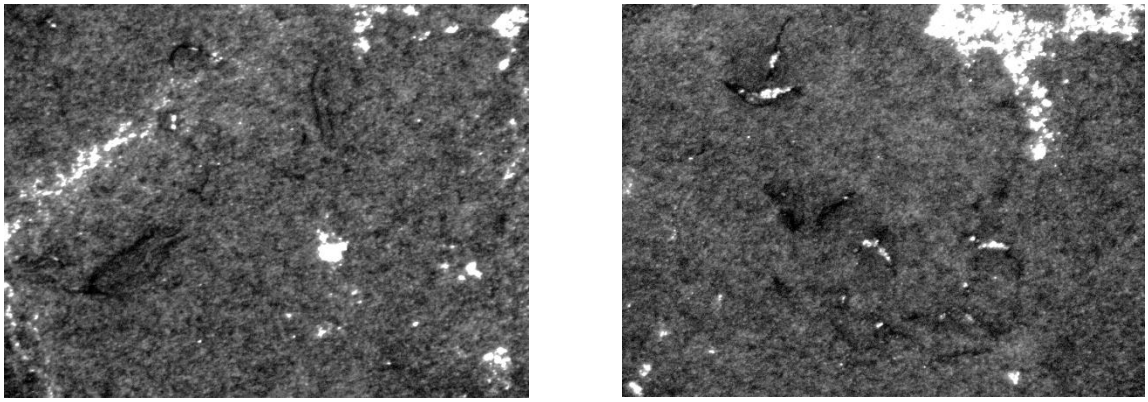

0.300 mg cm^{-2} 0.375 mg cm^{-2}

Figure 3.11: Crumbling surface of AuNP/GONR/CS electrodes due to increasing GONR loading more than 0.25 mg cm^{-2}.

Fig. 3.10 (B) displays the extracted values of peak current density (I_{peak}) and total active surface area of the AuNPs for various AuNP loadings on 0.25 mg cm^{-2} GONRs. Overall, the peak current density and total active surface area increased with increasing AuNP loading up to 0.1125 mg cm^{-2}. Over–loading of AuNPs resulted in a reduction of both

peak current density and active surface area. The SEM images (Fig. 3.12) indicate that the increased AuNP loading caused the aggregation of AuNPs to form larger nanoparticles (≈100 nm in diameter). Consequently, the total active surface area of the aggregated AuNPs decreased, resulting in a reduced peak current density. It is plausible that the non-aggregated particles contributed to the larger exposed active surface area for the glucose oxidation reaction. These results indicate the significant dependence of glucose oxidation on the specific AuNP surface area and diameter. This dependence, in turn, may be related to the difference in adsorption behavior of the reactant on different crystal sites. As the AuNP size decreases, the surfaces at the corners and edges, which serve as active sites for the adsorption/hydrogenation of glucose, increase [25-26]. This dependence is in agreement with the exceptionally high current density at the lowest loading, indicating a larger active surface area of the small AuNPs compared than of the mixture of large and small AuNPs obtained at the higher loading. Hence, the AuNP/GONR/CS electrode with a AuNP loading of 0.1125 mg cm^{-2} demonstrated the best catalytic performance towards the glucose oxidation reaction with the highest peak current density and the largest active surface area of AuNPs. On the basis of the optimum values for the GONR and AuNP loadings, the fabricated AuNP/GONR/CS electrode was tested further in terms of its sensitivity, reproducibility and selectivity.

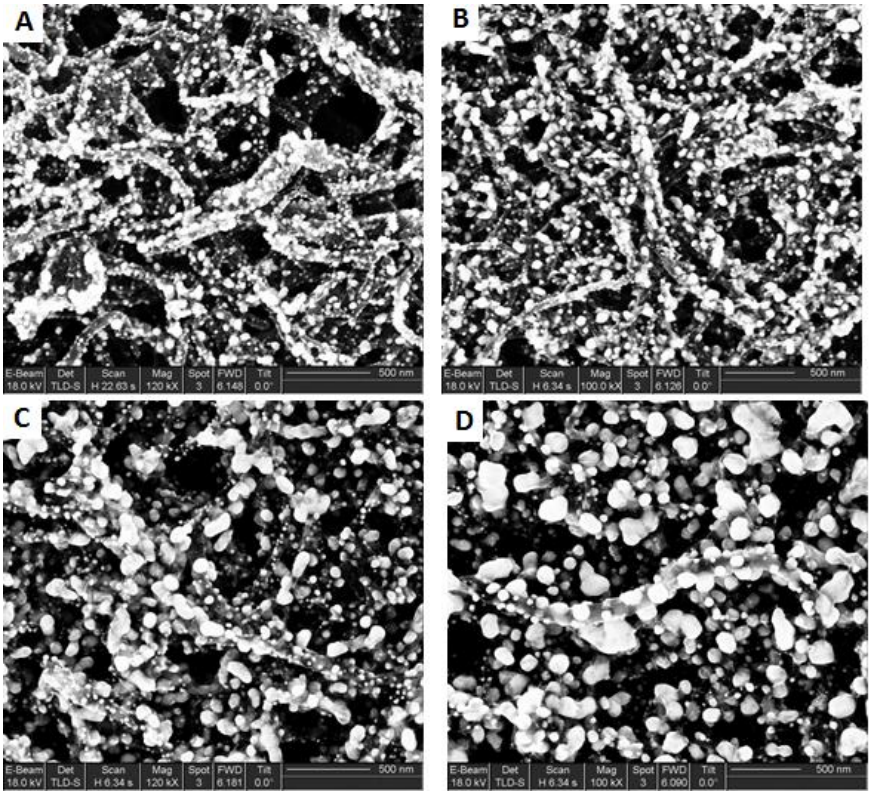

Figure 3.12: SEM images of GONRs/CS electrode with the AuNP loading of (A) 0.0281 mg cm^{-2}, (B) 0.0563 mg cm^{-2}, (C) 0.1125 mg cm^{-2} and (D) 0.2250 mg cm^{-2}. The surface area was calculated using Randle-Sevcik equation with diffusion coefficient, D_0 of 3.52×10^{-5} cm^2 s^{-1} for modified carbon sheet (CS) electrode.

3.3.5 Sensitivity and reproducibility

The sensitivity of the AuNP/GONR/CS electrode was calculated based on the amperometric responses upon addition of glucose into 5 mL stirred 0.1 M PBS solution, which were measured during chronoamperometry (CA) and linear sweep voltammetry (LSV) tests. In order to achieve a well-balanced calibration curve, the addition volume of glucose aliquot was controlled to be not more than 10 µL by diluting 1 M glucose stock solution to several concentrations. A distinct and stable amperometric response with an interval of 40 s can be observed in Fig. 3.13 (A) for the AuNP/GONR/CS electrode at an applied potential of +0.2 V (vs. Ag/AgCl). As shown in the inset of Fig. 3.13 (A), after glucose addition, less than 5 s

was needed for the electrode to achieve 95% of its steady–state current response, indicating rapid and sensitive detection. Meanwhile, Fig. 3.13 (B) shows two linear relationships between the current density and standard glucose concentration extracted from CA data, from 5 µM to 4.92 mM with the sensitivity of 59.1 µA mM^{-1} cm^{-2} (correlation coefficient 0.9989) and from 4.92 to 10 mM with the sensitivity of 31.4 µA mM^{-1} cm^{-2} (correlation coefficient 0.9936). The limit of detection (LOD) found from the CA methods was 5 µM with a signal-to-noise ratio (S/N) of 3. Alternatively, with the LSV method (Fig. 3.13 (C)), the AuNP/GONR/CS electrode was capable of detecting glucose oxidation at +0.227 V and responded to the addition of glucose. The inset displays the respective standard curve, which covers the range from 0.0005 to 10 mM with a sensitivity of 57.1 µA mM^{-1} cm^{-2}. The LOD found from the LSV methods was 0.5 µM, with a S/N of 3. In brief, with the CA method, AuNP/GONR/CS electrode can produce higher sensitivity at the low range of glucose concentration while LSV method can give mediocre sensitivity at the wider range of glucose concentration. In comparison to static applied potential in CA method, LSV employ scanning potential from low to high potential that possible to clean electrode surface after each addition of glucose, which avoid poisoning of electrode and enhance sensitivity. Thus, LSV might be considered as the method of choice for continuous glucose monitoring with an implantable sensor made of our AuNP/GONR/CS catalytic material.

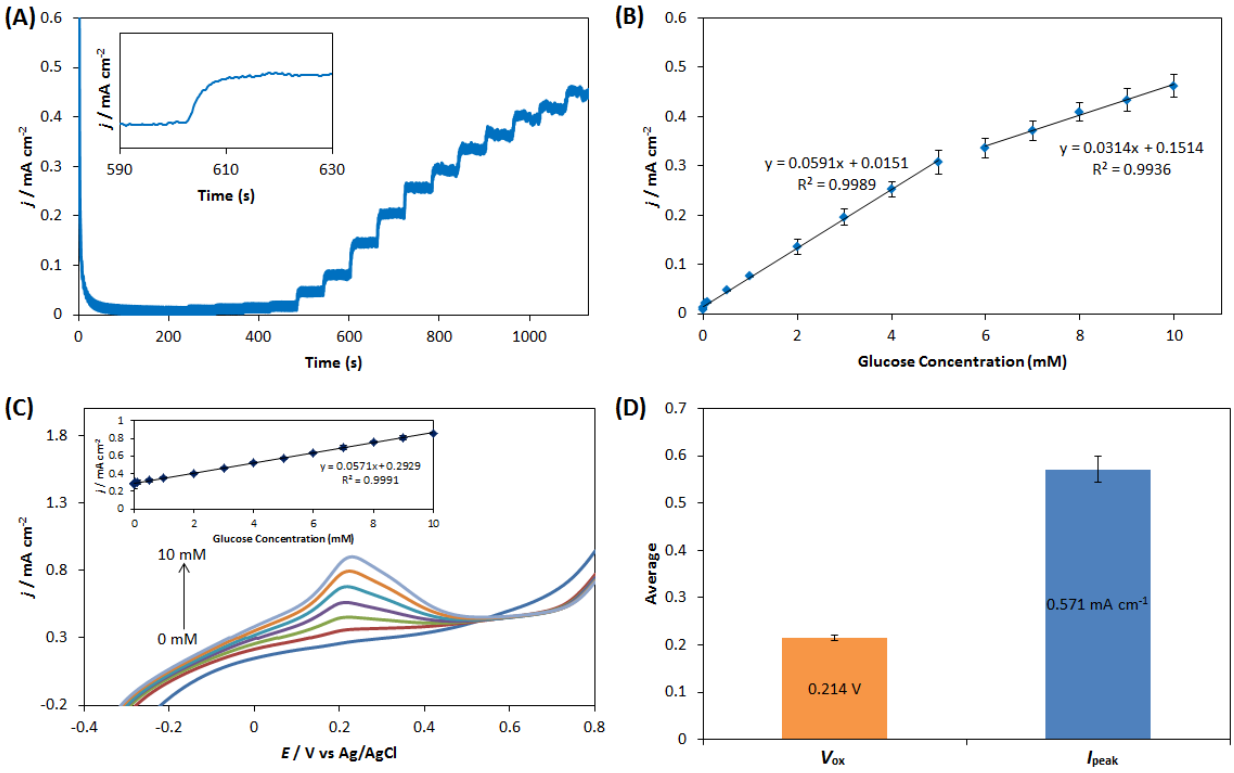

Figure 3.13: (A) Chronoamperometric (CA) responses of AuNP/GONR/CS electrodes upon addition of glucose at +0.2 V. (B) Linear calibration curve based on chronoamperometric response. (C) Linear sweep voltammograms (LSVs) for various concentrations of glucose on AuNP/GONR/CS electrode. (D) Extracted results of peak current density (I_{peak}) and glucose oxidation potential (V_{ox}) from CVs in 5 mM glucose. The supporting electrolyte was 0.1 M PBS (pH 7.0). Scan rate for LSV and CV was 10 mV/s.

The performance of our AuNP/GONR/CS electrode is compared with other well-known catalysts used for non-enzymatic glucose sensing in neutral conditions in Table 3.1. It is observed that the AuNP/GONR/CS electrode exhibits a fast response and excellent detection limit, as well as a wide linear range, which covers the range of physiological glucose level in human blood (3–8 mM), indicating the possibility of practical application of our AuNP/GONR/CS electrode. Moreover, the detection potential for glucose oxidation is lower than that of other Au-based electrodes, indicating the fast kinetic response of our

AuNP/GONR/CS electrode. The wide linear range can be attributed to the numerous electroactive sites and larger surface area for the adsorption of glucose, while the fast and sensitive performance are due to the high catalytic activity afforded by the hybrid structure of AuNPs with a GONR supporting matrix. A reproducibility study of the AuNP/GONR/CS electrodes towards the glucose oxidation reaction was carried out by comparing their I_{peak} and V_{ox} from six electrodes that were prepared in the same batch. The voltammetric response of these electrodes to 5 mM glucose solution was independently tested. The extracted results of I_{peak} and V_{ox} of the fabricated AuNP/GONR/CS electrodes (Fig. 3.13 (D)) gave relative standard deviations (RSD) of 2.72% and 0.57%, respectively, revealing the excellent reproducibility of our sensing material.

Table 3.1. Comparison of analytical performances of various Au and/or graphene-based non-enzymatic glucose sensors in neutral condition.

Electrode	Applied Potential (V)[a]	Detection Limit (μM)	Linear Range (mM)	Sensitivity ($\mu A\ mM^{-1}\ cm^{-2}$)	Ref
AuNP/GONR/CS	+0.20	5	0.005–4.92	59.1	This work
			4.92-10	31.4	
	–0.4 to +0.8 V	0.5	0.0005–10	57.1	This work
PtNFs-GO[b]	+0.49 vs. SCE	2	2–10.3	1.26	[27]
			10.3–20.3	0.64	
PtNi-ERGO[c]	–0.35	10	0.01–35	20.42	[28]
AuNPs integrate nanotube arrays	+0.25	10	1–42.5	1.13	[29]
AuNP/GC[d]	+0.36	4	2–38	NA	[30]

[*a*] vs (Ag/AgCl)

[*b*] Platinum Nickel Nanoparticle - Electrochemical Reduced Graphene Oxide

[*c*] Platinum Nanoflowers – Graphene Oxide

[*d*] Glassy Carbon

3.3.6 Selectivity

One of the major challenges in non-enzymatic glucose sensors is the selectivity of the electrode in the presence of electroactive interferences in blood samples, especially under neutral conditions. Specifically, gold-based catalysts are known to be poisoned by adsorptive

species, which quickly deteriorate the catalytic activities of electrodes. The chloride ion is one of the most problematic inhibiting species because it is present at a high concentration in blood (≈0.1 M). Makovos and Liu [6] have discovered that chloride ions strongly inhibit any response of gold towards the glucose oxidation reaction, even at very low concentrations. They suggested that the presence of chloride ions causes the gold to be dissolved instead of forming an oxide layer for a further oxidation step. As expected, Fig. 3.14 shows the disappearance of the glucose oxidation peak on the voltammogram of the AuNP/GONR/CS electrode in the presence of 0.1 M chloride ions.

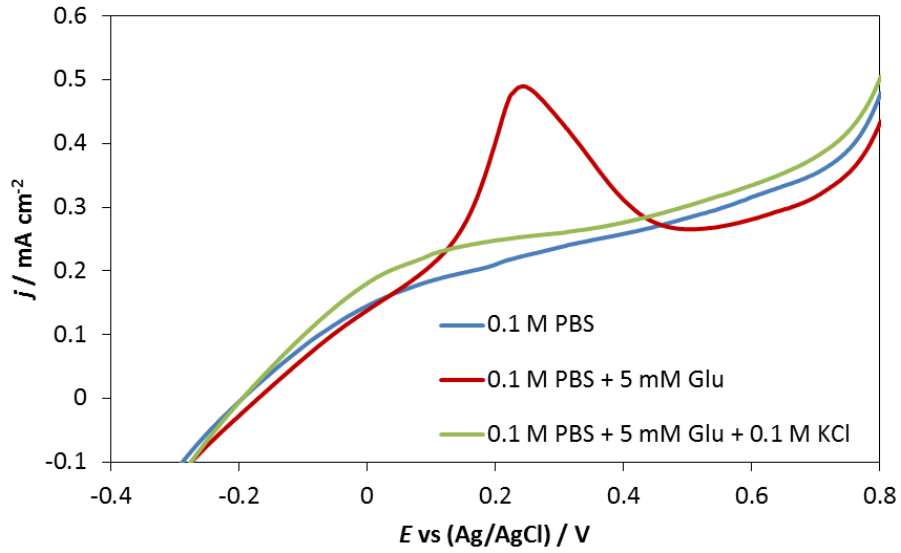

Figure 3.14: LSVs of AuNP/GONR/CS electrode in 0.1 M PBS (pH 7.0) containing 5 mM glucose with and without 0.1 M KCl at a scan rate of 10 mV/s.

This outcome suggested that the AuNP/GONR/CS electrode needs a protective layer to prevent hindrance from chloride ions and other interferences. Some approaches studied to overcome these problems, include permselective coating using Nafion, film electropolymerisation and over potential reduction [32]. In this study, we used an optimized percentage of Nafion and the conducting polymer polypyrrole (PPy) to fabricate a protective membrane for the AuNP/GONR/CS electrode. The PPy-Nafion membrane was made from a

mixture of 0.05% Nafion and 0.2% PPy, which was drop-cast on the AuNP/GONR/CS electrode and allowed to dry at room temperature. The electrocatalytic performance of the two electrodes was compared by studying their LSVs in 5 mM glucose, which showed 53% decrease in peak current density of the PPy-Nafion/AuNP/GONR/CS electrode (Fig. 3.15). The morphology of the coating layer was examined by SEM (Fig. 3.16 (A)) and the film thickness was measured to be ~3310 nm (S/N of 3) by Alpha-Step IQ (KLA-Tencor, USA). This result indicates that the PPy-Nafion coating retards the transport of glucose to the electrode active sites. On the other hand, the LSVs shown in Fig. 3.16 (B) prove that the integration of the PPy-Nafion membrane successfully recovers the glucose oxidation on the AuNP/GONR/CS electrode from the poisoning effect of chloride ions, with a negligible positive shift (≈5 mV) of the glucose oxidation peak. Thus, even though a reduction in current density is observed on the electrode with the protective membrane, the catalytic activity of the AuNPs towards the glucose oxidation reaction can be maintained in the presence of chloride ions.

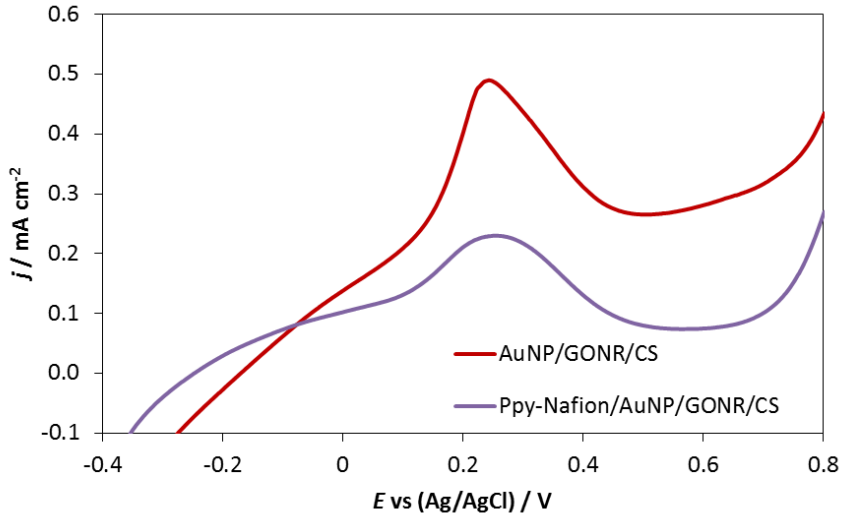

Figure 3.15: LSVs of AuNP/GONR/CS and PPy-Nafion/AuNP/GONR/CS electrodes in 0.1 M PBS (pH 7.0) containing 5 mM glucose at a scan rate of 10 mV/s.

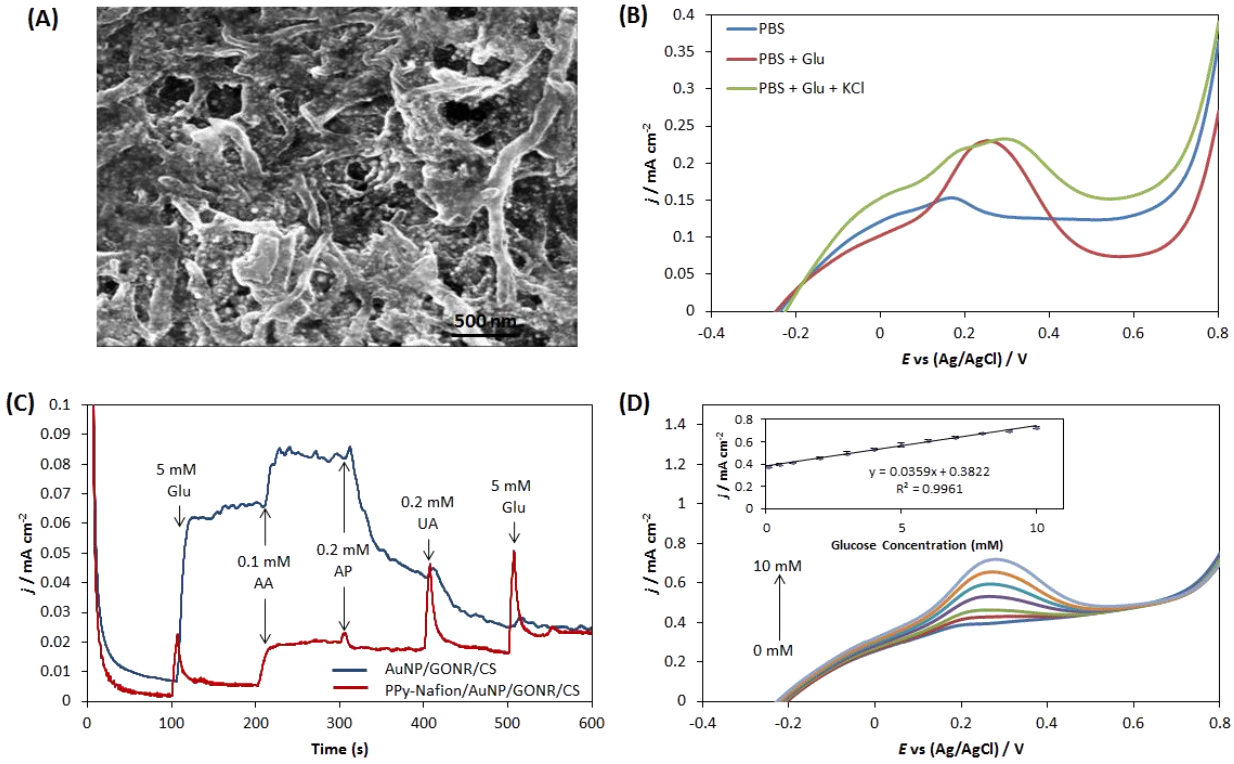

Figure 3.16: (A) SEM image of PPy-Nafion/AuNP/GONR/CS electrode. (B) LSVs of PPy-Nafion/AuNP/GONR/CS electrode in 0.1 M PBS (pH 7.0) containing 5 mM glucose with and without 0.1 M KCl at a scan rate of 10 mV/s. (C) CA responses of AuNP/GONR/CS and PPy-Nafion/AuNP/GONR/CS electrodes upon addition of various interferents. (D) LSVs with various concentrations of glucose on PPy-Nafion/AuNP/GONR/CS electrode.

Further investigations were made with other interferents that exist naturally in blood, including ascorbic acid (AA), *p*-acetamidophenol (AP), and uric acid (UA) [32]. The selectivities of both the AuNP/GONR/CS and PPy-Nafion/AuNP/GONR/CS electrodes were observed through their chronoamperometric responses upon the addition of glucose and interferent species at an applied potential of +0.2 V. As illustrated in Fig. 3.16 (C), although the protective membrane gave a reduction in the glucose response, it improved the selectivity of the AuNP/GONR/CS electrode significantly. In the case of AA, the increment of the current density was reduced by 43% with the PPy-Nafion protective membrane. Both

electrodes exhibited a high response towards AA addition, which might be because ascorbate ions are the predominant species at typical biological pH values, and are oxidized at the same potential as glucose. In contrast to the effect of AA, the addition of AP resulted in a drastic reduction in current density (58%) owing to its strong inhibition on the surface of the AuNP/GONR/CS electrode. The PPy-Nafion/AuNP/GONR/CS electrode, however, reduced this suppression of current density to around 11%. The protective membrane also worked successfully in the case of UA. As shown in the CA response, the addition of UA resulted in a significant reduction in current density in the case of the AuNP/GONR/CS electrode (45%), while only a small change (2%) was observed in the case of the PPy-Nafion/AuNP/GONR/CS electrode. The suppression of the glucose oxidation reaction on the AuNP/GONR/CS electrode in the presence of AP and UA suggests the strong adherence of these electroactive species on the AuNP surfaces. The use of the PPy-Nafion membrane decreased significantly the AuNPs poisoning from AP and UA interferents by charge repulsion, as proved by the above mentioned results. The final addition of glucose showed a 3% current drop on the AuNP/GONR/CS electrode, while the electrode with the protective membrane showed a 32% increase in current density. This result indicates that the surface of the AuNP/GONR/CS electrode was poisoned completely by the electroactive species, and that the PPy-Nafion membrane is essential for recovering the catalytic activity of the AuNPs towards the glucose oxidation reaction. Finally, the sensitivity of the PPy-Nafion/AuNP/GONR/CS electrode towards the addition of glucose was investigated using LSV method, as depicted in Fig. 3.16 (D). The inset displays the standard calibration curve, which covers the range 0.05 to 10 mM with an LOD of 50 μM. The sensitivity of the PPy-Nafion/AuNP/GONR/CS electrode was determined to be 35.9 $\mu A\ mM^{-1}\ cm^{-2}$ at the S/N ratio of 3, which is quite high in comparison with other reported electrodes (Table 3.1). The reduction in the sensitivity and detection limit is due to the addition of a diffusion layer by

the PPy-Nafion protective membrane. Further improvement of the protective membrane is therefore needed before the application stage.

3.4 Conclusions

In summary, we have designed, synthesized and optimized a nanocomposite of AuNPs with GONRs, through simple deposition on carbon sheet and activation by thermal treatment. The catalytic activity of AuNP/GONR/CS towards the glucose oxidation reaction has been studied and compared to that of a Au sheet and AuNP/CS in neutral conditions. The intercalation of AuNPs with GONRs resulted in 200% and 121.22% increments in glucose oxidation current density compared with those of the bare Au sheet and AuNP/CS, respectively, as revealed by CV data. Consequently, GONRs have been identified to act as a three-dimensional backbone with oxygenated functional groups that form non-covalent interactions with AuNP active sites to promote the reaction kinetics. Further application of the AuNP/GONR/CS electrode in glucose detection showed a wide linear calibration curve between 0.0005 and 10 mM and good sensitivity, as tested by using the LSV method. Although AuNPs exhibit poisoning and strong inhibition of glucose oxidation by chloride ions and other electroactive interferents, a protective membrane made of 0.2% polypyrrole and 0.05% Nafion was utilized to recuperate the catalytic activity of the AuNPs successfully. Further work to improve the protective membrane and investigate other interference effects is being undertaken in our laboratory, paving the way for future developments of *in-vivo* non-enzymatic glucose sensors.

3.5 References

[1] T. Scully, Diabetes in numbers, *Nature Outlook* **485** (2012) S2-S3.

[2] E. Dolgin, Managed by machine, *Nature Outlook* **485** (2012) S6-S8.

[3] S. Park, H. Boo, T.D. Chung, Electrochemical non-enzymatic glucose sensor, *Analytica Chimica Acta* **556** (2006) 46.

[4] G. Wang, X. He, L. Wang, A. Gu, Y. Huang, B. Fang, B. Geng, X. Zhang, Non-enzymatic electrochemical sensing of glucose, *Microchim Acta* **180** (2013) 161.

[5] Y.B. Vassilyev, O.A. Khazova, N.N. Nikolaeva, Kinetics and mechanism of glucose electrooxidation on different electrode catalyst. Part II: Effect of the nature of the electrode and the electrooxidation mechanism, *J. Electronal. Chem.* **196** (1985) 127.

[6] E.B. Makovos, C.C. Liu, A cyclic-voltammetric study of glucose oxidation on a gold electrode, *Bioelectrochemistry and Bioenergetics* **15** (1986) 157.

[7] R.R. Adzic, M.W. Hsiao, E.B. Yeager, Electrochemical oxidation of glucose on single cystal gold surfaces, *J. Electroanal. Chem.* **260** (1989) 475.

[8] M.W. Hsiao, R.R. Adzic, E.B. Yeager, Electrochemical oxidation of glucose on single crystal and polycrystalline gold surfaces in phosphate buffer, *Journal of Electrochemical Society* **143** (1996) 759.

[9] L.Q. Hoa, M.C. Vestergaard, H. Yoshikawa, M. Saito, E. Tamiya, Enhancing catalytic performance of Pt-based electrode with a noncovalent interaction-induced functionalized carbon nanotube-grafted matrix, *J. Mater. Chem.* **22** (2012) 14705.

[10] A.K. Geim, K.S. Novoselov, The rise of graphene, *Nat. Mater. 6* (2007) 183.

[11] T. Kuila, S. Bose, A.K. Mishra, P. Khanra, N.H. Kim, J.H. Lee, Chemical functionalization of graphene and its applications, *Prog. in Mater. Sci.* **57** (2012) 1061.

[12] S. Park, R.S. Ruoff, Chemical methods for the production of graphenes, *Nature Nanotechnology* **4** (2009) 217.

[13] D.V. Kosynkin, A.L. Higginbotham, A. Sinitskii, J.R. Lomeda, A. Dimiev, B.K. Price, J.M. Tour, Longitudinal unzipping of carbon nanotunes to form graphene nanoribbons, *Nature* **458** (2009) 872.

[14] A.L. Hogginbotham, D.V. Kosynkin, A. Sinitskii, Z. Sun, J.M. Tour, Lower-defect graphene oxide nanoribbons from multiwalled carbon nanotubes, *ACS Nano* **4** (2010) 2059.

[15] Y. Hu, J. Jin, P. Wu, H. Zhang, C. Cai, Graphene-gold nanostructure composites fabricated by electrodeposition and their electrocatalytic activity toward the oxygen reduction and glucose oxidation, *Electrochimica Acta* **56** (2010) 491.

[16] F.Y. Kong, X.R. Li, W.W. Zhao, J.J. Xu, H.Y. Chen, Graphene oxide-thionine-Au nanostructure composites: preparation and application in non-enzymatic glucose sensing, *Electrochemistry Communications* **14** (2012) 59.

[17] J. Naruse, L.Q. Hoa, Y. Sugano, T. Ikeuchi, H. Yoshikawa, M. Saito, E. Tamiya, Development of biofuel cells based on gold nanoparticle decorated multi-walled carbon nanotubes, *Biosensor & Bioelectronics* **30** (2011) 204.

[18] C Jin, I. Taniguchi, Electrocatalytic oxidation of glucose on gold nanocomposite electrodes, *Chem. Eng. Technol.* **30** (2007) 1298.

[19] H-F. Cui, J-S Ye, W-D Zhang, C-M Li, J.H.T. Luong, F-S. Sheu, Selective and sensitive electrochemical detection of glucose in neutral solution using platinum-lead alloy nanoparticle/carbon nanotube nanocomposites, *Anal. Chim. Acta* **594** (2007) 175.

[20] K.N. Kudin, B. Ozbas, H.C. Schniepp, R.K. Prud'homme, I.A. Aksay, R. Car, Raman spectra of graphite oxide and functionalized graphene sheets, *Nano Lett* **8** (2008) 36.

[21] A.C. Ferrari, J.C. Meyer, V. Scardaci, C. Casiraghi, M. Lazzeri, F. Mauri, S. Piscanec, D. Jiang, K.S. Novoselov, S. Roth, A.K. Geim, Raman spectrum of graphene and graphene layers, *Physical Review Letters* **97** (2006) 1.

[22] N. Saliba, D.H. Parker, B.E. Koel, Adsorption of oxygen on Au (111) by exposure to

ozone, *Surface Science* **410** (1998) 270.

[23] T. Ishida, N. Kinoshita, H. Okatsu, T. Akita, T. Takei, M. Haruta, Influence of the support and the size of gold clusters on catalytic activity for glucose oxidation, *Angewandte Chemie* **120** (2008) 9405.

[24] M. Haruta, When gold is not noble: catalysis by nanoparticles, *The Chemical Record* **3** (2003) 75.

[25] Y. Önal, S, Schimpf, P. Claus, Structure sensitivity and kinetics of D-glucose oxidation to D-gluconic acid over carbon-supported gold catalysts, *J. Catalysis* **223** (2004) 122.

[26] M. Mavrikakis, P. Stoltze, J.K. Nørskov, Making gold less noble, *Catalysis Letters* **64** (2000) 101.

[27] D.A.C. Brownson, D.K. Kampouris, C.E. Banks, Graphene electrochemistry: fundamental concepts through to prominent applications, *Chem. Soc. Rev.* **41** (2012) 6944.

[28] G. Wu, X. Song, Y. Wu, X. Chen, F. Luo, X. Chen, Non-enzymatic electrochemical glucose sensor based on platinum nanoflowers supported on graphene oxide, *Talanta* **105** (2013) 379.

[29] H. Gao, F. Xiao, C.B. Ching, H. Duan, One-step electrochemical synthesis of PtNi nanoparticle-graphene nanocomposite for nonenzymatic amperometric glucose detection, *ACS Applied Material Interfaces* **3** (2011) 3049.

[30] Y.G. Zhou, S. Yang, Q.Y. Qian, X.H. Xia, Gold nanoparticles integrated in a nanotube array for electrochemical detection of glucose, *Electrochemistry Commun.* **11** (2009) 216.

[31] H. Zhang, J. Xu, H. Chen, Shaped-controlled gold nanoarchitectures: synthesis, superhydrophobicity, and electrocatalytic properties, *J. Phys. Chem. C* **112** (2008) 13886.

[32] K.E. Toghill, R.G. Compton, Electrochemical non-enzymatic glucose sensors: a perspective and an evaluation, *J. Electrochem. Sci.* **5** (2010) 1246.

CHAPTER 4

ENHANCED ELECTROCHEMILUMINESCENCE OF *N*-(AMINOBUTYL)-*N*-(ETHYLISOLUMINOL) FUNCTIONALIZED GOLD NANOPARTICLES BY GRAPHENE OXIDE NANORIBBONS

4.1 Introduction

Electrochemiluminescence or electrogenerated luminescence (ECL) has become an important detection method in analytical chemistry due to its simplicity, rapidity and high sensitivity [1-2]. ECL possess several advantage over chemiluminescence (CL) technique; electrochemical reaction allows the time and position of the light-emitting reaction to be controlled and more selective due to generation of excited states in ECL can be selectively controlled by varying the electrode potentials as depicted in Fig. 4.1 [3].

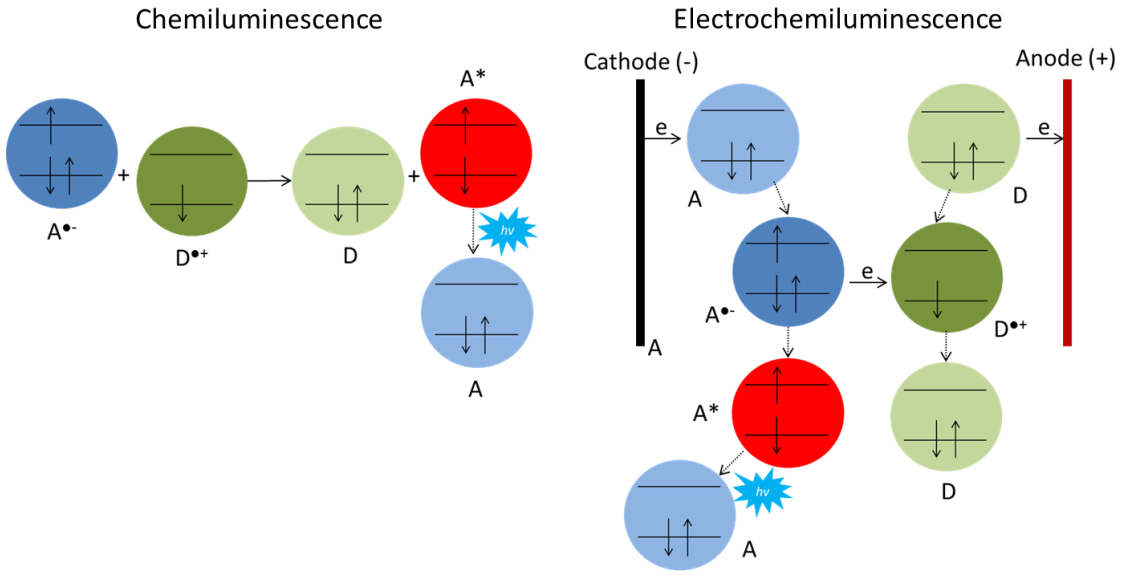

Figure 4.1: Schematic diagram of general mechanism of CL and ECL [3].

Luminol (3-amino-phthalhydrazide) is the most widely used ECL reagent where decomposition of a luminol results in the production of excited states (3-amino-phthalate, 3-AP*) and emission of blue light through an annihilation process [4]. Many studies have been devoted to understanding the mechanism of luminol ECL in luminol-hydrogen peroxide (H_2O_2) system [5-7]. Since H_2O_2 play an important role in generating oxygen-related radical for interaction with luminol radical, two main focuses were considered in finding the suitable catalyst. First, peroxidase- or oxidase-based enzyme was utilized to catalyze the production of H_2O_2 [8-9]. Second, noble metal was used to accelerate the generation of oxygen-related radical for rapid and enhanced ECL intensity [10-11]. Previous research has revealed that the behavior of luminol ECL is highly dependent on pH of buffer solution, which prefers alkaline conditions. Enzyme gives major drawback in terms of very expensive, sensitive to temperature, and required complex binding on the electrode surface [12]. Moreover, enzymatic reaction only works in neutral conditions [13]. On the other hand, noble metal catalyst, especially gold (Au) is very reactive in alkaline conditions caused by hydroxide anions promote noncovalent interactions on metal active sites that significantly enhance its reactivity, which make it compatible with the luminol oxidation reaction [14]. Furthermore, Au proved to enhanced chemiluminescence (CL) and ECL activity, particularly in nanoparticle form. However, the catalytic performance of gold nanoparticle (AuNP) in luminol ECL was reliant to particle size [15], nature of the support matrix [16] and preparation method [17-18].

Recently, we have reported the catalytic activity of AuNPs was enhanced by using graphene oxide nanoribbons (GONRs) as a functional supporting matrix for a non-enzymatic glucose sensor [19]. Graphene is a single-atomic-layer honeycomb lattice of carbon atoms in an sp^2 hexagonal bonding configuration which is the basic building block for other carbon materials [20]. One of the improved techniques in chemically derived graphene is the

longitudinal unzipping of CNTs to form graphene oxide nanoribbons (GONRs) by using oxidizing agents in strong acidic conditions, followed by a reduction process to finally achieve graphene nanoribbons [21]. Owing to the strong oxidative reaction during unzipping process, the resulting GONRs are highly soluble in water and polar solvents, with an attractive surface and edges containing oxygen functional groups [21-22]. Utilization of GONR contributed to the high total surface area of the AuNPs and formed three-dimensional specific interaction between the functional groups on the GONRs and the AuNP active sites with the reactant and the intermediates that promote the reaction kinetics [19]. However, the burst nucleation method used in producing AuNPs required the usage of hexane as surfactant to avoid aggregation of particles. As a consequent, high thermal treatment at 400 °C is necessary after electrode fabrication to remove the surfactant on the AuNP surface. The thermal treatment step was necessary not only to activate the AuNP catalytic surface by removing the stabilizing agents, but also to bind AuNPs on the GONRs for stability enhancement [19]. Unfortunately, our ECL setup required utilization of SPE made of glass epoxy substrate that incapable to withstand high temperature treatment [23]. Therefore, direct synthesis of AuNP that is free from surfactant is compulsory.

Cui's group has reported direct synthesis of AuNP using luminol derivative, *N*-(aminobutyl)-*N*-(ethylisoluminol) (ABEI), as reducing agent through seed growth method at room temperature [24]. This simple method capable of producing ABEI coated on AuNP surface without additional surfactant. As a result, this particle can illuminate by itself without supplementary luminol in solution, thus make it a desirable label especially in immunosensor [25]. To the best of our knowledge, the catalytic performance of this particle hasn't been studied on any supporting matrix except cysteine linker [26]. Herein, for the first time, we investigate the performance of ABEI functionalized gold nanoparticles hybrid with graphene oxide nanoribbons on a carbon screen printed electrode (ABEI-AuNP-GONR/SPE) towards

ECL of ABEI in alkaline conditions. Furthermore, the catalytic performance of the ABEI-AuNP without GONR supporting matrix on SPE is studied. In addition, ECL of ABEI in aqueous alkaline condition on bare SPE and GONR modified SPE is performed to further elucidate the ECL mechanism of ABEI-AuNP-GONR/SPE. These interesting results obtained may provide an insight for further improvements of ECL sensors through the utilization noble metal and GONRs as a functional supporting matrix on SPE. As a step further, we have successfully utilized ABEI-AuNP-GONR/SPE in enzymatic biosensor development. The usage of SPE has great potential for implementation in portable, rapid and sensitive point of care device.

4.2 Experimental

4.2.1 Materials and reagents

Multi-walled carbon nanotubes (MWCNTs), hydrogen tetrachloroaurate (III) tetrahydrate ($HAuCl_4.4H_2O$), 0.1 M sodium hydroxide (NaOH), concentrated sulfuric acid (H_2SO_4), potassium permanganate ($KMnO_4$), 30% hydrogen peroxide (H_2O_2), ethanol and ether were obtained from Wako Co., Japan. *N*-(4-aminobutyl)-*N*-ethylisoluminol was purchased from Tokyo Chemical Industry Co. Ltd., Japan. Carbonate buffer solution (CBS, 0.1 mol L^{-1}, pH 9.02- 10.72) was prepared from Na_2CO_3 and $NaHCO_3$. Ultrapure water obtained from Barnstead Nanopure water purification system (18 MΩ, Thermo Scientific, USA) was used in all experiments.

4.2.2 Synthesis of GONRs

GONRs were synthesized through the method of longitudinal unzipping of MWCNTs [21]. In brief, MWCNTs were suspended in concentrated H_2SO_4 for 12 h, and then treated with $KMnO_4$. The mixture was stirred at room temperature for 1 h, and heated at 55 to 70 °C for a

further 1 h. After all the $KMnO_4$ had been consumed, the reaction was quenched by pouring the mixture into ice containing 1.25% H_2O_2. The solution was filtered through a polytetrafluoroethylene (PTFE) membrane. The remaining solid was washed with HCl and ethanol/ether alternately between filtrations. The final product was dried *in vacuo*.

4.2.3 Synthesis of ABEI-AuNP

AuNPs were synthesized through a seed growth method using the *N*-(aminobutyl)-*N*-(ethylisoluminol) (ABEI) as the reducing agent [24]. First, stock solutions of $HAuCl_4 \cdot 4H_2O$ in water (5.9 mM) and ABEI in NaOH (4 mM) were prepared. Then, $HAuCl_4$ stock solution (9 mL) was mixed with water (45 mL). ABEI stock solution (6 mL) was added rapidly while stirring. The reaction mixture was stirred at room temperature for 2 h. After that, $HAuCl_4$ stock solution (6 mL) was added and the reaction mixture was continuously stirred for another 2 h. Finally, the mixture was dialyzed for 3 days with frequent change of water to remove unreacted reagent. The produced AuNPs coated with ABEI molecules (ABEI-AuNP) were kept at 4 °C when not used.

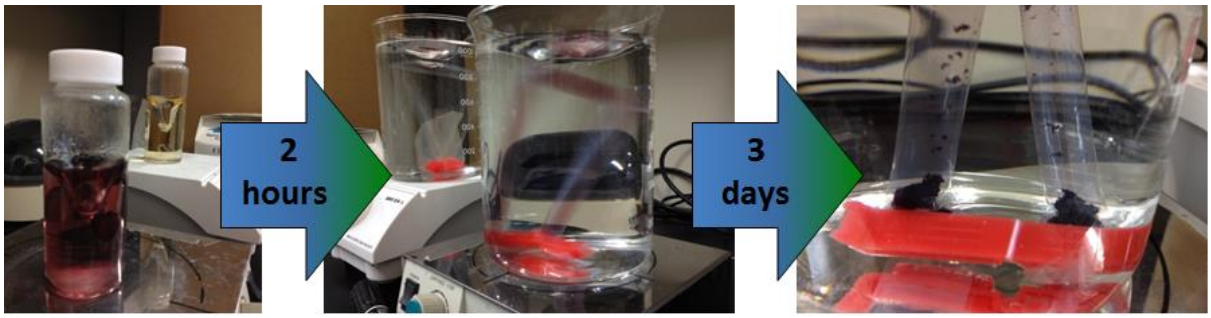

Figure 4.2: Synthesis of ABEI-AuNPs through seed growth method.

4.2.4 Fabrication of ABEI-AuNP and ABEI-AuNP-GONR modified SPE

Screen printed electrode (SPE) was used for all electrochemical measurements. The carbon based SPE contained a three-electrode system; working electrode, counter electrode and the

Ag/AgCl reference electrode. The working electrode area is 2.64 mm^2 and the total size including the connection part and the carbon barrier to prevent the solution from flowing into the connector is 12.5 mm x 4 mm x 0.3 mm [27]. Small volume of solution (20 μL) was applied directly onto the electrode surface and SPE was discarded after a single use.

Surface modification of SPE working electrode was done by the drop casting method. First, GONRs (1 mg) were sonicated and dispersed in 1 mL water. Then, the mixture of as-prepared ABEI-AuNP and GONR was sonicated for 30 min. Finally the mixture of ABEI-AuNP-GONR (2 μL) was cast on SPE working electrode and dried at room temperature overnight. For comparison purpose, ABEI-AuNP modified SPE was prepared by direct casting of as-prepared ABEI-AuNP (2 μL) on working electrode.

4.2.5 Characterization of ABEI-AuNP-GONR material and ECL measurement

The formation of AuNPs by reduction of $HAuCl_4$ with ABEI was confirmed by UV-Vis spectrophotometer (Shimadzu UV-2550, Japan). The functional groups on the ABEI-AuNPs and GONRs were confirmed by attenuated total reflectance–Fourier transform infrared (ATR-FTIR) spectroscopy (Horiba FT-720, Japan). The morphologies of the catalytic materials were acquired by scanning electron microscopy (SEM) using a DB 235 microscope (FEI Co.). All electrochemical measurements were performed with a USB-powered handheld potentiostat (BDTminiSTAT100; Biodevice Technology Co. Ltd., Japan) [28]. This portable potentiostat can be controlled and powered by connecting to the USB port of a laptop without additional external power supply. ECL of ABEI was observed through EM-CCD digital camera and recorded with AquaCosmos software while ECL intensity was measured by photon detector unit (Hamamatsu Photonics, Japan).

4.3 Results and Discussion

4.3.1 Characterization of ABEI-AuNP-GONR/SPE

Formation of ABEI-AuNP was confirmed by UV-Vis absorption spectra of ABEI and $HAuCl_4$ precursor before and after reduction process as demonstrate in Fig. 4.3. ABEI stock solution shows the absorption peak and shoulder at 290 and 320 nm, respectively [24]. Meanwhile, $HAuCl_4$ absorption peak was observed at 290.5 nm. The mixture of ABEI and $HAuCl_4$ after stirring for total 4 h demonstrate absorption peak shift to 298 nm and shoulder shift to 350 nm with the appearance of small peak at 525 nm indicating formation of AuNP. After completing three days of dialysis process, the mixture showed a decreased in ABEI absorbance intensity but increased in gold absorbance intensity. This result suggests that concentration of ABEI reduced after reaction with $HAuCl_4$ to form AuNPs. Moreover, the existence of both ABEI and Au peaks might indicate the resultant AuNPs were coated with ABEI molecules since the dialysis supernatant was cleared from any substance. The size of as-prepared ABEI-AuNPs were confirmed to be ~38 nm (Fig. 4.4).

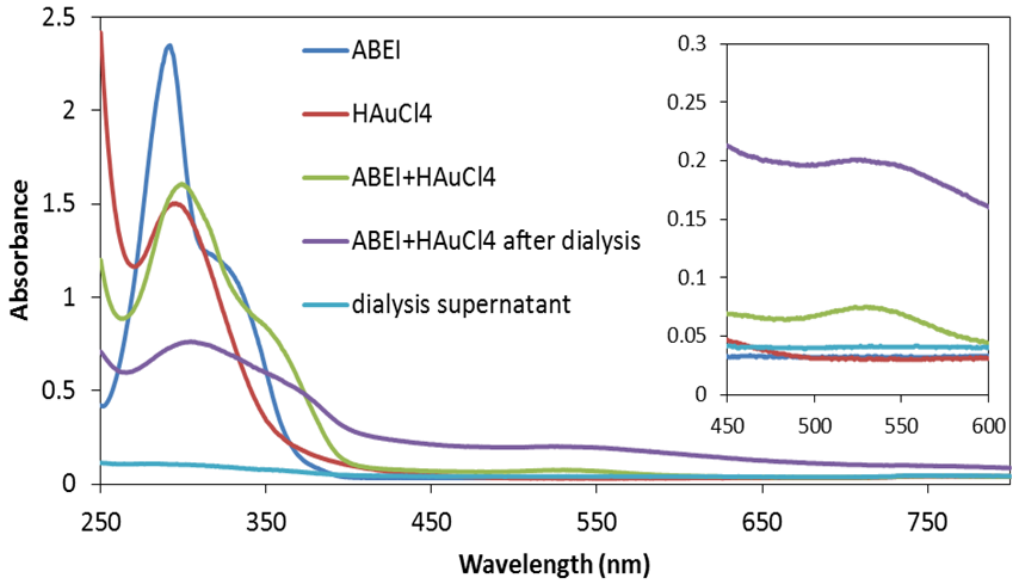

Figure 4.3: UV-Vis spectra of individual and mixture of ABEI and $HAuCl_4$ precursor in seed growth method to form ABEI-AuNPs

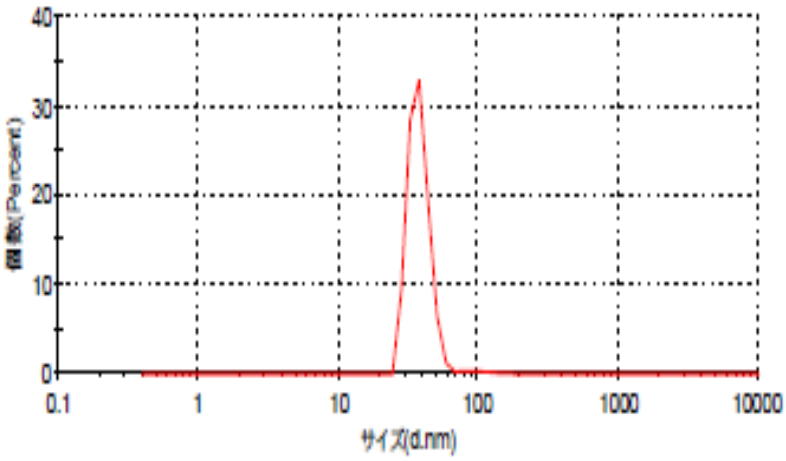

Figure 4.4: Size of ABEI-AuNP

After confirmed the formation of ABEI-AuNPs, as-prepared ABEI-AuNPs and ABEI-AuNP-GONR mixture were dropped-cast (2 µL) on the working electrode of SPE. Fig. 4.5 (A) shows the SEM image of the bare SPE working electrode that was made of carbon paste before surface modification. ABEI-AuNP modified SPE (ABEI-AuNP/SPE) displays aggregation of ABEI-AuNP to form gold (Au) layer (Fig. 4.5 (B)). On the other hand, mixture of ABEI-AuNP and GONR produced a homogenous layer of ABEI-AuNP-GONR modified SPE (ABEI-AuNP-GONR/SPE) as depicted in Fig. 4.5 (C) with a particle size of ABEI-AuNPs could be maintained. This result might suggest that oxygen functional groups on GONR might formed electrostatic bonding with ABEI-AuNPs, which hinder the aggregation process. It is expected that these functional groups in the GONR matrix play an important role in enhancement of ECL of ABEI-AuNPs in solid-liquid interface. Further characterizations of each catalytic material towards the ECL of ABEI under alkaline conditions are presented in the following sections.

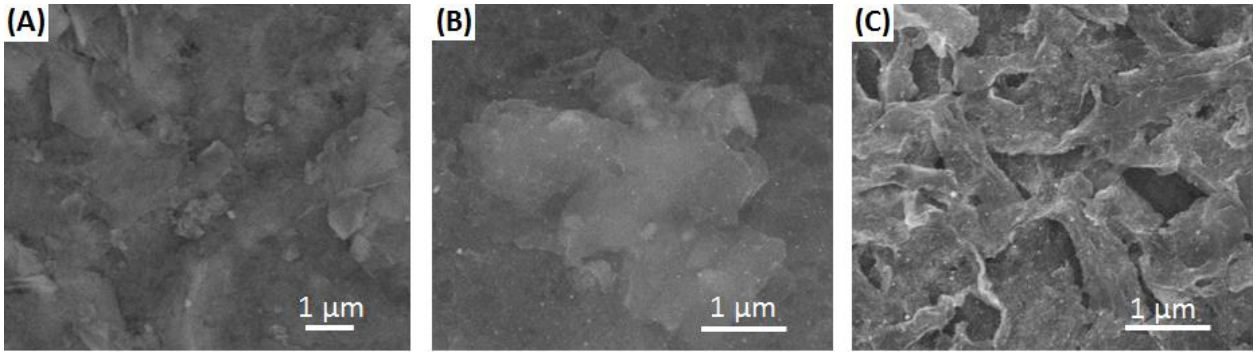

Figure 4.5: SEM images of (A) SPE, (B) ABEI-AuNP/SPE and (C) ABEI-AuNP-GONR/SPE.

4.3.2 ECL of ABEI-AuNP-GONR modified SPE

General ECL of the luminol-H_2O_2 system can be referred to schematic in Fig. 3 [1]. Luminol and H_2O_2 dissociate to luminol monoanion (LH^-) and hydrogen peroxide anion (HOO^-), respectively. Then, the HOO^- is oxidized to oxygen via hydroperoxy radical $HOO^{\bullet-}$ while LH^- is oxidized to 3-amino-phthalate (3-AP) via diazasemiquinone radical ($LH^{\bullet-}$) during forward scan [30]. Later, $LH^{\bullet-}$ react with superoxide radical ($O_2^{\bullet-}$), which produce through dissociation of $HOO^{\bullet-}$ intermediates, to yield hydroperoxy intermediate (LOO^-) that become excited state of 3-amino-phthalate (3-AP*) by releasing nitrogen. In consequence, the 3-AP* returns to ground state by emitting fluorescence [1,4,5,30].

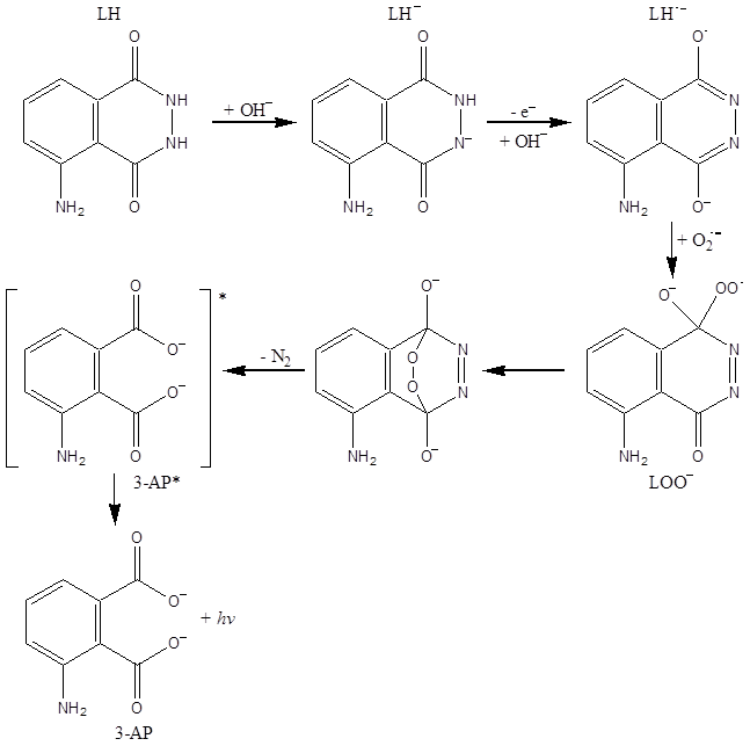

Figure 4.6: The basic mechanism for ECL of luminol

In order to understand the ECL mechanism of ABEI on ABEI-AuNP-GONR/SPE, we investigated through cyclic voltammetry (CV) on each catalytic material separately as depicted in Fig. 4.7. To begin with, SPE and GONR modified SPE (GONR/SPE) were tested in 0.364 mM ABEI solution. The concentration of ABEI tested on SPE and GONR/SPE was predicted equal to the total concentration of ABEI molecules on AuNPs cast on working electrode; based on calculation from starting stock solution during the synthesis process. Then, ABEI-AuNP/SPE and ABEI-AuNP-GONR/SPE were tested in plain buffer without additional ABEI solution. This process step was necessary not only to investigate the role of GONR in ECL but also to prove that ABEI molecules were coated on AuNPs.

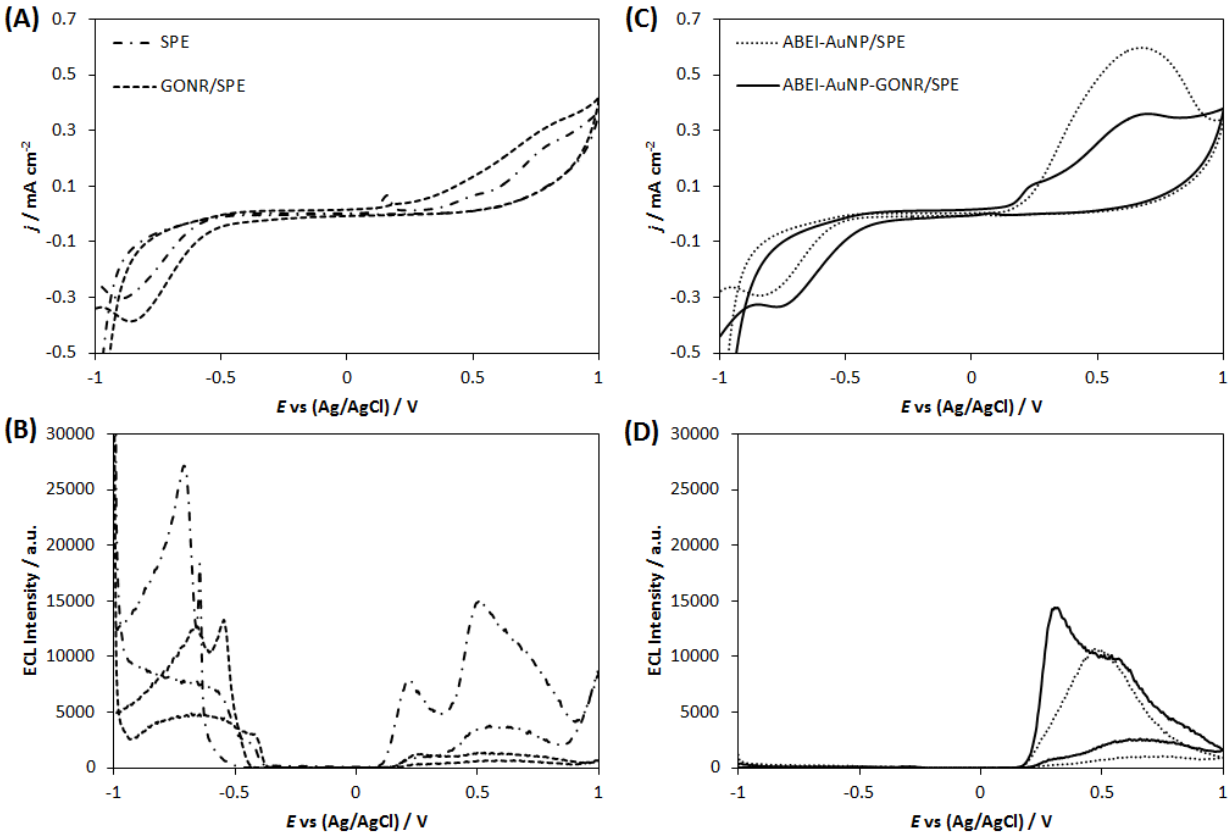

Figure 4.7: (A) CVs and (B) ECL intensities of SPE and GONR/SPE in 0.364 mM ABEI solution. (C) CVs and (D) ECL intensities of ABEI-AuNP/SPE and ABEI-AuNP-GONR/SPE. Supporting electrolyte was 1 mM H_2O_2 in 0.02 M CBS (pH 9.85).

Fig. 4.7(A) shows CV of SPE in ABEI solution produced three oxidation peaks during forward scan at +0.135, +0.475 and +0.78 V with one reduction peak at -0.907 V during reverse scan. The corresponding ECL intensity spectrum in Fig. 4.7(B) reveals only two ECL peaks appeared at +0.210 and +0.505 V during forward scan while reverse scan produced two ECL peaks at -0.645 and -0.710 V. To distinguish the mechanism on each peak in CV and ECL intensity spectrum, each component of testing solutions on SPE were compared as depicted in Fig. 4.8. Based on previous research on ECL of luminol on paraffin-impregnated graphite electrode, the first anodic ECL peak was identified due to direct electro-oxidation of luminol to $LH^{\bullet-}$, which consequently converted into 3-AP* with or

without dissolved oxygen (O_2) existence to emit light [31]. The second anodic ECL peak was relied on the first oxidation peak (Fig 4.9), which indicates that $LH^{\bullet-}$ intermediate produced from first oxidation process involved in the second oxidation process. The conversion of $LH^{\bullet-}$ to 3-AP* in second anodic ECL peak may occur by (i) interaction with O_2, (ii) electrochemically oxidized [31] or (iii) oxidation of HOO^- to $O_2^{\bullet-}$ that consequently interact with $LH^{\bullet-}$, if H_2O_2 exist in solution [30]. CVs in Fig. 4.8(C) show increased in current density with the existence of H_2O_2, which is corresponding to increase in second anodic ECL intensity. This result indicates reaction (i) - (iii) might happen simultaneously. By referring to the CVs of SPE in CBS with and without H_2O_2 in Fig. 4.8(A), we can confirmed that third oxidation peak at +0.78 V was due to oxidation of H_2O_2 to produce O_2. These results suggest that oxidation of H_2O_2 to O_2 involves generation of $HOO^{\bullet-}$ intermediate that dissociates to $O_2^{\bullet-}$, which subsequently react with $LH^{\bullet-}$ leading to the generation of 3-AP* [30]. Finally, the high ECL intensity was observed during reverse scan at oxygen reduction region, which suggest the O_2 produced during third oxidation peak were reduced to HOO^- and react with remaining $LH^{\bullet-}$ in solution to produce 3-AP* [10,16,17,31].

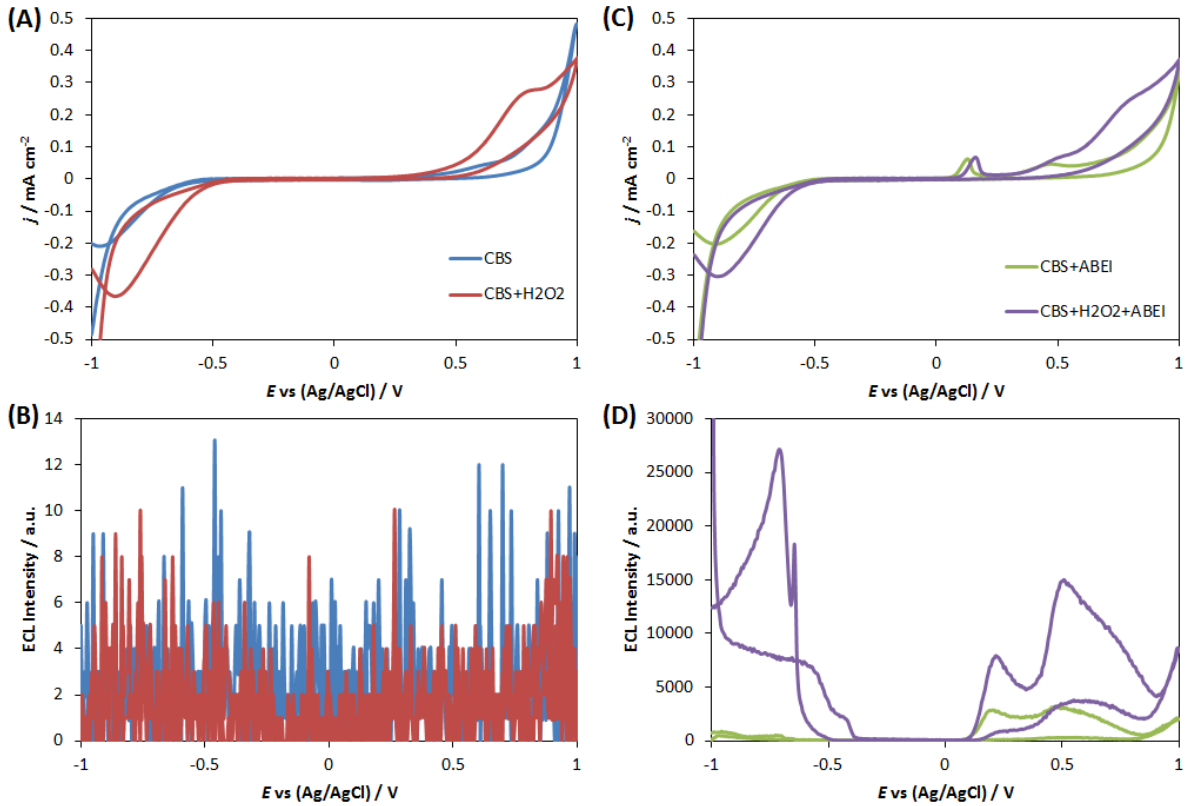

Figure 4.8: CVs and ECL intensities of SPE without (A & B) and with (C & D) 0.364 mM ABEI solution. Supporting electrolyte was 0.02 M CBS (pH 9.85) with and without 1 mM H_2O_2.

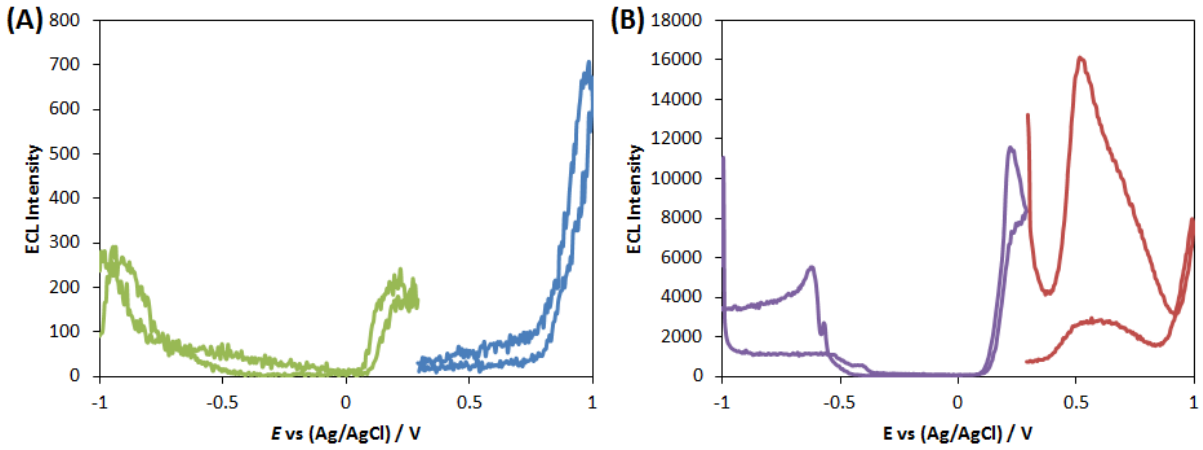

Figure 4.9: Potential dependent of ECL of ABEI solution on SPE (A) without and (B) with H_2O_2.

Similar CV and ECL intensity characteristic were observed on GONR/SPE in the same condition as depicted in Fig. 4.10. However, the first peak was shifting positively 35 mV might due to oxygen functional groups on GONR limiting the adsorption of ABEI on the electrode surface, hence reduce the ECL intensity. In contrast, the oxygen reduction peak of GONR/SPE shift negatively 100 mV compared to SPE expectedly contributed by oxygen functional groups that originally exist during GONR oxidative unzipping process, therefore speed up the reduction process and produce ECL emission.

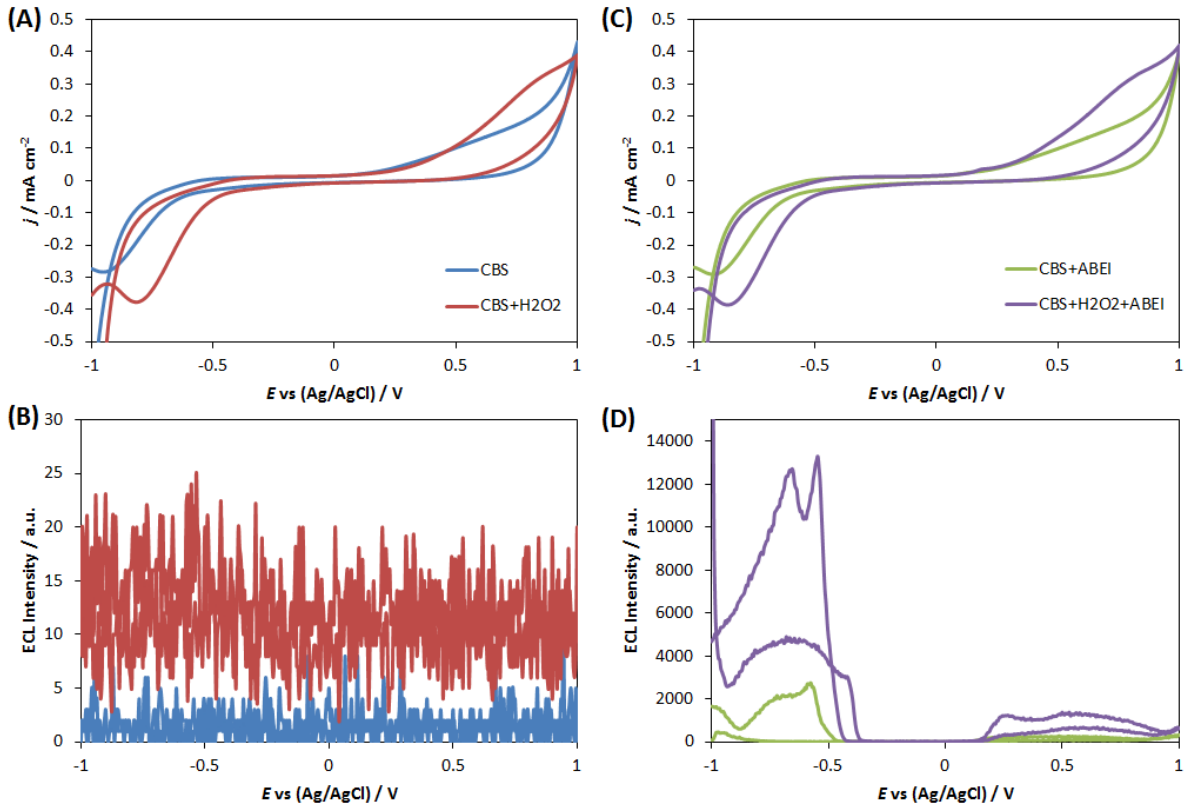

Figure 4.10: CVs and ECL intensities of GONR/SPE without (A & B) and with (C & D) 0.364 mM ABEI solution. Supporting electrolyte was 0.02 M CBS (pH 9.85) with and without 1 mM H_2O_2.

With the aim to confirm the presence of ABEI molecules on the as-prepared ABEI-AuNPs and its characteristic in ECL activity, the ABEI-AuNP/SPE was tested in blank CBS.

Fig. 4.7(C) shows CV of ABEI-AuNP/SPE only produce one oxidation peak at +0.655 V and one reduction peak at -0.824 V. With regard to CV, the ECL intensity spectrum also revealed one anodic ECL peak at +0.470 V with no cathodic ECL observed (Fig. 4.7(D)). This result confirmed that ABEI molecules exist together with AuNPs and capable to produce ECL activity. Previous report on ECL of luminol solution on Au electrode in alkaline conditions stated that oxidation of $LH^{\bullet-}$ by Au hydroxide ($Au(OH)_3$) is possible to yield anodic ECL at 0.5 V [10,16,17]. However, ABEI-AuNP/SPE in solid-liquid interface is not possible to generate anodic ECL through oxidation of $LH^{\bullet-}$ by $Au(OH)_3$ due to unlikely contact between Au surface and ABEI molecule. Although we believe CV oxidation peak refers to formation of gold oxide (Au_2O_3) but the anodic ECL might be generated between $LH^{\bullet-}$ and $O_2^{\bullet-}$ interaction through slow oxidation of LH^- and HOO^-, respectively. Positively shift anodic ECL peak of ABEI-AuNP/SPE in comparison to SPE in ABEI solution, suggested that ABEI-AuNP in solid-liquid interface has low catalytic activity towards ECL of ABEI. Since luminol oxidation is a rate determining step in ECL [15], low rates of ABEI oxidation reaction led to poor ECL emission. Moreover, due to ABEI-AuNP low catalytic activity, we believe direct electro-oxidation of $LH^{\bullet-}$ to 3-AP* is not possible as in ABEI in solution on SPE and GONR/SPE. Without H_2O_2 in solution, the CV (Fig. 4.11(A)) and ECL spectrum (Fig. 4.11(B)) showed identical characteristic, but both oxidation and anodic ECL peaks were shifted negatively with reduced current density and ECL intensity, respectively. The weak anodic ECL might produce from reaction $LH^{\bullet-}$ with dissolved O_2 [17].

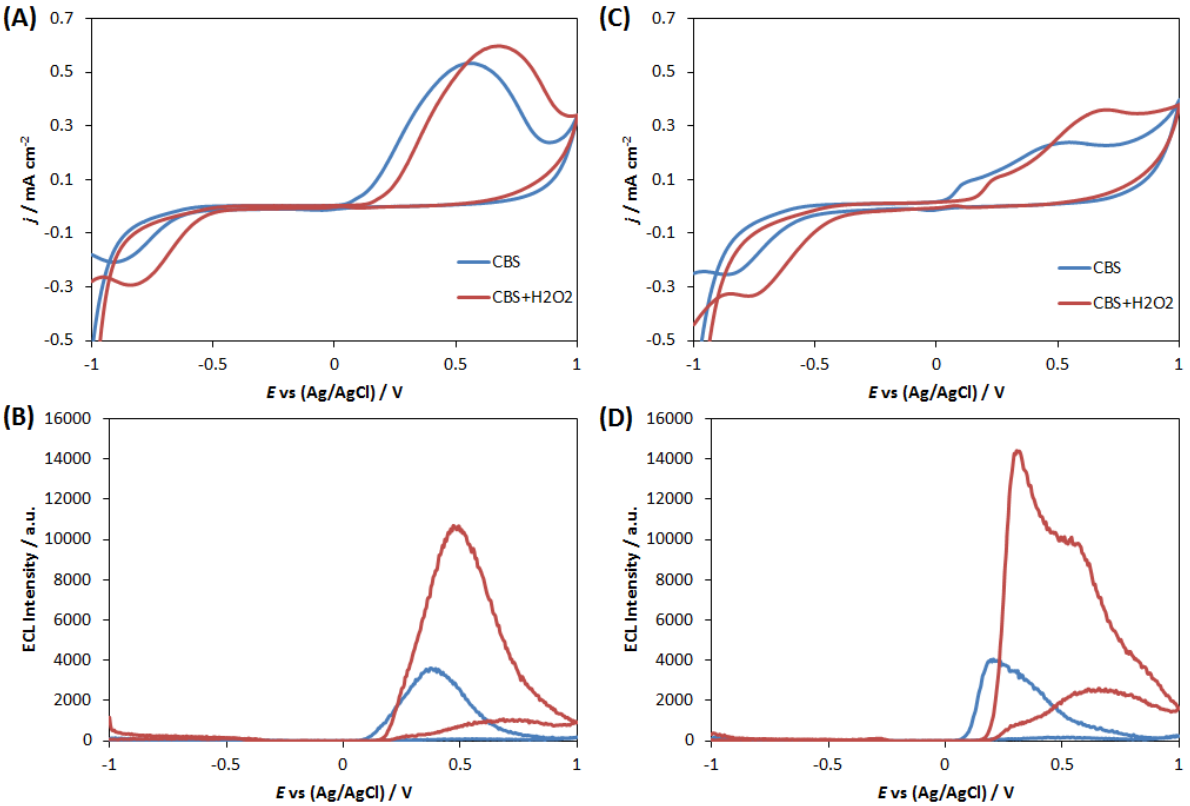

Figure 4.11: CVs and ECL intensities of ABEI-AuNP/SPE (A & B) and ABEI-AuNP-GONR/SPE (C & D). Supporting electrolyte was 0.02 M CBS (pH 9.85) with and without 1 mM H_2O_2.

Interestingly, by integrating as-prepared ABEI-AuNP with GONR to form ABEI-AuNP-GONR/SPE, CV revealed two oxidation peaks at +0.235 and +0.641 V with one reduction peak at -0.746 V as in Fig. 4.7(C). In correlation to CV, the ECL intensity spectrum also showed two anodic ECL peaks at +0.305 and +0.570 V with no appearance of cathodic ECL peak (Fig. 4.7(D)). CVs of ABEI-AuNP-GONR/SPE in CBS with and without addition of H_2O_2 (Fig. 4.11(C)) exhibit similar characteristic, but positively shift oxidation potentials and increase current density with existence of H_2O_2. The corresponding ECL spectra demonstrate that the first anodic ECL peak was decreased significantly while the second anodic ECL peak was diminished without the existence of H_2O_2. Based on these results, we believed the first oxidation peak is due to LH^- to $LH^{\bullet-}$ that react with $O_2^{\bullet-}$ to form 3-AP*.

The $O_2^{\bullet-}$ might be generated through hydroxyl radical ($OH^{\bullet}$) from broken O-O bond of H_2O_2 with HOO^- or reaction between $LH^{\bullet-}$ with dissolved O_2 [14]. On the other hand, a brief shoulder of second anodic ECL peak was attributed by oxidation of HOO^- to produce $O_2^{\bullet-}$ and interact with remaining $LH^{\bullet-}$ to emit light. The oxidation peak of H_2O_2 on ABEI-AuNPs is expected to be later than bare Au electrode as in Fig. 4.12. Similar to ABEI-AuNP/SPE, we believe the second oxidation peak of ABEI-AuNP-GONR/SPE was due to oxidation of Au to Au_2OH_3. In comparison to ABEI-AuNP/SPE, ABEI-AuNP with the support from GONR produce 30.0% increment in ECL intensity at much early potential suggesting enhanced in catalytic activity. The catalytic enhancement might due to increment in AuNP active surface area that facilitates the oxidative radical generation and faster reaction kinetics on luminol oxidation process. Furthermore, GONR has identified to act as backbone with ABEI-AuNP to avoid aggregation as observed in Fig. 4.5. Moreover, hybrid of ABEI-AuNP and GONR might form three-dimensional specific non-covalent interaction between oxygenated functional groups of GONR and AuNPs active sites, which consequently enhanced the catalytic performance of the whole system.

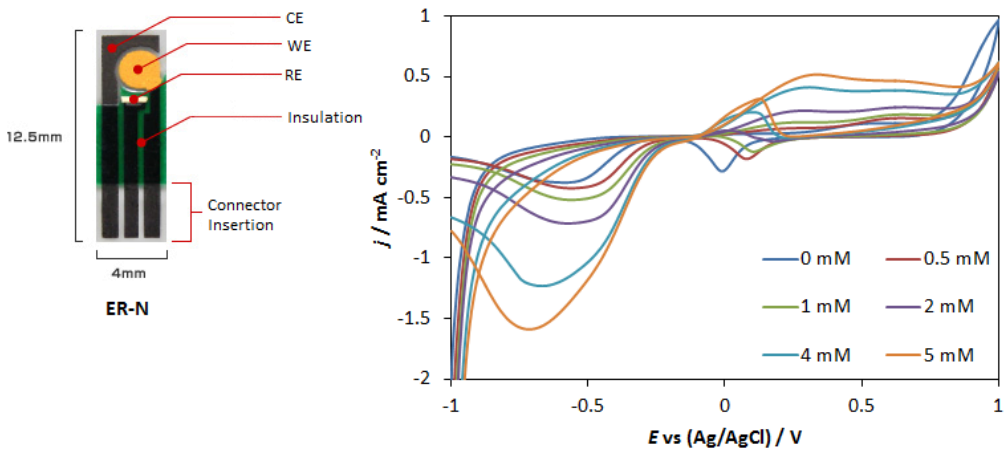

Figure 4.12: H_2O_2 oxidation peak on bare gold electrode.

ECL spectra of ABEI in solution on SPE demonstrate the high cathodic ECL intensity (Fig. 4.7 (B)) while ABEI-AuNP on modified SPE shows none (Fig. 4.7 (D)). To understand this phenomenon, we used a CCD camera to record ECL activity on each electrode. Fig. 4.13 (A) shows SPE in ABEI solution produce high ECL emission at the working electrode during forward scan while counter electrode produce ECL emission during reverse scan. In contrast, ABEI-AuNP/SPE only produces ECL emission at the working electrode during forward scan (Fig. 4.13 (B)). In electrochemical system, working electrode behave as anode while counter electrode behave as the cathode during forward scan and vice versa during reverse scan. These results explained that ECL emission only happened on anode as being proven by ABEI in solution on SPE electrode. Since ABEI-AuNP only cast on the working electrode of SPE, hence no ECL emission was observed during reverse scan. Leading up to this point, we have so far proven that GONRs play a very important role as a functional supporting matrix in enhancing the catalytic activity of ABEI-AuNPs in the luminol oxidation reaction, and also act as a backbone to prevent the aggregation of ABEI-AuNPs. To achieve a better performance of the ABEI-AuNP-GONR/SPE, we carried out further optimization studies on loading ratio between GONR and ABEI-AuNP and as described in the following section.

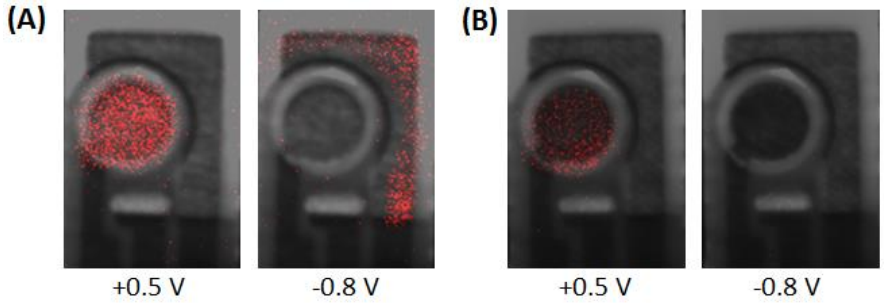

Fig. 4.13: CCD images of ECL intensity at different potentials on (A) SPE in 0.364 mM ABEI solution and (B) ABEI-AuNP/SPE. Supporting electrolyte was 1 mM H_2O_2 in 0.02 M CBS (pH 9.85).

4.3.3 Effect of loading ratio on ECL of ABEI-AuNP-GONR/SPE

In the previous section, GONRs have proven to be a good supporting matrix on ABEI-AuNPs in enhancing its catalytic activity and also avoiding aggregation of particles through electrostatic interaction between AuNP and carboxyl groups on GONR. However, the loading ratio between ABEI-AuNP and GONR need to be controlled in order to avoid aggregation from high concentration of ABEI-AuNP and thick oxygen barrier from high concentration of GONR. Therefore, we optimized the ratio of GONR and ABEI-AuNP loadings to achieve an optimum binding between ABEI-AuNPs and the GONR supporting matrix while controlling the size of the AuNPs in the ABEI-AuNP-GONR/SPE. The optimized loading ratio was determined from the maximum measured ECL intensity of the anodic ECL peak in 0.02 M CBS with the addition of 1 mM H_2O_2. Furthermore, the higher ECL intensity of the ABEI-AuNP-GONR/SPE is attributed to the increased AuNP surface area [18] along with the greater number of active sites [24]. To prove this suggestion, we examined the surface area of each catalytic material modified on SPE based on the optimum loading ratio of optimum ABEI-AuNP-GONR/SPE in 10 mM ferricyanide at various scan rates. Subsequently, the active surface area was calculated using Randles-Sevcik equation [19].

Fig. 4.14 shows the loading ratio between as-prepared ABEI-AuNPs and GONR (1 mg/mL in DI water). The ECL intensity was significantly increased by increasing the GONR ratio from 0% to 25% and reducing the amount of ABEI-AuNPs from 100% to 75%. A further decrease of ABEI-AuNP loading to 50% and 50% of GONR show strong inhibition of ECL intensity. The low loading of GONR yield high ECL intensity might due to less aggregation of ABEI-AuNP on SPE and expected to increase the active surface area on the electrode. In the case of high loading of GONR with low loading of ABEI-AuNP, the reduction in ECL intensity was mainly caused by low amounts of ABEI exist on the electrode. Moreover, high loading of GONR

lead to a high amount of oxygen functional groups present on the electrode, which form an oxide layer that act as barriers in the electron-transfer process, thus lowering the oxidation rates of ABEI [28]. From this experiment, loading ratio of 75% ABEI-AuNPs to 25% GONR was chosen as the optimum loading ratio to be applied in other experiments.

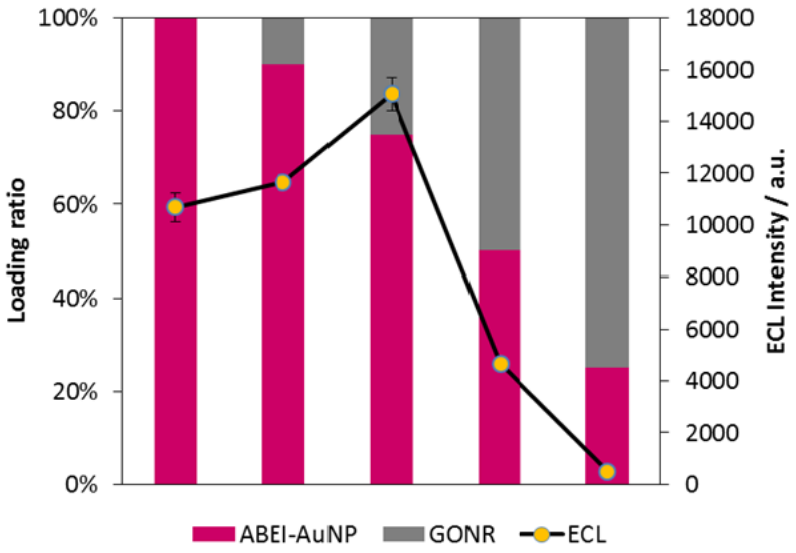

Figure 4.14: ECL intensity on various loading ratio of ABEI-AuNP and GONR. Electrolyte was 1 mM H_2O_2 in 0.02 M CBS (pH 9.85).

Based on the optimum ABEI-amp-GONR/SPE, the contribution of each catalytic material ratio towards the active surface area and ECL intensity were compared. Fig. 4.15 shows the increment in the active surface area by modifying SPE electrode with GONR material. The reduction in GONR loading (1 mg/mL) by 4x dilution in water before casting on working electrode resulted in 21.7% increase of active surface area. This phenomenon might relate to improve in electron-transfer due to less oxide ions that insulate the electrode surface. In the case of ABEI-AuNP, 25% loading reduction than as-prepared ABEI-AuNP on modified SPE lead to 48.8% increment in the active surface area but decrease in ECL intensity by 53.7%. These results suggest that higher loading of ABEI-AuNP promote high

aggregation on the electrode surface. It is expected that by lowering the loading of ABEI-AuNP will caused reduction of ECL intensity due to low amount of ABEI molecule exist on the electrode. Interestingly, composite of 25% GONR and 75% ABEI-AuNP lead to 34.9% and 97.8% increment in the total active surface area and ECL intensity, respectively. Leading up to this point, we have so far proven that GONRs play a very important role as a functional supporting matrix in enhancing the catalytic activity of ABEI-AuNPs in the ECL reaction, and also act as a backbone to prevent the aggregation of AuNPs. The high catalytic activity of ABEI-AuNPs might lead to active generation of oxidative radicals, which subsequently enhanced the ECL intensity. The following section will discussed the influenced of buffer pH, H_2O_2 concentration and dissolved O_2 in ECL reaction to further elucidate the mechanism of ABEI-AuNP-GONR/SPE in solid-liquid interface.

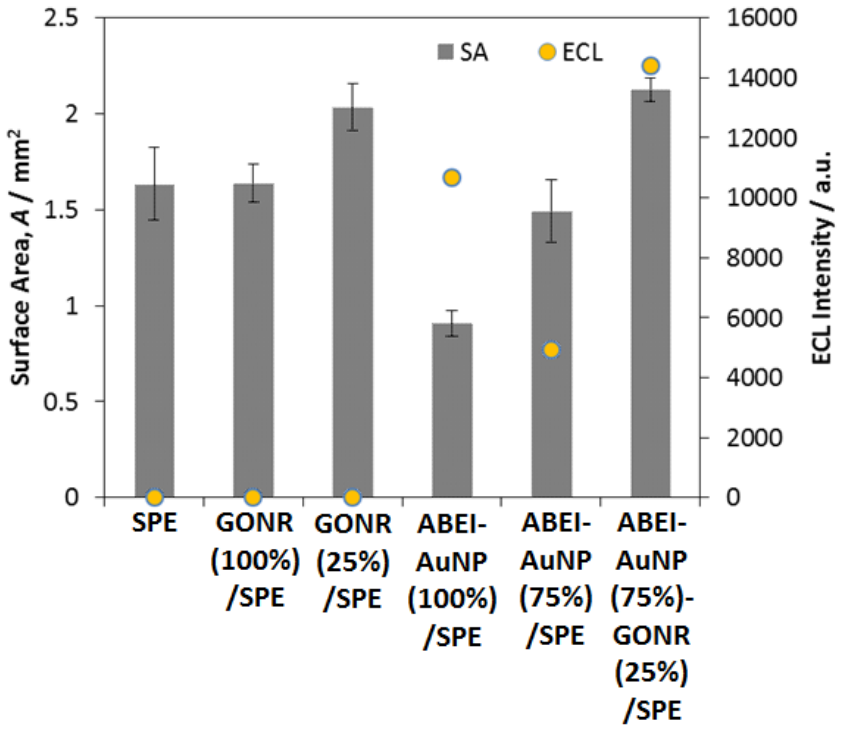

Figure 4.15: Comparison of anodic ECL peak and calculated active surface area on each ratio of catalytic materials. The electrolytes were 1mM H_2O_2 in 0.02 M CBS (pH 9.85) and 10 mM $K_3[Fe(CN)_6]$ in 1 M KCl for measurement of ECL intensity and active surface area, respectively.

4.3.4 Effect of pH, H_2O_2 concentration and dissolved O_2 on ECL of ABEI-AuNP-GONR/SPE

The effect of pH on ECL of ABEI-AuNP-GONR/SPE was determined using CBS for pH in the range of 9.02 to 10.72 as shown in Fig. 4.16. The ECL intensity increases significantly with increasing pH value and achieved its maximum at pH 10.02. Moreover, the enormous increment in ECL intensity with addition of 1 mM H_2O_2 at increasing pH value might suggest enhancements in oxidative species generation, such as $OH^{\bullet}$ and $O_2^{\bullet-}$, which were necessary in conversion of $LH^{\bullet-}$ to 3-AP* [10]. Furthermore, presence of ABEI-AuNP catalyst facilitate the generation of epoxidation reaction on Au surface with H_2O_2 via O-O bond. The catalysis of AuNP might break up the O-O bond to form $OH^{\bullet}$ that consequently interact with HOO^- to form $O_2^{\bullet-}$ [29]. In addition, basic solution also important in preparing LH^- and HOO^- precursor for further electrochemical oxidization to produce $LH^{\bullet-}$ and $O_2^{\bullet-}$ radicals. However, at very high pH, a decrease in ECL intensity was observed might due to high formation of hydroxide ions (OH^-) on electrode surface that interfere with H_2O_2 dissociation on AuNP surface, therefore reduce the $O_2^{\bullet-}$ generation. In the case of ABEI-AuNP-GONR/SPE tested in various pH of CBS without the addition of H_2O_2, ECL intensity demonstrates small increment due to ECL mainly generated through interaction between $LH^{\bullet-}$ and dissolved O_2 to produce 3-AP*. On the other hand, CV of ABEI-AuNP-GONR/SPE in neutral conditions (data not included) shows luminol oxidation reaction start at 0.48 V and produce very low ECL intensity, where the peak shift positively 150 mV compare to ABEI-AuNP-GONR/SPE tested in alkaline condition. These results indicate that neutral pH provides insufficient amount of oxidative radical to produce appreciable amounts of $LH^{\bullet-}$ and $O_2^{\bullet-}$, which lead to very slow luminol oxidation reaction and consequently low 3-AP* [7]. So far, we have known the generation of $O_2^{\bullet-}$ in the presence of H_2O_2 play important role in producing intense ECL emission.

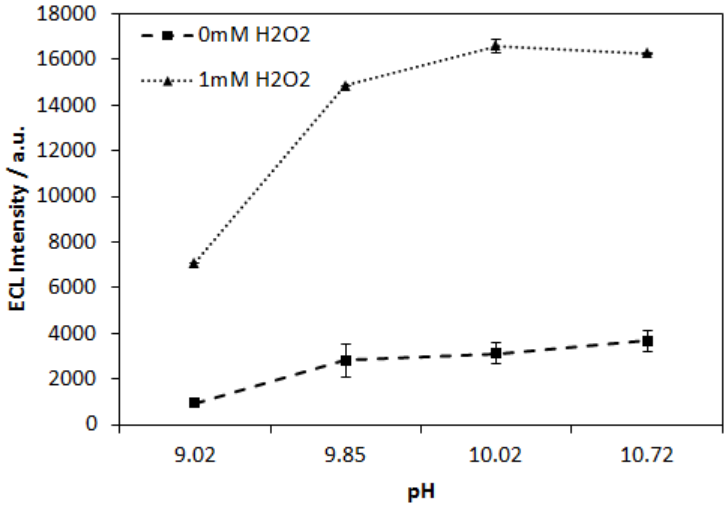

Figure 4.16: ECL intensity of ABEI-AuNP-GONR/SPE in relation to pH of buffer solution with and without the presence of 1 mM H_2O_2.

H_2O_2 plays an important role in ECL of luminol in facilitating oxidative radical formation in order to produce 3-AP* excited state as discussed in the previous section. Fig. 4.17(A) shows that ECL intensity increase significantly with increasing concentration of H_2O_2 and the second peak become more obvious. Moreover, the ECL peak intensity shifts positively with increasing H_2O_2 concentration. Above results suggest that H_2O_2 provide the generation of $O_2^{\bullet-}$ radicals through oxidation of HOO^- and facilitate $OH^\bullet$ formation on ABEI-AuNP surface simultaneously through epoxidation reaction. However, this process led to competition between radicals to absorb on the electrode surface, resulted in positively shift anodic ECL peak. With low concentration of H_2O_2, most HOO^- formed $O_2^{\bullet-}$ radicals through reaction with $OH^\bullet$ and consumed to generate first ECL peak with $LH^{\bullet-}$. We can assume that HOO^- involve in second ECL peak increase with higher H_2O_2 concentration through electrochemical oxidization of remaining HOO^- to $O_2^{\bullet-}$ and subsequently react with $LH^{\bullet-}$ in generating 3-AP* for second anodic ECL peak. Apart from that, we also can observe high

ECL intensity without addition of H_2O_2. This phenomenon might suggest that ECL of ABEI might be generated from $LH^{\bullet-}$ with dissolved O_2 in basic conditions. Therefore, a thorough study was done on ABEI-AuNP-GONR/SPE in deaerated CBS, which was purge with nitrogen gas (N_2) for 30 minutes before test. Fig. 4.17(B) shows that ECL intensity increase with increase of H_2O_2 concentration in deaerated CBS. However, the ECL intensity recorded was lower compare to ECL intensity in normal CBS containing dissolved O_2. This result further confirms that dissolve O_2 also give minor contribution to $O_2^{\bullet-}$ generation through $LH^{\bullet-}$ for ECL emission. Moreover, ECL intensity still can be detected on ABEI-AuNP-GONR/SPE in deaerated CBS without addition of H_2O_2. This result suggests that $LH^{\bullet-}$ can be converted into 3-AP* through direct electro-oxidation in the absence of O_2 and HOO^- [11]. Without dissolved O_2, the second ECL peak was not observed at low concentration of H_2O_2.

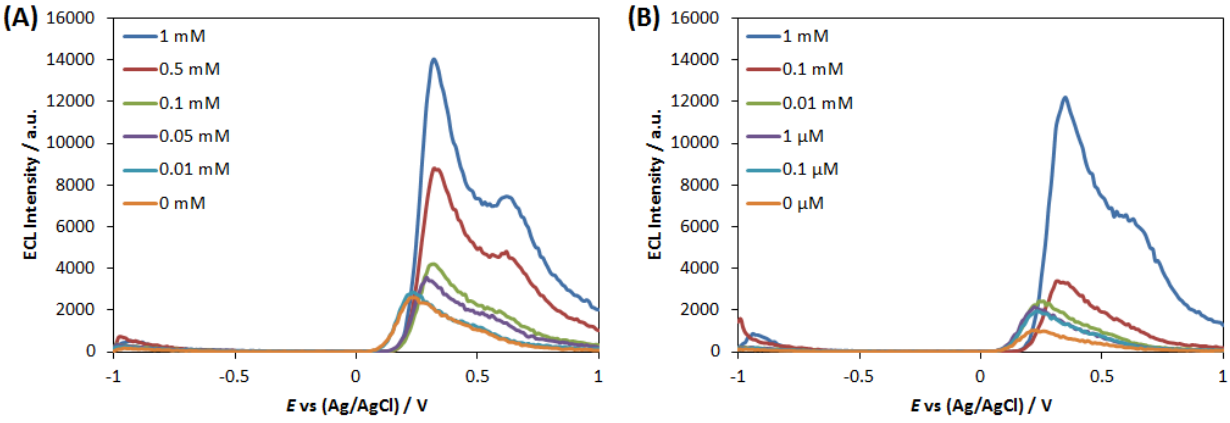

Fig. 4.17: ECL intensity of ABEI-AuNP-GONR/SPE in (A) CBS and (B) deaerated CBS (pH 9.85) with various concentrations of H_2O_2. The scan rate was 100 mV/s.

In conclusion, the pH of buffer, H_2O_2 concentration and dissolved O_2 are contributed to formation of oxidative radical, mainly $O_2^{\bullet-}$, which is a strong co-oxidant for $LH^{\bullet-}$ in generating ECL. In addition, the generation of radicals also depends on catalysis of ABEI-

AuNP that enhanced significantly with GONR supporting matrix. The possible mechanism of ABEI-AuNP-GONR/SPE in generating ECL on ABEI-AuNP-GONR/SPE was proposed in the next section.

4.3.5 Propose ECL mechanism of ABEI-AuNP-GONR/SPE

ECL of ABEI-AuNP-GONR/SPE revealed two anodic ECL peaks. Experimental results show first anodic ECL peak is highly dependent on pH, H_2O_2 concentration and catalysis of ABEI-AuNP. Inspection of ABEI-AuNP-GONR/SPE ECL under nitrogen atmosphere without addition H_2O_2 show weak emission of ECL proving that $LH^{\bullet-}$ can undergo direct electro-oxidation to 3-AP* in the absence of $O_2^{\bullet-}$ as in eq. (1). Otherwise, $LH^{\bullet-}$ is expected to interact with $O_2^{\bullet-}$ to produce 3-AP* as in eq. (4) – (6). The generation of $O_2^{\bullet-}$ may resulted either from interaction between HOO^- with $OH^{\bullet}$ from H_2O_2 epoxidation reaction by the virtue of the AuNP catalysis as in eq. (2) or direct reaction between $LH^{\bullet-}$ with dissolved O_2 that naturally exist in solution as in eq. (3).

$$LH^- - e^- \rightarrow LH^{\cdot -} + H^+ \rightarrow\rightarrow 3-AP^* \ (1)$$

$$HOO^- + OH^{\cdot} \rightarrow O_2^{\cdot -} + H_2O \ (2)$$

$$LH^{\cdot -} + O_2 \rightarrow O_2^{\cdot -} + L \ (3)$$

$$LH^{\cdot -} + O_2^{\cdot -} \rightarrow LOO^- \ (4)$$

$$LOO^- \rightarrow 3-AP^* + N_2 \ (5)$$

$$3-AP^* \rightarrow 3-AP + h\nu \ (6)$$

On the other hand, the second anodic ECL mainly contributes by high concentration of H_2O_2 as being confirmed in both deaerated and non-deaerated CBS. The emission of light was predicted due to interaction between $LH^{\bullet-}$ with $O_2^{\bullet-}$, which produced through

electrochemical oxidation of HOO^- based on the peak position of second anodic ECL in between oxidation peak of H_2O_2 to O_2 on gold electrode and GONR/SPE.

$$HOO^- - e^- \rightarrow HOO^{\cdot -} \leftrightarrow O_2^{\cdot -} \ (7)$$

$$LH^{\cdot -} + O_2^{\cdot -} \rightarrow LOO^- \ (4)$$

$$LOO^- \rightarrow 3 - AP^* + N_2 \ (5)$$

$$3 - AP^* \rightarrow 3 - AP + h\nu \ (6)$$

4.3.6 Characterization interaction between ABEI-AuNP and GONR

To further clarify the interaction between ABEI-AuNP and GONR, ATR-FTIR spectra of each catalytic material were gathered. We prepared 1 mL of GONR and ABEI-AuNP solutions in DI water based on the ratio used for ABEI-AuNP-GONR solution. These solutions were centrifuged to remove DI water. Then, 0.5 mL of ethanol was added and sonicated to produce a well-dispersed catalyst solution. Immediately after that, a small amount of catalyst was casted on the ATR diamond surface to form a thin layer. The FTIR spectra in Fig. 4.18 show common peaks at around 2300 cm^{-1}, which are attributed to the asymmetric stretching vibration of CO_2, while the noise signal in the regions 3400–4000 cm^{-1} and 1300–1900 cm^{-1} are derived from water vapor [29]. Apart from those signals, the GONR spectrum showed a strong hydroxyl band at approximately 3200 cm^{-1} (i) of COO–H/O–H stretching, in addition to four carbonyl bands at around 1700 cm^{-1} (iii) of C=O stretching, around 1564 cm^{-1} (iv) of –COO– asymmetric stretching, around 1030 cm^{-1} (vii) of C–O stretching and around 1209 cm^{-1} (viii) of O–H deformation [19, 29].

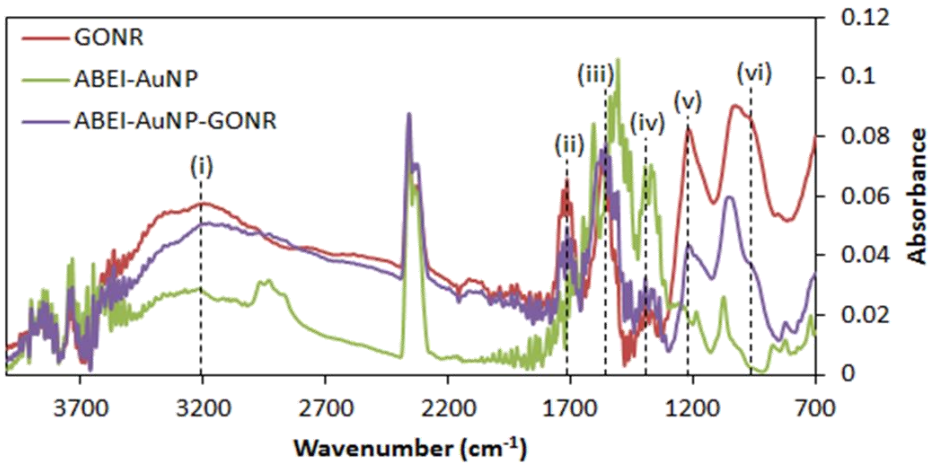

Fig. 4.18: ATR-FTIR spectra of ABEI-AuNP and GONR precursor to form ABEI-AuNP-GONR mixture.

The appearance of hydroxyl and carbonyl bands indicates that the GONR had successfully undergone oxidative unzipping process. In comparison, ABEI-AuNP spectrum revealed a broad peak at 3400 cm^{-1}signifying weak covalent interaction between the amino group in ABEI and AuNPs [24]. Moreover, ABEI-AuNP spectrum shows strong aromatic C=C bending at 1500 cm^{-1} (v) with two alkanes band at around 2900 cm^{-1} (ii) of C–H stretching and around 1390 cm^{-1} (vi) of C–H deformation. Interestingly, mixture of ABEI-AuNP-GONR show a decrease of absorbance intensity for hydroxyl and carbonyl bands of GONR indicating ABEI-AuNP formed metal-oxygen bonding with GONR that enhanced its catalytic performance. In addition, the disappearance of the aromatic band in ABEI-AuNP after mixing with GONR might suggest non-covalent interaction between benzene ring of ABEI with benzene domain of GONR.

4.3.7 Application in biosensors

ECL enzyme biosensors (also called enzyme-based ECL biosensors) offer selective, sensitive detection of analytes. Enhancement in the ECL intensity of ABEI-AuNP-GONR/SPE with

addition of H_2O_2 was observed in Fig. 4.16 and Fig. 4.17; indicate the possible application in enzymatic glucose sensor. This is due to glucose oxidase enzyme catalyzes glucose oxidation to gluconolactone that produce H_2O_2 as shown in Fig. 4.19. Figure 4.20 shows the increment in ECL intensity proportional to increasing glucose concentration. Linear calibration curve was obtained from 1 to 250 µM, show that ABEI-AuNP-GONR/SPE is very sensitive in glucose detection at low detection range. The lowest detection limit is 1 µM.

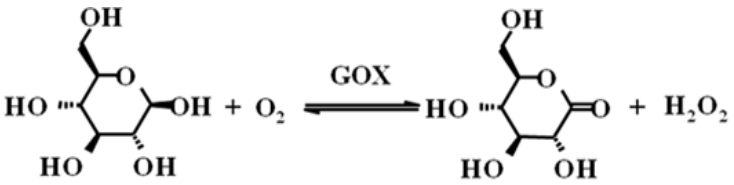

Figure 4.19: Enzymatic glucose oxidation reaction.

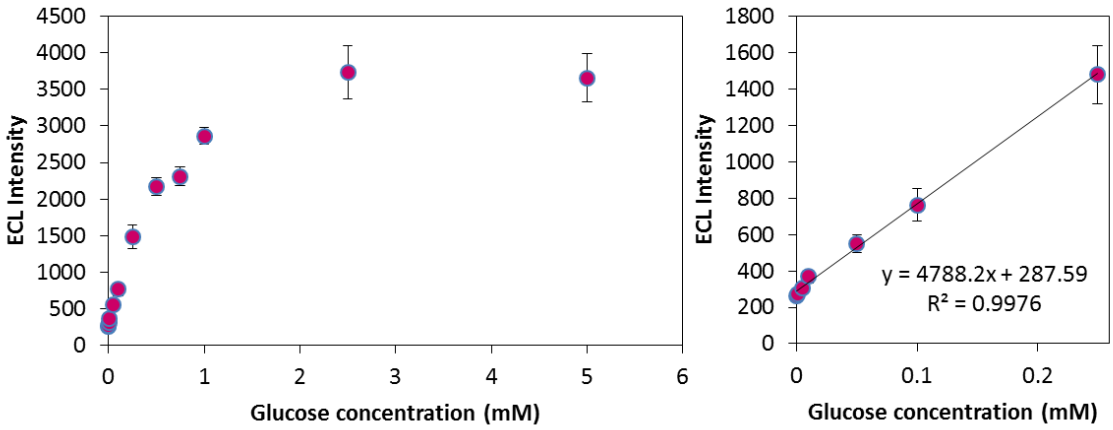

Figure 4.20: Calibration curve based on recorded ECL intensity on ABEI-AuNP-GONR/SPE in various concentrations of glucose. The supporting electrolyte was CBS (pH 9.85).

ABEI-AuNP-GONR/SPE in blood serum show no inhibition of ECL intensity as observed in Figure 4.21. The glucose concentration in blood serum was determined by using microplate reader. ECL intensity also observed in the absence of serum might due to pH buffer effect.

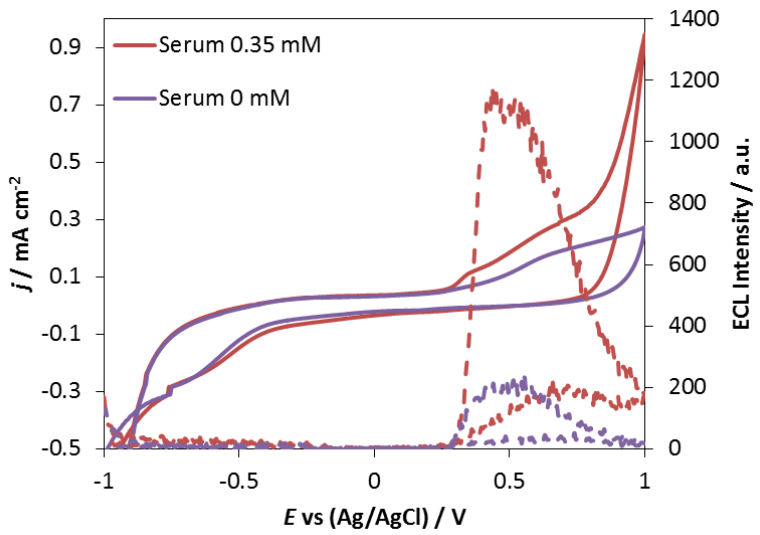

Figure 4.21: CV (solid lines) and ECL intensity (dotted lines) of ABEI-AuNP-GONR/SPE in blood serum containing 0.35 mM glucose.

ABEI-AuNP-GONR/SPE also sensitive to pH change as observed in Figure 4.16. Herein, for the first time we develop urea biosensor by utilizing urease enzyme to produce ammonia. As a consequence, ammonia will change the pH of solution based on urea concentration.

$$NH_2CONH_2 + H_2O \xrightarrow{\text{Urease}} 2NH_3 + CO_2$$

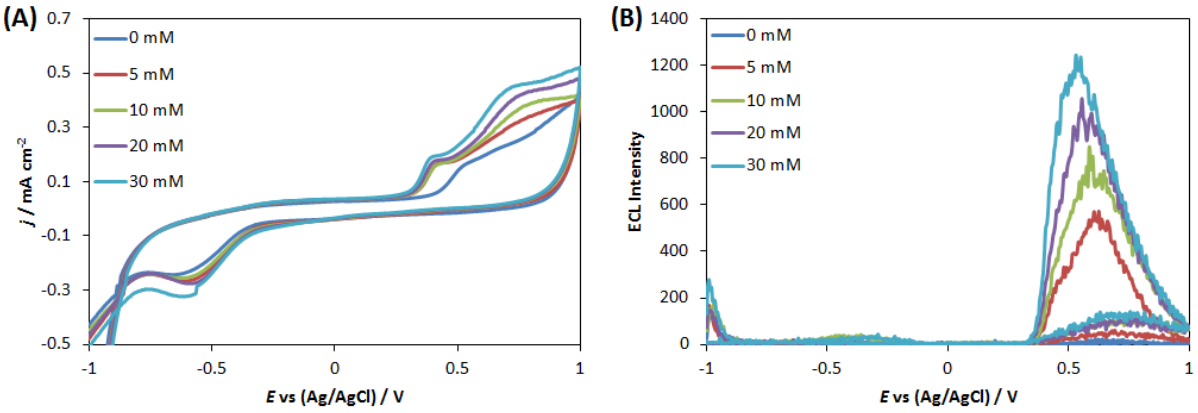

Figure 4.22: (A) CV and (ECL intensity of ABEI-AuNP-GONR/SPE in various concentrations of urea. The supporting electrolyte was PBS (pH 7.0). Scan rate was 50 mV/s.

CVs in Figure 4.22(A) demonstrate the increment in urea concentration lead to negatively shift in ABEI oxidation peak and increase in ECL intensity (Figure 4.22(B)). Furthermore, calibration curve in Figure 4.23 proved that ECL intensity correlate with the change in pH. These results suggest that the reaction kinetics of ABEI oxidation reaction and oxidative radical generation are improved with increment in pH solution, leading to negatively shift ABEI oxidation potential and anodic ECL.

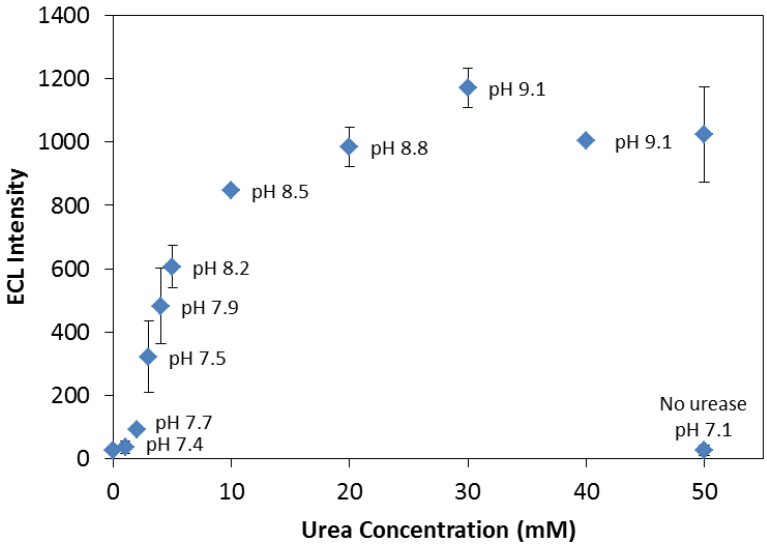

Figure 4.23: Calibration curve based on recorded ECL intensity on ABEI-AuNP-GONR/SPE in various concentrations of urea. The supporting electrolyte was PBS (pH 7.0).

4.4 Conclusions

In summary, we have synthesized and optimized a hybrid of ABEI-AuNPs with GONRs, through simple mixing and deposition on carbon SPE. The catalytic activity of ABEI-AuNP-GONR/SPE towards ECL of luminol oxidation reaction has been studied and compared to that of ABEI-AuNP/SPE in alkaline conditions. The intercalation of ABEI-AuNPs with GONRs resulted in 30.0% increment in ECL intensity due to 80.2% increase in active surface area compared with ABEI-AuNP/SPE. However, different characteristics of CV data were

revealed for both electrodes that showing slow reaction kinetics towards luminol oxidation of ABEI-AuNP without support GONR, but produce 50.1% higher peak current density. These results suggest that high ECL emission from ABEI-AuNP-GONR/SPE might due to interaction between electrochemical generated luminol radicals and oxidative radicals, which independently generated by the virtue of ABEI-AuNP catalysis. Consequently, GONRs have been identified to act as a backbone with ABEI-AuNP to keep from aggregation through non-covalent interactions and metal-oxygen bonding between oxygen functional groups on GONR with ABEI-AuNP active sites enhances the catalytic performance. Possible application of ABEI-AuNP-GONR/SPE in enzymatic electrochemical biosensor display good sensitivity and selectivity. The utilization of SPE can pave the way for future developments of portable and rapid point of care device.

4.5 References

[1] M.M. Richter, Electrochemiluminescence (ECL), *Chem. Rev.* **104** (2004) 3003.

[2] Y. Su, Y. Lv, Graphene and graphene oxide: recent advances in chemiluminescence and electrochemiluminescence, *RSC Adv.* **4** (2014) 29324.

[3] W. Miao, Electrogenerated chemiluminescence and its biorelated applications, *Chem. Rev.* **108** (2008) 2506.

[4] A.J. Bard, in *Electrogenerated Chemiluminescence*, ed. A.J. Bard, Marcel Dekker, Inc., 10th edn. (2004), ch. 1, pp 1–22.

[5] G. Merényi, J. Lind, T.E. Eriksen, Luminol chemiluminescence: Chemistry, Exitation, Emitter, *J. of Bioluminescence and Chemiluminescence* **5** (1990) 53.

[6] G. Merényi, J.S. Lind, Role of peroxide intermediate in the chemiluminescence of luminol. A mechanistic study, *J. Am. Chem. Soc.* **102** (1980) 5830.

[7] S. Sakura, Electrochemiluminescence of hydrogen peroxide-luminol at a carbon

electrode, *Analytica Chimica Acta* **262** (1992) 49.

[8] P.M. Easton, A.C. Simmonds, A. Rakishev, A.M. Egorov and L.P. Candeias, Quantitative model of the enhancement of peroxidase-induced luminol luminescence, *J. Am. Chem. Soc.* **118** (1996) 6619.

[9] A.N. Diaz, F.G. Sanchez and J.A.G. Garcia, Hydrogen peroxide assay by using enhanced chemiluminescence of the luminol-H_2O_2-horseradish peroxidase system: comparative studies, *Analytica Chimica Acta* **327** (1996) 161.

[10] S. Sakura and H. Imai, Determination of Sub-nmol Hydrogen Peroxide by Electrochemiluminescence of Luminol in Aqueous Solution, *Anal. Sci.* **4** (1988) 9.

[11] H. Cui, Z.F. Zhang, G.Z. Zou and X.Q. Lin, Potential-dependent electrochemiluminescence of luminol in alkaline solution at a gold electrode, *Journal of Electroanalytical Chemistry* **566** (2004) 305.

[12] X. Chen, B. Su, X. Song, Q. Chen, X. Chen, X. Wang, Recent advances in electrochemiluminescent enzyme biosensors, *Trends in Analytical Chemistry* **30** (2011) 665.

[13] G.P. Jirka, A.F. Martin and T.A. Nieman, pH and concentration response surfaces for the luminol-H_2O_2 electrogenerated chemiluminescence reaction, *Analytica Chimica Acta* **284** (1993) 345.

[14] D. Strmcnik, K. Kodama, D. van der Vliet, J. Greeley, V. R. Stamenkovic, N. M. Markovic, The role of non-covalent interactions in electrocatalytic fuel-cell reactions on platinum, *Nat. Chem.* **1** (2009) 466.

[15] Z.F. Zhang, H. Cui, C.Z. Lai and L.J. Liu, Gold nanoparticle-catalyzed luminol chemiluminescence and its analytical application, *Anal. Chem.* **77** (2005) 3324.

[16] Y.P. Dong, H. Cui, and Y. Xu, Comparative studies on electrogenerated chemiluminescence of luminol on gold nanoparticle modified electrodes, *Langmuir* **23** (2007) 523.

[17] H. Cui, Y. Xu and Z.F. Zhang, Multichannel electrochemiluminescence of luminol in neutral and alkaline aqueous solutions on a gold nanoparticle self-assembled electrode, *Anal. Chem.* **76** (2004) 4002.

[18] H. Cui, W. Wang, C.F. Duan, Y.P. Dong and J.Z. Guo, Synthesis, characterization, and electrochemiluminescence of luminol-reduced gold nanoparticles and their application in a hydrogen peroxide sensor, *Chem. Eur. J.* **13** (2007) 6975.

[19] N.S. Ismail, Q.H. Le, H. Yoshikawa, M. Saito and E. Tamiya, Development of non-enzymatic electrochemical glucose sensor based on gonr-gold nanoparticle hybrid, *Electrochimica Acta* **146** (2014) 98.

[20] A.K. Geim and K.S. Novoselov, The rise of graphene, *Nat. Mater.* **6** (2007) 183.

[21] D.V. Kosynkin, A.L. Higginbotham, A. Sinitskii, J.R. Lomeda, A. Dimiev, B.K. Price and J.M. Tour, Longitudinal unzipping of carbon nanotunes to form graphene nanoribbons, *Nature* **458** (2009) 872.

[22] A.L. Hogginbotham, D.V. Kosynkin, A. Sinitskii, Z. Sun and J.M. Tour, Lower-defect graphene oxide nanoribbons from multiwalled carbon nanotubes, *ACS Nano* **4** (2010) 2059.

[23] K. Idegami, M. Chikae, N. Nagatani, E. Tamiya, Y. Takamura, Fabrication and characterization of planar screen-printed Ag/AgCl reference electrode for disposable sensor strip, *Japanese Journal of Applied Physics* **49** (2010) 097003.

[24] D. Tian, H. Zhang, Y. Chai and H. Cui, Synthesis of *N*-(aminobutyl)-*N*-(ethylisoluminol) functionalized gold nanomaterials for chemiluminescence for chemiluminescence bio-probe, *Chem. Commun.* **47** (2011) 4959.

[25] W. Shen, D. Tian, H. Cui, D. Yang and Z. Bian, Nanoparticle-based electrochemiluminescence immunosensor with enhanced sensitivity for cardiac troponin I using *N*-(aminobutyl)-*N*-(ethylisoluminol) functionalized gold nanoparticles as labels, *Biosensors and Bioelectronics* **27** (2011) 18.

[26] W. Wang, T. Xiong, H. Cui, Fluorescence and electrochemiluminescence of luminol-reduced gold nanoparticles: photostability and platform effect, *Langmuir* **24** (2008) 2826.

[27] http://www.biodevicetech.com/products/depchip/dep_ep.shtml (accessed January 2014).

[28] http://www.biodevicetech.com/BDTminiSTATleaf100707.pdf, (accessed January 2014).

[29] L.Q. Hoa, M.C. Vestergaard, H. Yoshikawa, M. Saito and E. Tamiya, Enhancing catalytic performance of Pt-based electrode with a noncovalent interaction-induced functionalized carbon nanotube-grafted matrix, *J. Mater. Chem.* **22** (2012) 14705.

[30] K.E. Haapakka and J.J. Kankare, The mechanism of the electrogenerated chemiluminescence of luminol in aqueous alkaline solution, *Analytica Chimica Acta* **138** (1982) 263.

[31] H. Cui, G.Z. Zou and X.Q. Lin, Electrochemiluminescence of luminol in alkaline solution at a paraffin-impregnated graphite electrode, *Anal. Chem.* **75** (2003) 324.

CHAPTER 5

SUMMARY & FUTURE REMARKS

5.1 Summary

Graphene oxide nanoribbon (GONR) is a good candidate to be used as electrode materials in electrochemical sensors due to the ease of synthesis, solution processability and versatile properties. GONR is a strip of single-atomic-layer of carbon honeycomb lattice with high length-to-width ratio and straight edges. One of the improved techniques in chemically derived GONR is the longitudinal unzipping of multi-walled carbon nanotubes (MWCNTs) by using oxidizing agents in strong acidic conditions. Owing to the strong oxidative reaction during unzipping process, the resulting GONRs are covered with an attractive surface and edges containing oxygen functional groups. The polar oxygen functional groups of GONR render its strong hydrophilicity that in turn gives a good dispersibility in polar solvents and water. Subsequently, the stable GONR dispersion can be deposited on various substrates to form a thin layer film as electrode materials by drop casting, spraying or spin-coating methods. However, the electrochemical performance on carbon electrode is sensitive to the presence of surface oxide, which either catalyzes the electron transfer or modifies the surface charge.

The first chapter discussed on the effects of MWCNT diameter and sulfuric acid (H_2SO_4) pre-treatment time on the formation graphene oxide nanoribbons (GONRs) produced by an oxidative unzipping process. The aim of this study is to understand the rate of unzipping and degree of oxidation of produced GONR that subsequently affect the electrochemical performance. Scanning electron microscopy (SEM) images reveal that the large MWCNTs (MWCNT_L) produced fully opened and exfoliated nanoribbons at a 3 h

oxidation period; the medium MWCNTs (MWCNT_M) formed a mixture of nanoribbons and nanotubes in the extended acid treatment period; and the small MWCNTs (MWCNT_S) failed to unzip despite a long suspension time in concentrated H_2SO_4. Characterization of the synthesized GONRs reveal that the unzipping rate follows the case of MWCNT_L > MWCNT_M > MWCNT_S at 12 > 6 > 3 h suspension times in H_2SO_4. When being used as electrode materials in electrochemical sensors, GONR demonstrated fast charge-transfer kinetics and superior electro-catalytic activities compared to the MWCNT precursors in detecting hydrogen peroxide (H_2O_2) and β-nicotinamide adenine dinucleotide (NAD).

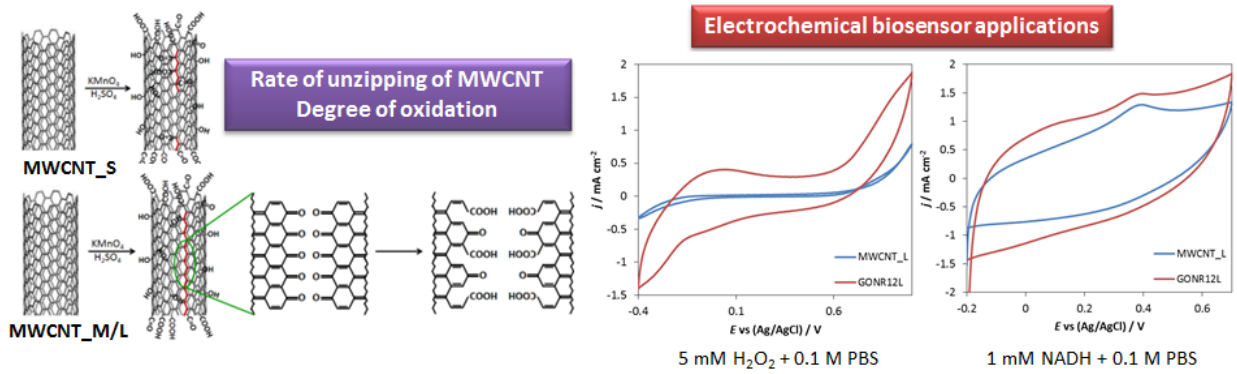

Figure 5.1: Effect of MWCNT diameter and oxidizing time on rate of unzipping and degree of oxidation of produced GONR through longitudinal unzipping method towards electrochemical biosensor applications.

As a step further in GONR-based electrochemical sensor application, GONR was utilized in development of non-enzymatic glucose sensor. This study focuses on enhancing the catalytic activity of gold nanoparticles (AuNPs) by GONRs as a functional supporting matrix for a non-enzymatic glucose sensor operating under neutral condition. The proposed method for electrode fabrication offers the ability to control the GONR and AuNP loading for optimum catalytic performance. In our catalytic system, AuNPs supported by GONRs was profoundly superior to the unsupported conventional bare gold electrode, with a greatly enhanced current density (≈200%). This is attributed not only to the high total surface area of

the AuNPs compared to that of a Au sheet, but also to the three-dimensional specific interaction between the functional groups on the GONRs and the Au active sites with the reactant and the intermediates that promote the reaction kinetics.

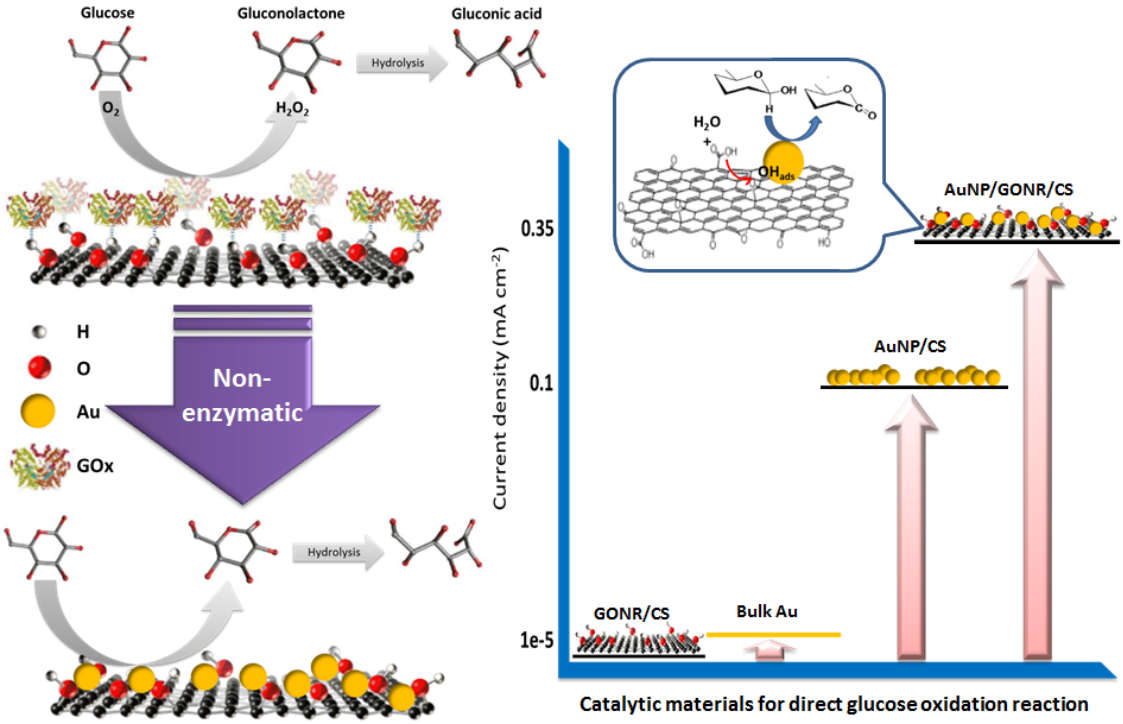

Figure 5.2: Development of non-enzymatic glucose sensor utilizing AuNP on GONR supporting matrix for direct glucose oxidation reaction in neutral conditions.

Many studies have been devoted to understanding the mechanism of luminol ECL in luminol-hydrogen peroxide (H_2O_2) liquid phase system and to improve the ECL emission by integrating with enzyme and noble metal catalysts. However, the study on mechanism of ECL of luminol in solid-liquid interface is still lacking. Thorough studies were done on the ECL performance of *N*-(aminobutyl)-*N*-(ethylisoluminol)-functionalized gold nanoparticle (ABEI-AuNP) hybridized with GONRs on a carbon screen printed electrode (SPE) in alkaline conditions. ABEI-AuNPs supported by GONRs was superior to the unsupported ABEI-AuNP/SPE with a greatly enhanced ECL intensity at negatively shift potential. This

phenomenon is attributed to increment in total surface area of the ABEI-AuNP-GONR/SPE and enhancement of ABEI-AuNP catalytic activity. The boost of catalytic activity of ABEI-AuNP facilitates the oxidative radical generation and faster reaction kinetics on ABEI oxidation process. Further applications of ABEI-AuNP-GONR/SPE in enzymatic biosensor, demonstrates sensitive and selective detection of target analytes at low concentration. In conclusion, GONRs have been identified to act as a backbone to keep ABEI-AuNP from aggregate through non-covalent interactions. Moreover, metal-oxygen bonding between oxygen functional groups on GONR and the ABEI-AuNP active sites enhances the catalytic activity of ABEI-AuNP, which subsequently improved ECL intensity.

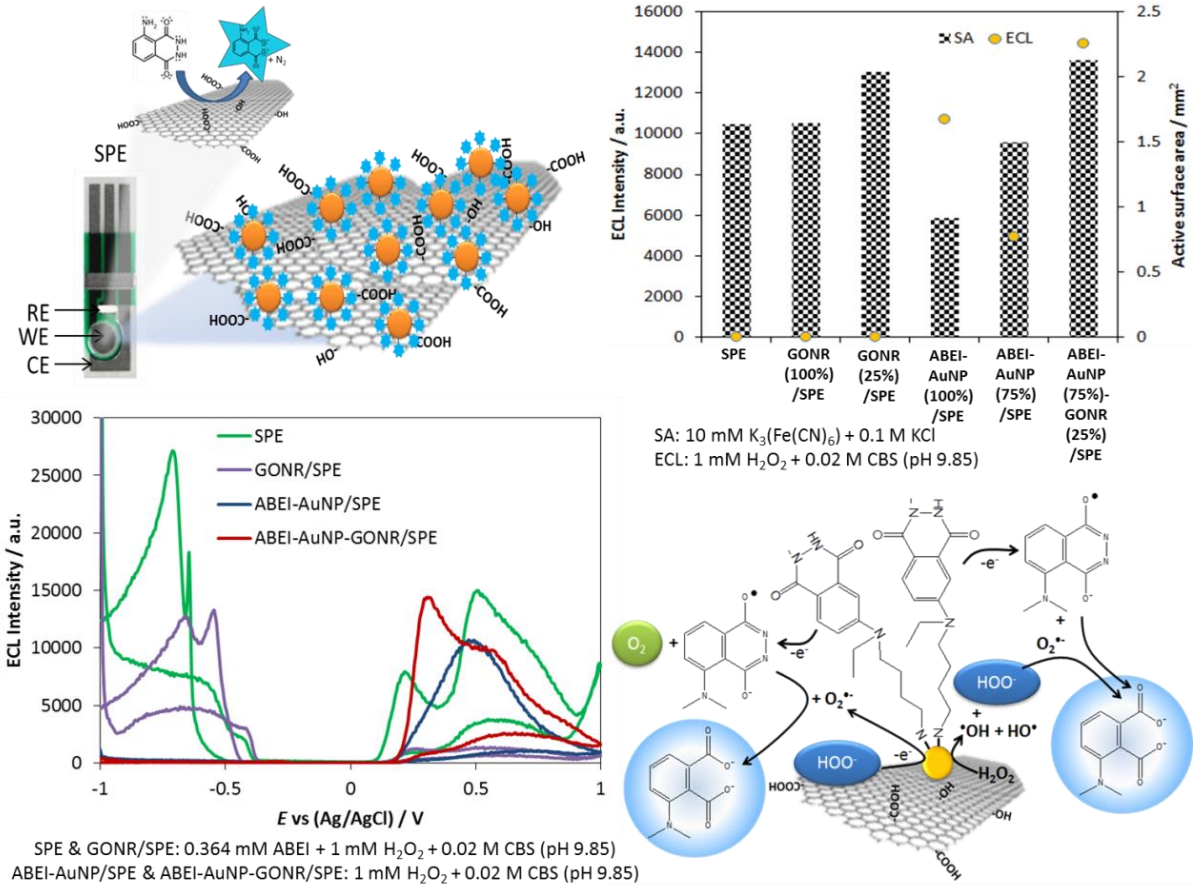

Figure 5.3: Co-assembled of ABEI functionalized AuNP with GONR supporting matrix on modified SPE for enhanced of ECL in solid phase.

In conclusion, we have examined the unzipping rate and the oxidation degree on various diameters of MWCNT in synthesizing GONR through the oxidative longitudinal unzipping. Employing GONR as electrode material in electrochemical sensors demonstrated superior electro-catalytic activity in comparison to their MWCNT precursors owing to the highly active surface areas with oxygenated functional groups that speed up redox reactions. Moreover, GONR has been proven to be a good supporting matrix for noble metal catalysts, especially AuNP, for the catalytic activity enhancement in both electrochemical and electrochemiluminescence systems.

5.2 Future Remarks

GONR has been proven to be a good supporting matrix for noble metal catalysts, especially AuNP, for the catalytic activity enhancement in both electrochemical and electrochemiluminescence (ECL) biosensor. However, in non-enzymatic glucose sensor development, the performance of fabricated electrode AuNP/GONR/CS towards glucose oxidation reaction is severely affected in blood serum due to poison of AuNPs by various interference electroactive species. The utilization of protective membrane PPy-Nafion capable to reduce the interference effect, but resulted in decrease sensitivity of electrode. Therefore, development of more effective protective membrane is required to improve electrode sensitivity and selectivity in real blood sample, which can be applied in *in-vivo* continuous glucose monitoring. Apart from that, we have successfully developed glucose and urea biosensor using ECL method on ABEI-AuNP-GONR/SPE. Our preliminary study on urea sensor show proportional increment in ECL intensity with urea concentrations. Hence, ABEI-AuNP-GONR/SPE should be tested in real urine sample to examine the possible biosensor application. Moreover, numerous optimizations on electrode fabrication are crucial for better reproducibility of ECL results.

LIST OF PUBLICATIONS

1. **Nur Syakimah Ismail**, Le Quynh Hoa, Hiroyuki Yoshikawa, Masato Saito, Eiichi Tamiya. Development of Non-enzymatic Electrochemical Glucose Sensor Based on Graphene Oxide Nanoribbon – Gold Nanoparticle Hybrid. *Electrochimica Acta*, 2014, **146**, 98-105.
2. **Nur Syakimah Ismail**, Le Quynh Hoa, Hiroyuki Yoshikawa, Masato Saito, Eiichi Tamiya. Effect of MWCNT Diameter and Chemical Oxidation Time on Formation and Performance of Graphene Oxide Nanoribbons for Electrochemical Biosensor Applications. (Submitted).
3. **Nur Syakimah Ismail**, Le Quynh Hoa, Hiroyuki Yoshikawa, Eiichi Tamiya. Enhanced Electrochemiluminescence of *N*-(aminobutyl)-*N*-(ethylisoluminol)-Functionalized Gold Nanoparticles by Graphene Oxide Nanoribbons. (In preparation).
4. **Nur Syakimah Ismail**, Le Quynh Hoa, Hiroyuki Yoshikawa, Eiichi Tamiya. Development of Urea Electrochemiluminescence Sensor using *N*-(aminobutyl)-*N*-(ethylisoluminol)-Functionalized Gold Nanoparticles – Graphene Oxide Nanoribbons Hybrid. (In preparation).

PRESENTATIONS AT SCIENTIFIC MEETING

1. **Nur Syakimah Ismail**, Le Quynh Hoa, Hiroyuki Yoshikawa, Masato Saito, Eiichi Tamiya. Non-Enzymatic Electrochemical Glucose Sensor Based On Graphene-Oxide Nanoribbons. The 80th Spring Meeting of the Electrochemical Society of Japan. Kawauchi Campus, Tohoku University, Sendai, Japan. 29-31 March 2013. (Oral presentation).
2. **Nur Syakimah Ismail**, Le Quynh Hoa, Hiroyuki Yoshikawa, Masato Saito, Eiichi Tamiya. Optimization of Graphene Oxide Nanoribbons Preparation Process for Biosensor Application. 2013 JSP – MRS Joint Symposia. Doshisha University, Kyoto, Japan. 16-20 September 2013. (Poster presentation).
3. **Nur Syakimah Ismail**, Le Quynh Hoa, Tomohiko Ikeuchi, Eiichi Tamiya. Gold Nanoparticle-Linked Electrochemical Immuno-Assay for Pork Protein Detection. 2nd International Symposium Halal Science and Innovative Product Development. Rizqun International Hotel, Brunei Darussalam. 11-13 February 2014. (Poster presentation).
4. **Nur Syakimah Ismail**, Le Quynh Hoa, Hiroyuki Yoshikawa, Masato Saito, Eiichi Tamiya. Effects of Oxidizing Time and Unzipping MWCNT Size on The Performance of Graphene Oxide Nanoribbons based Biosensor. The 81st Spring Meeting of the Electrochemical Society of Japan. Kansai University, Osaka, Japan. 29-31 March 2014. (Oral presentation).
5. **Nur Syakimah Ismail**, Le Quynh Hoa, Eiichi Tamiya. Electrochemiluminescence of Luminol on Gold Nanoparticles – Graphene Oxide Nanoribbons Hybrid. The 65th Annual Meeting of the International Society of Electrochemistry. The Swiss Tech Convention Center, EPFL, Laussane, Switzerland. 31 August – 5 September 2014. (Poster presentation).

6. **Nur Syakimah Ismail**, Le Quynh Hoa, Hiroyuki Yoshikawa, Masato Saito, Eiichi Tamiya. Electrochemiluminescence of Isoluminol-Gold Nanoparticle-Graphene Oxide Nanoribbon Hybrid. 2014 Fall Meeting of The Electrochemical Society of Japan. Hokkaido University, Hokkaido, Japan. 27-28 September 2014. (Oral presentation).
7. **Nur Syakimah Ismail**, Akiko Araki, Hiroyuki Yoshikawa, Masato Saito, Eiichi Tamiya. Development of Urea Electrochemiluminescence Biosensor Using Isoluminol-Functionalized Gold Nanoparticles-Graphene Oxide Nanoribbons Hybrid. The 82nd Spring Meeting of the Electrochemical Society of Japan. Yokohama National University, Yokohama, Japan. 15 - 17 March 2015. (Oral presentation).

ACKNOWLEDGEMENTS

I wish to express my gratitude to all the people whose support made completion of my doctoral degree possible. First and foremost, I would like to convey my deepest appreciation to my supervisor Prof. Eiichi Tamiya for giving me the opportunity to join Nano-Bioengineering laboratory. His guidance, continuous support and constructive criticism are key motivations in completing my study. I also gratefully acknowledge Prof. Yoshihiro Kobayashi, Prof. Yasushi Inouye and Prof. Toshifumi Takeuchi (Kobe University) for insightful comments and suggestions that help me to improve the quality of this thesis.

My sincere thanks to Dr. Hiroyuki Yoshikawa and Dr. Masato Saito for their continuous help in my study. I would like to convey my appreciation to all staffs and members of Tamiya Lab for supporting me in so many ways and exposing Japanese culture through many extracurricular activities. I am blessed with a wonderful mentor and good friend, Dr Le Quynh Hoa who assist me throughout my research and daily life in Japan. I have met many amazing friends during my study in Osaka University who inspire and encourage me to strive for greatness.

I have received much help from Malaysian community in Osaka University especially and in Osaka generally. I truly appreciate their kind help and warm hospitality that make my stay in Japan bearable. I am very thankful to all my best friends for always be a good listener, a helping hand and an angel.

Special thanks to my parent and family for their understanding, generous encouragement and endless support throughout my study. Without their love and prayers, I might not come this far.

Financial support from Ministry of Higher Education Malaysia and Universiti Malaysia Perlis are greatly acknowledged.